THERMAL DISPERSION AND CONVECTIVE HEAT TRANSFER DURING LAMINAR PULSATING FLOW IN POROUS MEDIA

A Thesis
Presented to
The Academic Faculty

by

Mihir Gaurang Pathak

In Partial Fulfillment
of the Requirements for the Degree
Master of Science in the
School of Mechanical Engineering

Georgia Institute of Technology
August 2010

THERMAL DISPERSION AND CONVECTIVE HEAT TRANSFER DURING LAMINAR PULSATING FLOW IN POROUS MEDIA

Approved by:

Dr. S. Mostafa Ghiaasiaan, Advisor
School of Mechanical Engineering
Georgia Institute of Technology

Dr. Prateen Desai
School of Mechanical Engineering
Georgia Institute of Technology

Dr. Sheldon Jeter
School of Mechanical Engineering
Georgia Institute of Technology

Date Approved: 6/24/2010

To my parents Gaurang and Sandhya Pathak

ACKNOWLEDGEMENTS

First, I would like to extend my greatest gratitude to Professor Ghiaasiaan. He has not only been my advisor, but also my mentor and guru. Without his sound advice, consistent motivation, and endless support, I would not be where I am today. I truly appreciate all that he has done for me. I would also like to thank Professor Desai and Professor Jeter for serving on my committee and for their insightful suggestions.

I must give praise to the George W. Woodruff School of Mechanical Engineering for the unparalleled opportunities I have been provided with. I must thank the staff and support center and extend a personal thank you to Dr. Whiteman, whose help and advice through my time at Georgia Tech is greatly appreciated. I must also thank the Institute as a whole for the love it has shown me through my time at Tech and for the GT Presidential Fellowship.

Unequivocal advice has come from Mr. Ted Conrad, my friend and lab partner, whose aid and patience have helped me out tremendously. Many other graduate students have helped me during my Master's tenure. The support and time spent together through coursework and research have resulted in deep and unbreakable bonds that will stay with me forever.

My brother, Munir Pathak and my dear friend, Praachi Jani, have given me their shoulders to lean on during my time in graduate school. Without them, the stress of

graduate life would have been very difficult to deal with. My sincere appreciation goes to Munir and Praachi for their encouragement and making sure that I get out of the lab once in a while.

Finally, I would like to thank my parents, Gaurang and Sandhya Pathak. Their endless support, motivational words, and love have gotten me through the tough times at Georgia Tech. Words cannot express the gratitude that I feel. They have always believed in me and pushed me to pursue my dreams.

TABLE OF CONTENTS

	Page
ACKNOWLEDGEMENTS	iv
LIST OF TABLES	viii
LIST OF FIGURES	ix
LIST OF SYMBOLS AND ABBREVIATIONS	xiv
SUMMARY	xvii
CHAPTER	
1 Introduction	1
1.1 Background	2
1.1.1 History of Cryogenic Refrigerators	2
1.1.2 Pulse Tube Refrigerators	3
1.1.3 Applications of Pulse Tube Cryocoolers	6
1.2 Purpose	7
2 Literature Survey	10
2.1 Porous Media Flow Physics	10
2.2 Numerical Modeling	12
2.3 Regenerator and Cryocooler Applications	16
2.4 Closing Remarks	19
3 Simulated System	20
3.1 Computational Model	20
3.2 Grid Convergence and Meshing Scheme	24
4 Theory	25
4.1 Flow Regime	25

4.2 Volume-Average Governing Equations 26
4.3 Calculated Parameters 31
4.4 Inlet, Initial, and Boundary Conditions 33
5 Results and Discussion 36
5.1 General Remarks 36
5.1.1 Convergence 38
5.1.2 Parametric Tests 39
5.2 Convection Heat Transfer 43
5.2.1 Solid-Fluid Heat Transfer Coefficients 44
5.2.2 Nusselt Numbers 47
5.2.3 Nusselt Number Correlation 52
5.3 Thermal Energy Dispersion 53
5.3.1 Thermal Dispersion 53
5.3.2 Non-Dimensional Thermal Dispersion 55
5.3.3 Thermal Dispersion Correlation 59
5.4 Effective Thermal Conductivity 61
6 Conclusion and Recommendations 65
6.1 Concluding Remarks 65
6.2 Recommendations for Future Work 66
APPENDIX A: FLUENT USER DEFINED FUNCTION 68
APPENDIX B: NUSSLET NUMBER PLOTS 69
APPENDIX C: DIMENSIONLESS THERMAL DISPERSION PLOTS 85
REFERENCES 101

LIST OF TABLES

	Page
Table 4.1: Fluid Properties	35
Table 5.1: Varied Parameters	40
Table 5.2: Calculated Variables	43

LIST OF FIGURES

Page

Figure 1.1: Pulse Tube Cryocooler [1]. 1

Figure 1.2: Cryocooler Types [1]. 3

Figure 1.3: The Basic Pulse Tube Cryocooler [5]. 4

Figure 1.4: Orifice Pulse Tube Cryocooler [6]. 5

Figure 1.5: Inertance Tube Pulse Tube Cryocooler [6]. 5

Figure 1.6: Wire Mesh 200x Magnification [7]. 8

Figure 1.7: Perforated Disk 200x Magnification [7]. 8

Figure 2.1: Generic Porous Media. 13

Figure 2.2: Nusselt Number as a Function of Porous Layer Thickness. 14

Figure 2.3: Porous Structure with Coordinate System. 15

Figure 2.4: Friction Factor Study. 18

Figure 3.1: The Simulated System [36]. 20

Figure 3.2: Computational Domain with Buffer Zones [36]. 22

Figure 3.3: 64% Porosity [12]. 23

Figure 3.4: 75% Porosity [12]. 23

Figure 3.5: 84% Porosity [12]. 24

Figure 5.1: Velocity Profile. 37

Figure 5.2: Temperature Profile. 37

Figure 5.3: Average Temperature Comparison Plot. 39

Figure 5.4: 64% Porosity – Heat Transfer Coefficient vs. Frequency. 44

Figure 5.5: 75% Porosity – Heat Transfer Coefficient vs. Frequency. 45

Figure 5.6: 84% Porosity – Heat Transfer Coefficient vs. Frequency. 45

Figure 5.7: Unit Cell Heat Transfer Coefficients. 46

Figure 5.8: Instantaneous, Unit Cell-Average Heat Transfer Coefficient. 47

Figure 5.9: 64% Porosity – Nusselt Number vs. Frequency. 48

Figure 5.10: 75% Porosity – Nusselt Number vs. Frequency. 48

Figure 5.11: 84% Porosity – Nusselt Number vs. Frequency. 49

Figure 5.12: 64% Porosity – Nusselt Number vs. Valensi Number. 50

Figure 5.13: 75% Porosity – Nusselt Number vs. Valensi Number. 50

Figure 5.14: 84% Porosity – Nusselt Number vs. Valensi Number. 51

Figure 5.15: Comparison of Nusselt Number Correlation vs. Numerical Predictions. 53

Figure 5.16: 64% Porosity – Thermal Dispersion vs. Frequency. 54

Figure 5.17: 75% Porosity – Thermal Dispersion vs. Frequency. 54

Figure 5.18: 84% Porosity – Thermal Dispersion vs. Frequency. 55

Figure 5.19: 64% Porosity – Non-Dimensional Dispersion vs. Frequency. 56

Figure 5.20: 75% Porosity – Non-Dimensional Dispersion vs. Frequency. 56

Figure 5.21: 84% Porosity – Non-Dimensional Dispersion vs. Frequency. 57

Figure 5.22: 64% Porosity – Non-Dimensional Dispersion vs. Valensi Number. 57

Figure 5.23: 75% Porosity – Non-Dimensional Dispersion vs. Valensi Number. 58

Figure 5.24: 84% Porosity – Non-Dimensional Dispersion vs. Valensi Number. 58

Figure 5.25: Comparison of D_T^* Correlation vs. Numerical Predictions. 60

Figure 5.26: Instantaneous Dispersion Conductivity at 75% Porosity and $Re_L = 420$. 61

Figure 5.27: Instantaneous Dispersion Conductivity at 64% Porosity and $Re_L = 560$. 62

Figure 5.28: Instantaneous Dispersion Conductivity at 84% Porosity and $Re_L = 280$. 62

Figure 5.29: Instantaneous Dispersion Conductivity at 84% Porosity and $Re_L = 840$. 63

Figure 5.30: Stead Flow Dimensionless Dispersion Thermal Conductivity 64

Figure A.1: Inlet Velocity Condition. 68

Figure B.1: 64% Porosity – Nusselt Number vs. Reynolds Number. 69

Figure B.2: 75% Porosity – Nusselt Number vs. Reynolds Number. 70

Figure B.3: 84% Porosity – Nusselt Number vs. Reynolds Number. 70

Figure B.4: Reynolds Number = 70 – Nusselt Number vs. Frequncey. 71

Figure B.5: Reynolds Number = 140 – Nusselt Number vs. Frequency. 71

Figure B.6: Reynolds Number = 280 – Nusselt Number vs. Frequency. 72

Figure B.7: Reynolds Number = 420 – Nusselt Number vs. Frequency. 72

Figure B.8: Reynolds Number = 560 – Nusselt Number vs. Frequency. 73

Figure B.9: Reynolds Number = 700 – Nusselt Number vs. Frequency. 73

Figure B.10: Reynolds Number = 840 – Nusselt Number vs. Frequency. 74

Figure B.11: Reynolds Number = 980 – Nusselt Number vs. Frequency. 74

Figure B.12: Reynolds Number = 70 – Nusselt Number vs. Unit Cell Porosity. 75

Figure B.13: Reynolds Number = 140 – Nusselt Number vs. Unit Cell Porosity. 75

Figure B.14: Reynolds Number = 280 – Nusselt Number vs. Unit Cell Porosity. 76

Figure B.15: Reynolds Number = 420 – Nusselt Number vs. Unit Cell Porosity. 76

Figure B.16: Reynolds Number = 560 – Nusselt Number vs. Unit Cell Porosity. 77

Figure B.17: Reynolds Number = 700 – Nusselt Number vs. Unit Cell Porosity. 77

Figure B.18: Reynolds Number = 840 – Nusselt Number vs. Unit Cell Porosity. 78

Figure B.19: Reynolds Number = 980 – Nusselt Number vs. Unit Cell Porosity. 78

Figure B.20: Frequency = 0 Hz – Nusselt Number vs. Unit Cell Porosity. 79

Figure B.21: Frequency = 20 Hz – Nusselt Number vs. Unit Cell Porosity. 79

Figure B.22: Frequency = 40 Hz – Nusselt Number vs. Unit Cell Porosity. 80

Figure B.23: Frequency = 64 Hz – Nusselt Number vs. Unit Cell Porosity. 80

Figure B 24: Frequency = 80 Hz – Nusselt Number vs. Unit Cell Porosity. 81

Figure B.25: Frequency = 100 Hz – Nusselt Number vs. Unit Cell Porosity. 81

Figure B.26: Frequency = 0 Hz – Nusselt Number vs. Reynolds Number. 82

Figure B.27: Frequency = 20 Hz – Nusselt Number vs. Reynolds Number. 82

Figure B.28: Frequency = 40 Hz – Nusselt Number vs. Reynolds Number. 83

Figure B.29: Frequency = 64 Hz – Nusselt Number vs. Reynolds Number. 83

Figure B.30: Frequency = 80 Hz – Nusselt Number vs. Reynolds Number. 84

Figure B.31: Frequency =100 Hz – Nusselt Number vs. Reynolds Number. 84

Figure C.1: 64% Porosity – Non-Dimensional Dispersion vs. Reynolds Number. 85

Figure C.2: 75% Porosity – Non-Dimensional Dispersion vs. Reynolds Number. 86

Figure C.3: 84% Porosity – Non-Dimensional Dispersion vs. Reynolds Number. 86

Figure C.4: Reynolds Number = 70 – Non-Dimensional Dispersion vs. Frequncey. 87

Figure C.5: Reynolds Number = 140 – Non-Dimensional Dispersion vs. Frequency. 87

Figure C.6: Reynolds Number = 280 – Non-Dimensional Dispersion vs. Frequency. 88

Figure C.7: Reynolds Number = 420 – Non-Dimensional Dispersion vs. Frequency. 88

Figure C.8: Reynolds Number = 560 – Non-Dimensional Dispersion vs. Frequency. 89

Figure C.9: Reynolds Number = 700 – Non-Dimensional Dispersion vs. Frequency. 89

Figure C.10: Reynolds Number = 840 – Non-Dimensional Dispersion vs. Frequency. 90

Figure C.11: Reynolds Number = 980 – Non-Dimensional Dispersion vs. Frequency. 90

Figure C.12: Reynolds Number = 70 – Non-Dimensional Dispersion vs. Porosity. 91

Figure C.13: Reynolds Number = 140 – Non-Dimensional Dispersion vs. Porosity. 91

Figure C.14: Reynolds Number = 280 – Non-Dimensional Dispersion vs. Porosity. 92

Figure C.15: Reynolds Number = 420 – Non-Dimensional Dispersion vs. Porosity. 92

Figure C.16: Reynolds Number = 560 – Non-Dimensional Dispersion vs. Porosity. 93

Figure C.17: Reynolds Number = 700 – Non-Dimensional Dispersion vs. Porosity. 93

Figure C.18: Reynolds Number = 840 – Non-Dimensional Dispersion vs. Porosity. 94

Figure C.19: Reynolds Number = 980 – Non-Dimensional Dispersion vs. Porosity. 94

Figure C.20: Frequency = 0 Hz – Non-Dimensional
Dispersion vs. Unit Cell Porosity. 95
Figure C.21: Frequency = 20 Hz – Non-Dimensional
Dispersion vs. Unit Cell Porosity. 95
Figure C.22: Frequency = 40 Hz – Non-Dimensional
Dispersion vs. Unit Cell Porosity. 96
Figure C.23: Frequency = 64 Hz – Non-Dimensional
Dispersion vs. Unit Cell Porosity. 96
Figure C.24: Frequency = 80 Hz – Non-Dimensional
Dispersion vs. Unit Cell Porosity. 97
Figure C.25: Frequency = 100 Hz – Non-Dim. Dispersion vs. Unit Cell Porosity. 97
Figure C.26: Frequency = 0 Hz – Non-Dimensional
Dispersion vs. Reynolds Number. 98
Figure C.27: Frequency = 20 Hz – Non-Dimensional
Dispersion vs. Reynolds Number. 98
Figure C.28: Frequency = 40 Hz – Non-Dimensional
Dispersion vs. Reynolds Number. 99
Figure C.29: Frequency = 64 Hz – Non-Dimensional
Dispersion vs. Reynolds Number. 99
Figure C.30: Frequency = 80 Hz – Non-Dimensional
Dispersion vs. Reynolds Number. 100
Figure C.31: Frequency =100 Hz – Non-Dim. Dispersion vs. Reynolds Number. 100

LIST OF SYMBOLS AND ABBREVIATIONS

H/L	Aspect Ratio [-]
D	Cylinder Diameter [m]
L	Unit Cell Length [m]
ε	Structure Porosity [-]
Re_K	Pore-Base Reynolds Number [-]
K	Permeability Coefficient [m^2]
ρ_f	Fluid Density [kg/m^3]
$\left\|\left\langle \vec{u} \right\rangle\right\|$	Volume-Average Fluid Velocity [m/s]
μ_f	Fluid dynamic Viscosity [kg/m-s]
Re_L	Unit Cell Length-Based Reynolds Number [-]
$\left\langle \phi \right\rangle^f$	Volume-Average Fluid Property
ϕ	Fluid Property
V_f	Fluid Volume [m^3]
V	Total Volume [m^3]
$\tilde{\phi}$	Spatial Deviation of Fluid Property
u_j	Velocity Vector [m/s]
b	Forchheimer Constant [m^2]
ν_f	Fluid Kinematic Viscosity [m^2/s]
t	Time [s]
c_{pf}	Fluid Specific Heat [J/kg-K]

T	Temperature [K]
$\langle T \rangle^f$	Volume-Average Fluid Temperature [K]
k_f	Fluid Thermal Conductivity [W/m-K]
n_j	Unit Vector [-]
A_{int}	Solid-Fluid Interface Area [m^2]
D_T	Volume-Average Thermal Dispersion [W/m^2]
a_f	Specific Area [$1/m^2$]
h_f	Heat Transfer Coefficient [W/m^2-k]
$\langle T \rangle^s$	Volume-Average Solid Temperature [K]
Nu_L	Volume-Average Nusselt Number [-]
$\left\langle \frac{dT}{dx} \right\rangle$	Volume-Average Unit Cell Temperature Gradient [W/m]
$u_{\max}$	Unit Cell Average Maximum Velocity [m/s]
D_T^*	Dimensionless Average Thermal Dispersion [-]
k_{disp}	Thermal Dispersion Thermal Conductivity [W/m-K]
U_{in}	Inlet Velocity [m/s]
U_m	Mean Fluid Velocity [m/s]
a	Flow Pulsation Amplitude [-]
f	Pulsation Frequency [Hz]
Va_L	Unit Cell Length-Based Valensi Number [-]
ω	Angular Frequency [rad/s]
$\%Error$	Percentage Error [%]

$Nu_{L,computational}$	Simulation-Based Cycle-Average Nusselt Number [-]
$Nu_{L,correlation}$	Correlation-Based Cycle-Average Nusselt Number [-]
$D^*_{T,computational}$	Simulation-Based Cycle-Average Dimensionless Thermal Dispersion [-]
$D^*_{T,correlation}$	Correlation-Based Cycle-Average Dimensionless Thermal Dispersion [-]
k_{disp}/k_f	Dimensionless Thermal Conductivity [-]
f	Fluid
s	Solid
CFD	Computational Fluid Dynamics
UDF	User Defined Functions

SUMMARY

The most important component of pulse tube and Stirling cryocoolers is the regenerator. The solid-fluid interactions within the filling structure inside the regenerator greatly affect and determine the overall performance of the cryogenic system. Therefore, it is necessary to understand the fluid and energy transport phenomena occurring within the regenerator. This investigation studies the thermal dispersion and heat transfer effects that occur during incompressible laminar pulsating flow within a porous medium via a computation model. Pulsating flow is investigated as the precursor for the more complicated periodic flow, which will be addressed in the future. The pore scale heat transfer coefficient and thermal dispersion interactions are examined. Arrays of square cylinders were used to make up the simulated porous geometry, where the porosity is varied by scaling the cylinder diameters. Specialized user defined functions were created to impose a pulsating flow condition and flow simulations were conducted with Fluent CFD code. The volume-average mass, momentum, and energy conservation equations were solved, and the average Nusselt number and average dimensionless thermal dispersion were determined. The computational investigation revealed that the average Nusselt number and the magnitude of the dimensionless thermal dispersion decreased with increasing oscillation frequency for a given unit cell length-based Reynolds number and structure porosity. The instantaneous thermal dispersion conductivity was found to vary periodically during each cycle and was found to be orders of magnitude larger than the molecular thermal conductivity of the fluid. Finally, correlations for the cycle-average

volume-average Nusselt number and non-dimensional thermal dispersion were derived and compared well with the generated numerical data.

CHAPTER 1

INTRODUCTION

Cryogenics is a branch of physics and engineering that involves low temperature studies in the range of absolute zero to 120 Kelvin. The goal of cryogenic scientists and engineers is to study the physical phenomena occurring at these very low temperatures and investigate applications that can be developed or improved upon. One particular cryogenic system, the Pulse Tube Cryocooler, shown in Figure 1.1, is a rugged and reliable cooling system that is widely used in space and airborne applications.

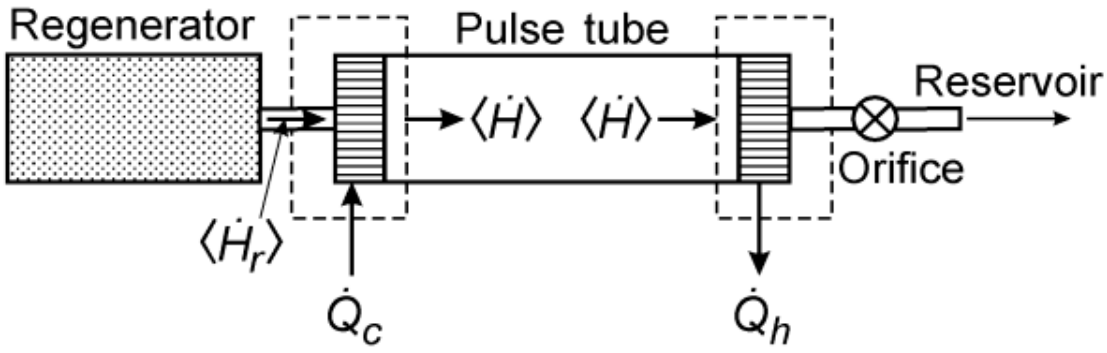

Figure 1.1. Pulse Tube Cryocooler [1].

The regeneration component within the cryogenic system is arguably the most critical part of the entire cooler. Since regenerators are commonly used in such important applications, careful studies and fundamental characterization of the underlying physical processes within these components are needed. The aim of this study is to investigate the thermal dispersion and convective heat transfer occurring during laminar pulsating flow

through generic porous media. Pulsating flow is investigated as a precursor for the more relevant, and more complicated periodic flow, which will be addressed in the future.

1.1 Background

1.1.1 History of Cryogenic Refrigerators

Robert Stirling first introduced the regenerative heat exchanger in his hot air engine in 1816. Later in 1834, John Herschel suggested that Stirling's engine could be used as a refrigerator. Gifford and McMahon in 1960, along with researchers at Philips Corporation developed small regenerative cryogenic refrigerators and established a cryogenic refrigeration industry [2]. In 1963, Gifford and Longworth introduced the first pulse tube cryocooler [3]. Since these historic findings, many different types of cryocoolers have been developed and examples of these can be seen in Figure 1.2.

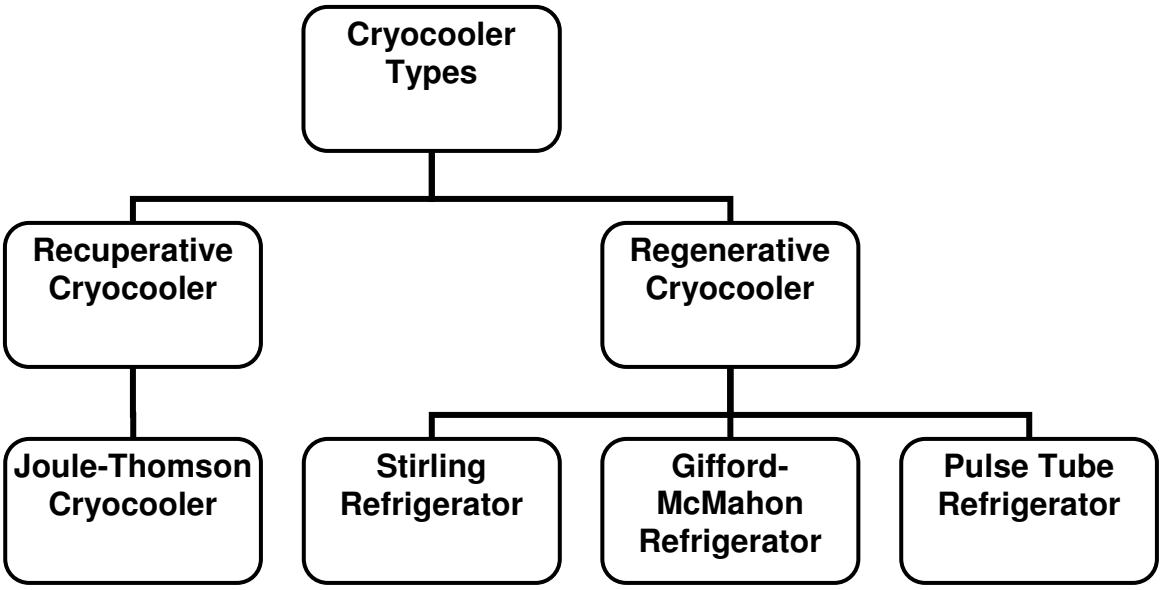

Figure 1.2. Cryocooler Types [1].

1.1.2 Pulse Tube Refrigerators

The basic pulse tube cryocooler can be seen in Figure 1.3. An inflow of helium gas is induced by a moving piston, within a compressor. Helium is primarily used as the working fluid in pulse tube refrigerators due to its ability to stay in the gaseous phase at very low temperatures. Also, helium has a high volumetric heat capacity and high thermal conductivity [4].

From the compressor, the gas flows through the transfer line and enters a warm heat exchanger, where heat is rejected from the fluid to the heat exchanger walls. From the warm heat exchanger, the helium gas transfers through the regenerator where heat is transferred from the fluid to the conductive regenerator material. The gas then goes

through the cold heat exchanger, where heat is received by the fluid, and enters the pulse tube section. After the pulse tube, the gas flows through another warm heat exchanger, where again heat is rejected. From this point the gas oscillates back to the start of the process, completing a full cycle. When the gas flows back through the regenerator, the fluid is cold and heat transfers from the regenerator material to the fluid, serving as preheating before the gas enters the aftercooler.

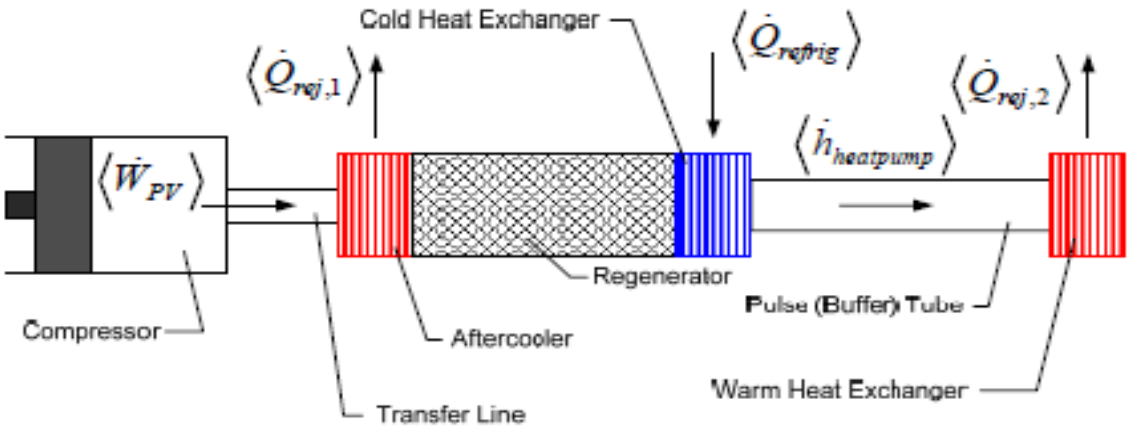

Figure 1.3. The Basic Pulse Tube Cryocooler [5].

Other types of pulse tube cryocoolers include the orifice pulse tube cryocooler and the inertance tube pulse tube cryocooler, shown in Figures 1.4 and 1.5, respectively.

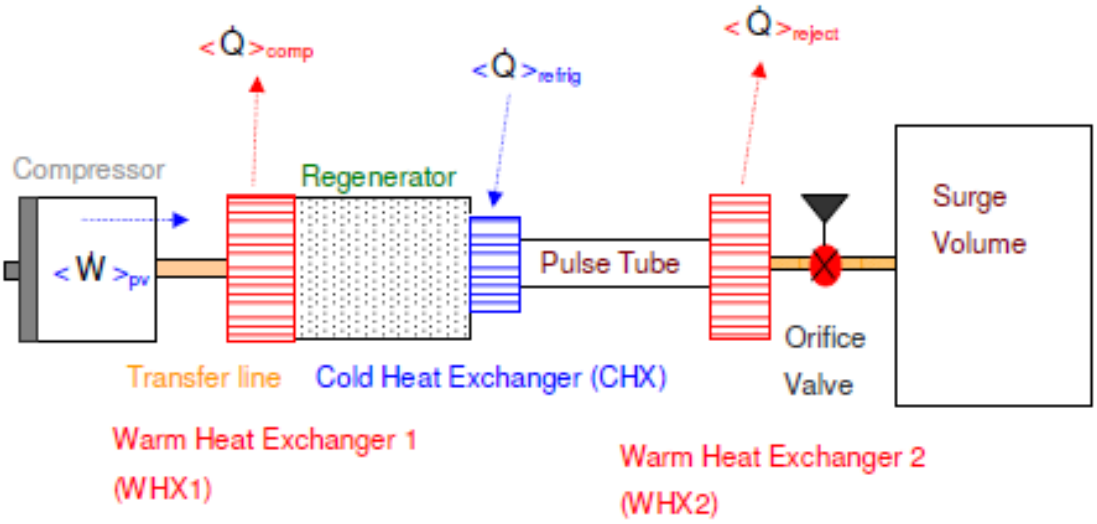

Figure 1.4. Orifice Pulse Tube Cryocooler [6].

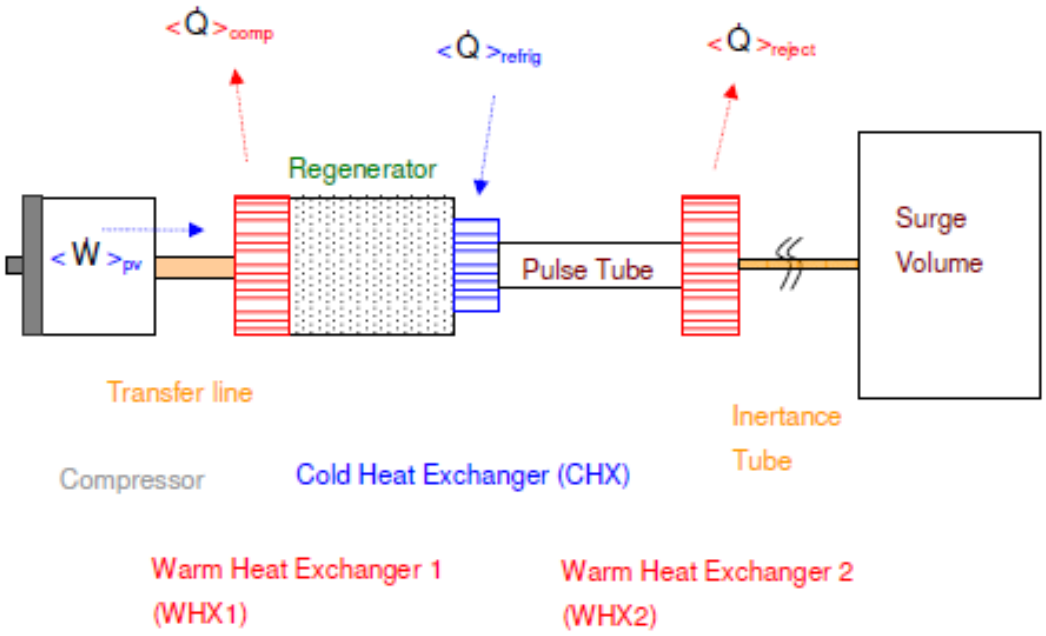

Figure 1.5. Inertance Tube Pulse Tube Cryocooler [6].

The orifice pulse tube cryocooler adds a surge volume and an orifice valve to the basic pulse tube cryocooler in order to improve its performance. The role of the orifice is to help improve a phase difference between the pressure and mass flow waves, which is required for the operation of pulse tube refrigerators. The inertance tube pulse tube cryocooler replaces the orifice valve from the orifice pulse tube cryocooler with an inertance tube. The advantage of the inertance tube pulse tube cryocooler is the fact that this system's only moving component is the piston within the compressor. Due to not having any system level moving parts, this particular cryocooler is the most reliable and long lasting, making it ideal for space based applications.

1.1.3 Applications of Pulse Tube Cryocoolers

The most widely encountered applications for pulse tube cryocoolers are for refrigeration purposes with small heat loads, where high reliability is needed. However, these cryocoolers do have the ability to cool larger heat loads at very low temperatures. Other current applications that use pulse tube cryocoolers include: magnetic resonance imaging, infrared focal plane arrays and detectors, gas liquefaction, mine sweeping magnets, space instruments, and weapon systems [7]. Many other applications could also benefit from pulse tube cryocooling technology.

1.2 Purpose

As can be seen from previous sections, the quality of the regenerator can directly impact the overall system performance of the pulse tube cryocooler. Therefore it is important that the regenerator performance is characterized. Typically, on a system level model, the entire regenerator is modeled as a porous cylinder, however component level models are important to investigate if true regenerator study is to be conducted.

Typically, in pulse tube cryocoolers, the regenerators are filled with stacks of mesh screens which could be wire, sintered, metal foams, or some other type of fine porous structure. Some of the structures examined at the Georgia Tech Cryogenics and Cryocooler Laboratory are shown in Figures 1.6 and 1.7. Each structure can consist of various geometries and various designs. The helium gas that flows through the regenerator travels through these screens losing or gaining heat depending on the direction of the flow field. Although the main purpose of the regenerator is to transfer heat, fundamental solid-fluid interactions on the pore-level, within a single mesh screen, are quite poorly understood, especially for transient and periodic flow.

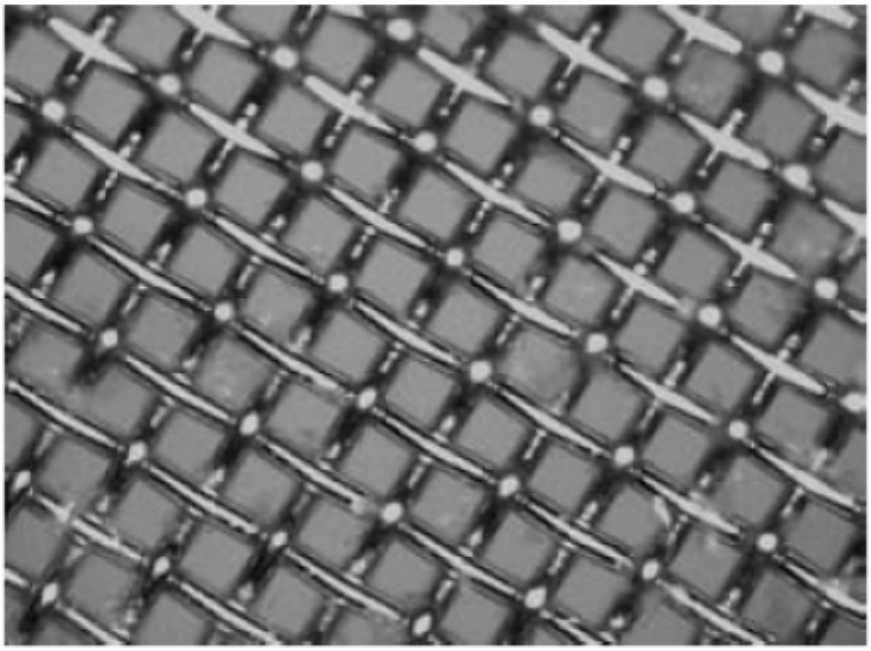

Figure 1.6. Wire Mesh 200x Magnification [7].

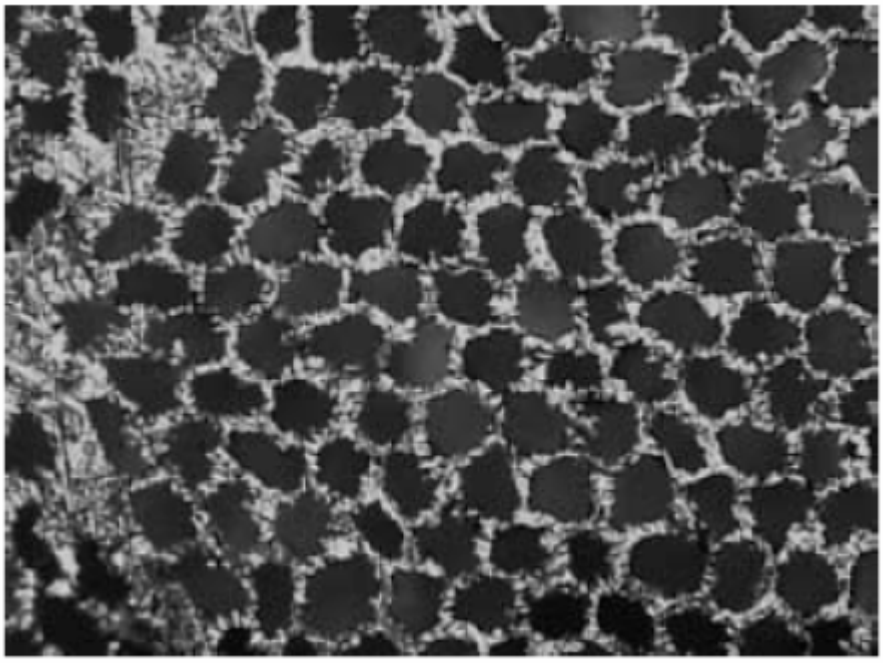

Figure 1.7. Perforated Disk 200x Magnification [7].

The purpose of this study is to investigate the solid-fluid interactions that occur within generic porous media in transient flow at the pore-level. The associated induced flow is laminar pulsating flow, and the porous media are two-dimensional square cylinders. This investigation is thus the first step towards the pore-level numerical investigation for more realistic pore geometries in periodic flow. The convective heat transfer and thermal dispersion are determined and analyzed through direct numerical solutions of the momentum and thermal energy equations.

CHAPTER 2

LITERATURE SURVEY

2.1 Porous Media Flow Physics

Flow in porous media is ubiquitous in nature and industry. The flow of water, oil, and gas in soil is the most familiar application. The literature dealing with flow in porous media is vast. A good review and summary can be found by Kaviany [8]. Flow in porous media is, in general, complicated due to the fact that porous structures often have irregular, non-uniform and often complex geometric configurations. Nevertheless, semi-empirical methods have been developed over decades for modeling the flow and transport phenomena in porous media, based on volume-averaging.

Some aspects of flow in porous media are still poorly understood, however, and the aforementioned volume-averaging-based method cannot be directly applied to all porous media flow problems. An area where the need for further investigations is obvious is unsteady flow, in particular periodic and pulsating flow.

In the following paragraphs, some recent studies relevant to pulsating and periodic flow will be briefly reviewed.

Transition from laminar to turbulent flow regimes is an important issue. Pedras and de Lemos, Liu et al, and Dybbs and Edwards [9], developed a pore Reynolds number, which is suitable for porous media studies. Their pore-level Reynolds number is defined as,

$$\mathrm{Re}_K = \frac{|\vec{u}|\sqrt{K}}{\nu} \tag{2.1}$$

Based on steady-flow experimental data, they found that the transition pore Reynolds number is 350. In steady flow, any Reynolds number at or below 300 can thus be considered laminar [9].

The Forchheimer-extended Darcy equation for incompressible flow through a homogenous and isotropic porous medium has been extensively used in experimental and numerical studies for convection heat transfer in fully developed saturated porous media. Vafai and Tien employed the Forchheimer-extended Darcy equation for incompressible steady flow in a homogenous porous medium [10],

$$-\nabla \langle p \rangle^f = \left(\frac{\mu_f}{K} + \rho_f b \left| \langle \vec{u} \rangle \right| \right) \langle \vec{u} \rangle \tag{2.2}$$

The above equation is a volume-average phenomenological equation. The volume-averaging technique can be further utilized to the mass, momentum, and thermal energy conservation equations for flow through porous media. This has been extensively practiced by Vafai and Tien [10], Nakayama et al [11], Kaiany [8], along with many others.

Kim and Ghiaasiaan [12] used the volume-averaging technique to numerically study laminar pulsating flow through porous media. They investigated two-dimensional flows in systems that consisted of a number of unit cells of generic porous structures, representing periodic arrays of square cylinders, by using a computational fluid dynamics tool. The model had sinusoidal variations in flow with time as the boundary condition and numerical data for a range of porosities with flow pulsation frequencies of 20-64 Hz

were collected. From their analysis, the cycle-average permeability and Forchheimer coefficients to be used in the standard unsteady volume-average momentum conservation equation for flow in porous media were derived. However, a solution to the volume-average thermal energy conservation equation remains to be solved.

2.2 Numerical Modeling

Since there is much complexity and inaccuracy, due to apparatus and flow control, in experimental studies when dealing with flow physics, direct numerical simulation models that resolve the pore-level geometric details and solve the conservation equations without any arbitrary or simplifying assumptions have become popular as substitutes or complements to experiments. The numerical investigations have made pore-level information easier. Many researchers have used numerical models to collect data and derive solutions to flow and energy equations in porous media with simple and generic pore structures.

Nakayama et al. [13] developed a two-energy equation model for analyzing conduction and convection within porous media, where the system is in local thermal non-equilibrium. The exact solutions were obtained for two cases: the one-dimensional steady conduction in a porous slab with internal heat generations in the solid; and thermally developing unidirectional flow through a semi-infinite medium. Figure 2.1 shows their generic porous media.

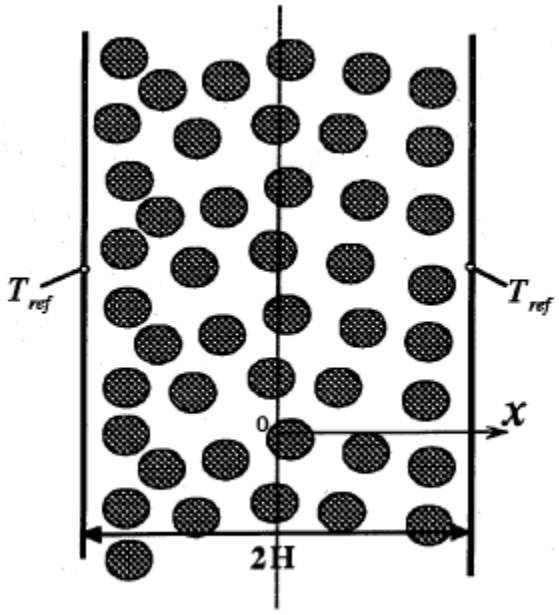

Figure 2.1. Generic Porous Media.

They found that for the first case, the solid and fluid temperatures decrease along the x-direction toward the wall. For the second case, the fluid temperature remained fairly constant, while the solid temperature exponentially increased to approach the fluid temperature along the x-direction toward the wall.

Jiang and Ren [14] used a numerical model including the thermal non-equilibrium assumption to see the effects of viscous dissipation, the boundary condition assumptions, thermal dispersion, particle diameters, and the variable properties of oil on convection heat transfer in steady flow in a porous medium. They found that viscous dissipation weakened the convection heat transfer from the fluid to the wall in the porous media, where the wall was modeled as a constant wall heat flux boundary condition.

The above investigations are representative examples out of a large number of investigations that have studied steady flow in porous media. In comparison, investigations dealing with transient pulsating or periodic flow are few, and include the following.

Guo et al. [15] performed a numerical study of pulsating flow and heat transfer characteristics in a circular pipe partially filled with a porous medium. They utilized the Brinkman-Forchheimer-extended Darcy model for a porous matrix region attached to a pipe wall. From this, they investigated the impacts of the Darcy number, the thickness of porous layer, and the ratio of effective thermal conductivity of the porous material to the fluid, the pulsating frequency, and the amplitude. The study by Guo et al. [15] of course was based on the solution of modeled (i.e. volume-average) conservation equations. The investigation showed that the Nusselt number monotonically increased as the porous layer thickness increased. This is graphically shown in Figure 2.2.

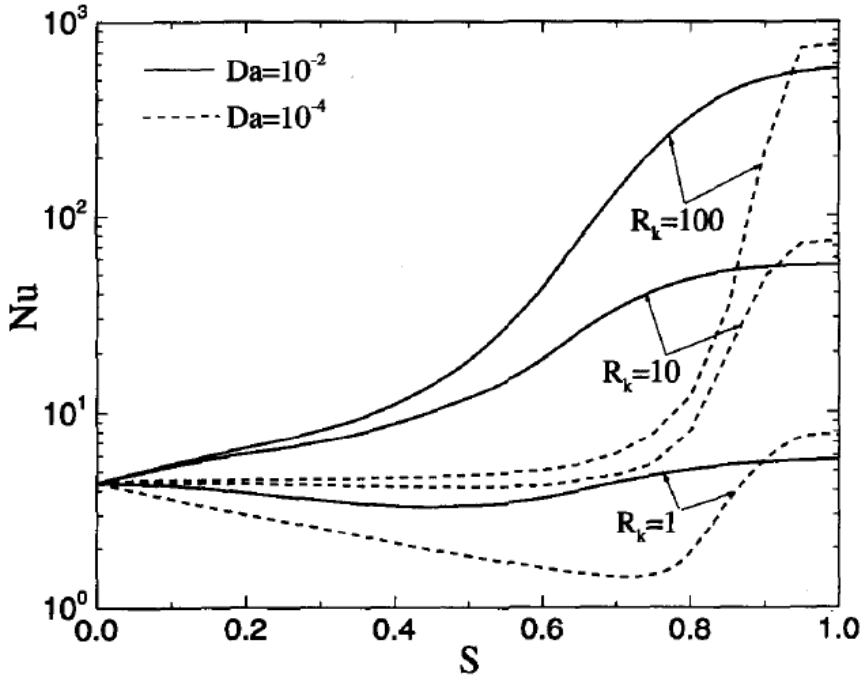

Figure 2.2. Nusselt Number as a Function of Porous Layer Thickness.

Nakayama et al. [16] developed a numerical model for a three-dimensional heat and fluid flow through a bank of infinitely long cylinders in yaw. Figure 2.3 shows a schematic of the porous structure along with a coordinate system they investigated. This investigation is one among several pore-level direct numerical simulations that latter

authors had investigated over the past several years. Their simulation results lead to the development of a permeability tensor and Forchheimer tensor. These results can be used in order to investigate complex flow and heat transfer characteristics associated with manmade structures such as fins.

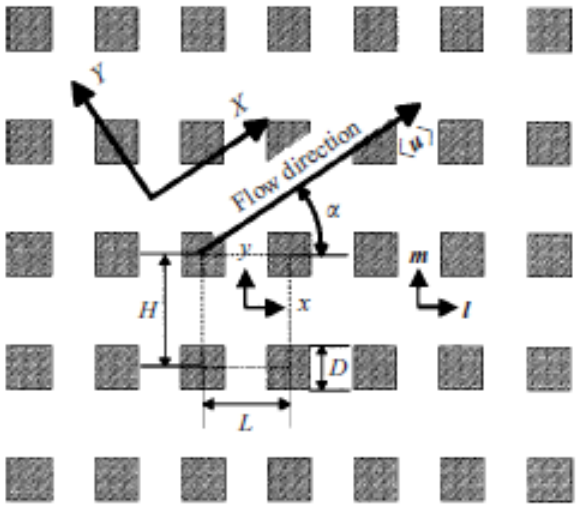

Figure 2.3. Porous Structure with Coordinate System.

An industrial application where porous media analysis becomes suitable and handy is the flow in tube bundles in large heat exchangers, or flow through pin fins. The very large number of spatially-periodic tube or pin fin unit cells makes the application of porous-media methods to these applications convenient as well as justifiable.

Recently, Benarji et al [17] developed transient numerical simulations of fluid flow and heat transfer over a bank of flat tubes for both in-line and staggered configurations for isothermal and isoflux boundary conditions. From this, they investigated the effect of Reynolds number, Prandtl number, length ratio, and the height ratio on the Nusselt number. They found that at a particular Reynolds number and Prandtl number, the Nusselt number decreased as the length of the investigated unit cell

increased. However, the Nusselt number increased as the height of the unit cell increased, for the same conditions.

These investigations prove the usefulness of direct numerical simulations when studying flow and thermal energy phenomena on the pore-scale.

2.3 Regenerator and Cryocooler Applications

An important application where periodic flow of a gas occurs in a porous structure is regenerative cryocoolers. Regenerative cryocoolers include Stirling and pulse tube cryocoolers. The regenerator, which is a porous component in cryogenic coolers have been of much interest, especially for military tactical and space based applications. The following is a listing of some recent cryocooler research studies that are relevant to this investigation.

Currently, the miniaturization of cryocoolers is of great interest. The root for this interest is the critical importance of small volume and light weight in satellite-based applications. To this end, Garaway et al. [18] have developed a miniature, high energy density pulse tube cryocooler that can appropriately provide cooling for size-limited cryogenic applications that demand fast cool down. The regenerator in their investigation was made of #635 stainless steel woven mesh with a porosity of 60%. By performing an optimization study, there results indicated that it was necessary to limit the operating frequency at 200 Hz, in order to ensure a sufficient ratio between the thermal penetration depth and hydraulic diameter. This study reveals how important the mesh porosity and hence regenerator can be to the entire cryocooling system.

Cha et al. [19] examined the adequacy of pulse tube cryocoolers being modeled as one-dimensional flow fields. To test this, they modeled and tested two entire inertance tube pulse tube refrigerator systems which were operating under various thermal boundary conditions using a computational fluid dynamics code. They were able to prove that a one-dimensional analysis is adequate when all components of the inertance tube pulse tube refrigerator have a large length to diameter ratio.

Cha et al. [20] studied the measurement and correlation of anisotropic hydrodynamic parameters of the most widely used cryocooler regenerator fillers. They tested stainless steel 400 mesh screens, stainless steel 325 mesh screens, stainless steel 400 mesh sintered filler, stainless steel sintered foam metal, and nickel micro-machined disks. CFD assisted methodology was used for the analysis and interpretation of the measured data. They were able to compare the magnitudes of oscillatory flow friction factors to steady flow friction factors at particular Reynolds number values for each of the regenerator fillers. Their results are presented in Figure 2.4.

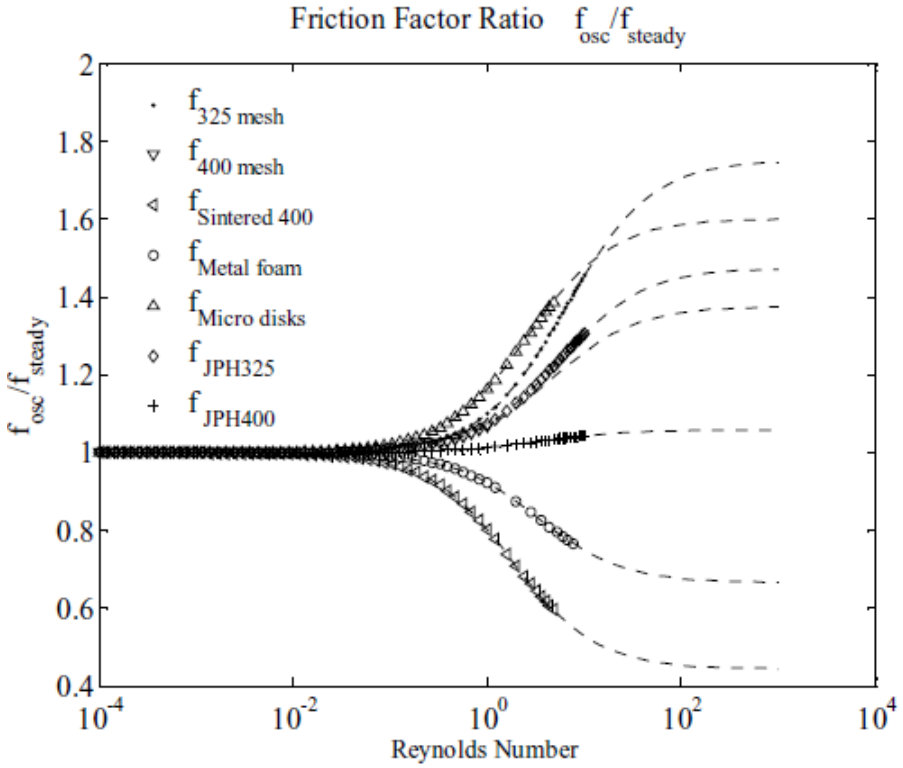

Figure 2.4. Friction Factor Study.

Clearman et al [21] measured and correlated the hydrodynamic parameters associated with steady longitudinal and radial flow of helium in many widely-used pulse tube and Stirling cryocooler regenerator fillers. They determined that for 325 mesh screens, a higher porosity results in a lower relative pressure drop within the regenerator.

Many other researchers have also specifically studied the regenerators in cryocooling systems because of the effect they have on the entire cryogenic system performance, including [22-35]: Nam and Jeong, 2007; Clearman, 2007; Cha, Ghiaasiaan, and Desai, 2006; Sahoo and Das, 1994; Guo et al., 1987; Erk and Dudukovic, 1997; Bubnovich, and Gonzalez, 2005; Ogawa et al., 1990; Willmott, 1964; Hua and Zhong, 1988, Radebaugh et al., 2002; de Waele and Zeegers, 2002; Yuan and Jing-Tao, 2002; and Popescu et al., 2001.

Although the findings of the above investigators have lead to new product development and important regenerator insights, the pore scale phenomena for transient flow through a regenerator has yet to be understood.

2.4 Closing Remarks

In closing, the literature survey revealed that the fundamental pore-level transient flow phenomenon in porous media is not well understood, primarily because these phenomena are difficult to experimentally study. Therefore, researchers have used numerical models and techniques to examine the details of the thermal-fluid effects. As an alternative to experiments, direct numerical simulation models are used to exactly solve the pore-level mass, momentum, and energy equations without making any simplifying assumptions. Such investigations have produced valuable insight about pore-level phenomena in steady-flow. No systematic study has been reported for periodic flow, however.

In cryogenic systems, specifically pulse tube and Stirling cryocoolers, the regenerator component is very important. However, pore-level details of the regenerator are still quite poorly understood. The goal of this study is to understand the micro scale thermal energy effects of pulsating flow within a porous medium using direct numerical simulation. Investigations addressing periodic flow will be performed in the future.

CHAPTER 3

SIMULATED SYSTEM

3.1 Computational Model

The computational model studied in this investigation consists of two dimensional arrays of rectangular cylinders. This simulated system along with the coordinate system and flow direction is shown in Figure 3.1.

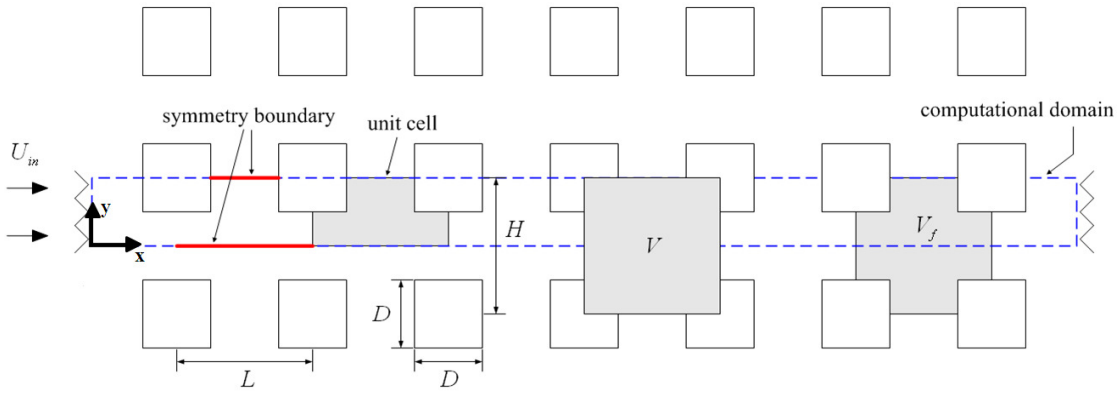

Figure 3.1. The Simulated System [12].

Previous researchers typically studied the flow details in a single unit cell, using periodic boundary conditions. However, for pulsating flow, a single unit cell is not sufficient due to the entrance effect complications and the development of phase shift which makes simple periodic boundary conditions along the main flow direction unsuitable [36]. Therefore, the generic computational domain for this study is composed

of six consecutive unit cells in series.

The upper and lower surfaces of each unit cell consist of a symmetry boundary condition in order to optimize the computational processing efficiency by reducing the number of grid points. This is justified since the flow about the x-axis for the entire computation domain is symmetric.

The square cylinders in this study were set to have an aspect ratio of $H/L = 1$, with $H = 10\ mm$. The dimension D was parametrically changed in order to adjust the porosity. V and V_f represent the total volume and the volume of the fluid, respectively, in each unit cell. The porosity of the structure can be found from,

$$\varepsilon = 1 - \left(\frac{D}{L}\right)^2 \tag{3.1}$$

where:

D = Cylinder diameter

L = Unit cell length

Previous studies indicate that the end effects of the simulated row of the unit cells essentially disappear after the first few unit cells with the addition of beginning and ending buffer zones and setting the inlet flow velocity to the entrance of the beginning buffer zone [36]. Following a recommendation by Kim [36], the buffer zone at the inlet has a length of $2L$, but a longer buffer length of $7L$ was used at the exit to eliminate the outflow boundary condition. The flow details of the fifth unit cell were used in the computations so that all end effects were mitigated. The entire computational domain with the buffer zones is shown in Figure 3.2.

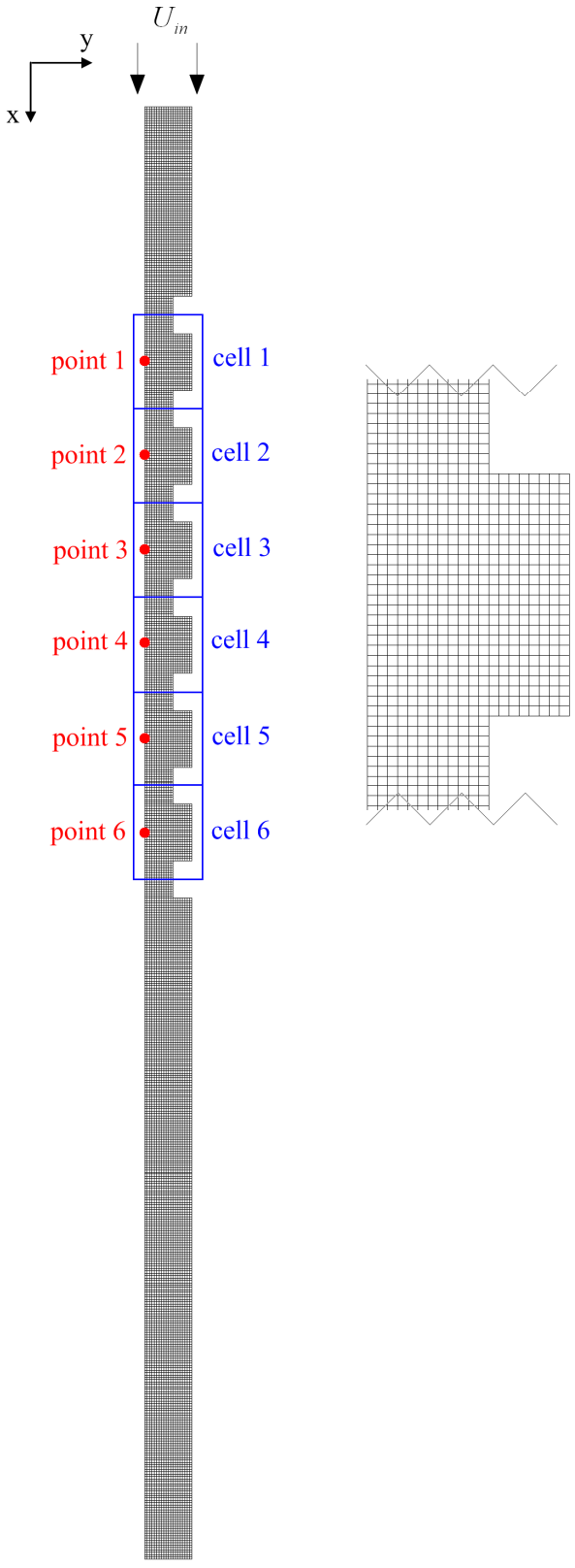

Figure 3.2. Computational Domain with Buffer Zones [36].

Figures 3.3, 3.4, and 3.5 display the dimensions of the generic porous structure geometries considered in this analysis, which include porosities of 64%, 75%, and 84%, respectively, where all dimensions are in millimeters.

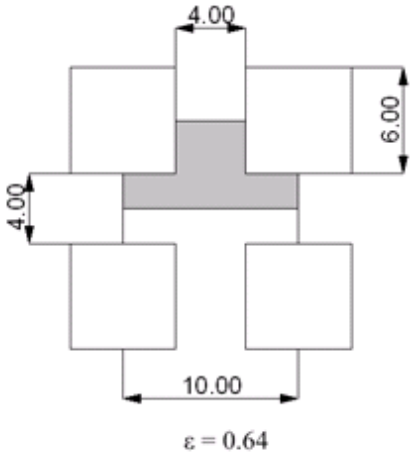

Figure 3.3. 64% Porosity [12].

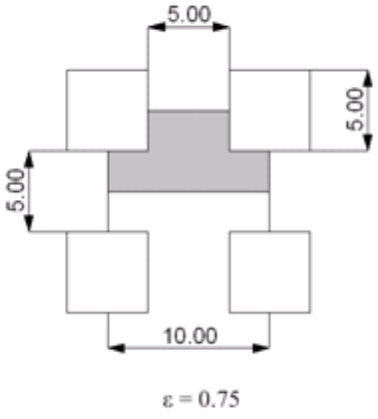

Figure 3.4. 75% Porosity [12].

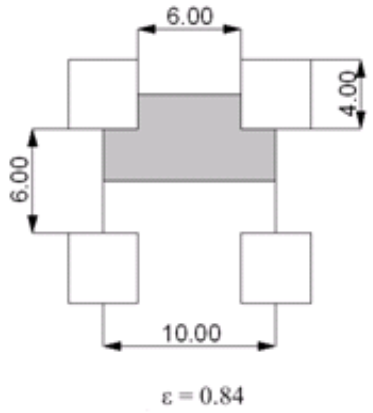

Figure 3.5. 84% Porosity [12].

The porous structures all contain a fixed unit cell length of 10 mm. The square rod size *D*, was varied from 6 mm to 4 mm for 64% porosity to 84% porosity, respectively.

3.2 Grid Convergence and Meshing Scheme

The entire computational domain was meshed in Gambit [37] with a 20×40 per unit cell grid structure in order to ensure that convergence was achieved. To ensure the adequacy of the nodalization, selected simulations were repeated using a 40x80 per unit cell grid structure. Results from the grid convergence tests, which confirmed that the simulation outcome was grid independent, are shown in later chapters.

CHAPTER 4

THEORY

4.1 Flow Regime

Turbulent flow can occur in porous media. The hydrodynamic conditions that lead to the onset of turbulent flow under steady flow conditions have been investigated in the past [9]. Little is known about turbulent flow in porous media under pulsating or periodic flow, however. Consequently, due to the apparent lack of directly-applicable information, steady flow criterion is used for the onset of turbulent flow regime.

To ensure that the flow field was indeed within the laminar flow regime, two different Reynolds numbers were defined and used. The pore – based Reynolds number is defined as,

$$\mathrm{Re}_K = \frac{\rho_f \left| \left\langle \vec{u} \right\rangle \right| \sqrt{K}}{\mu_f} \tag{4.1}$$

where:

K = Permeability coefficient along x direction

ρ_f = Fluid density

$\left|\left\langle \vec{u} \right\rangle\right|$ = Volume-average fluid velocity

μ_f = Fluid dynamic viscosity

As noted, the length scale in this definition is the square root of permeability. For steady flow, laminar flow regime is maintained as long as the value of the Reynolds number is at or below 300 [9].

The above definition for Re_K requires knowledge about permeability, which may not be known a priori. An alternative pore-level definition is,

$$\mathrm{Re}_L = \frac{\rho_f \left|\left\langle \vec{u} \right\rangle\right| L}{\mu_f} \tag{4.2}$$

where, as noted, the length scale is the physical dimension of a unit cell in the direction of the main flow.

This study investigated a range of unit cell length-based Reynolds numbers from 0 to 1000. All unit cell length-based Reynolds numbers considered were in the laminar regime according to the pore-based Reynolds number criterion, however.

4.2 Volume-Average Governing Equations

As mentioned earlier, numerical simulations when the pore details are resolved are not practical for common design and analysis calculations, because of the

prohibitively large computation times. Furthermore, pore geometries are often complex and non-uniform, rendering direct simulations as even more problematic.

Tractable conservation equations for flow in porous media can be derived, however, by volume-averaging of the local and instantaneous conservation equations [8], or by simply postulating model transport equations [10]. These tractable conservation equations are not concerned with pore-level phenomena, and deal with macroscopic flow and transport processes instead.

Volume-averaged conservation equations can be derived rigorously, starting from the local and instantaneous differential conservation equations [38, 8].

The formulations of the volume-average governing equations that are presented in this section are consistent with commonly used porous media literatures, including Whittaker [38], Nakayama, Kuwahara, and Kodama [13], and Kim and Ghiaasiaan [12]. Any volume-average fluid property can be found from,

$$\langle \phi \rangle^f = \frac{1}{V_f} \int_{V_f} \phi \, \mathrm{d}V \tag{4.3}$$

where:

ϕ = Any fluid property

V_f = Fluid volume

Now, consider the flow of an incompressible fluid in a porous medium. The local and instantaneous mass, momentum, and energy conservation equations will then be,

$$\frac{\partial u_j}{\partial x_j} = 0 \tag{4.4}$$

$$\frac{\partial u_i}{\partial t} + \frac{\partial}{\partial x_j} u_j u_i = -\frac{1}{\rho}\frac{\partial p}{\partial x_i} + \frac{\partial}{\partial x_j}\nu_f \left(\frac{\partial u_i}{\partial x_j} + \frac{\partial u_j}{\partial x_i} \right) \tag{4.5}$$

$$\rho_f c_{pf} \left(\frac{\partial T}{\partial t} + \frac{\partial}{\partial x_j} u_j T \right) = \frac{\partial}{\partial x_j} \left(k_f \frac{\partial T}{\partial x_j} \right) \tag{4.6}$$

where:

u_j = Velocity vector

ν_f = Fluid kinematic viscosity

t = Time

c_{pf} = Fluid specific heat

k_f = Fluid thermal conductivity

T = Temperature

Any fluid property can be separated into a volume-average fluid property term and a spatial deviation term,

$$\phi = \langle \phi \rangle^f + \tilde{\phi} \tag{4.7}$$

where:

$\tilde{\phi}$ = Spatial deviation of fluid property ϕ

Volume-averaging is now applied to all of the terms in the above conservation equations. The mass conservation equation will give,

$$\frac{\partial \langle u_j \rangle^f}{\partial x_j} = 0 \tag{4.8}$$

Note that Einstein's summation notation has been used.

The model, volume-average fluid momentum conservation equation will give,

$$\begin{aligned} &\frac{\partial \langle u_i \rangle^f}{\partial t} + \frac{\partial}{\partial x_j} \langle u_j \rangle^f \langle u_i \rangle^f = -\frac{1}{\rho} \frac{\partial \langle p \rangle^f}{\partial x_i} \\ &+ \frac{\partial}{\partial x_j} \nu_f \left(\frac{\partial \langle u_i \rangle^f}{\partial x_j} + \frac{\partial \langle u_j \rangle^f}{\partial x_i} \right) - \frac{\nu_f}{K} \varepsilon \langle u_i \rangle^f - b\varepsilon^2 \left(\langle u_k \rangle^f \langle u_k \rangle^f \right)^{\frac{1}{2}} \langle u_i \rangle^f \end{aligned} \tag{4.9}$$

where:

b = Forchheimer constant

The volume-average fluid energy conservation equation will be,

$$\begin{aligned} &\varepsilon \rho_f c_{pf} \left(\frac{\partial \langle T \rangle^f}{\partial t} + \frac{\partial}{\partial x_j} \langle u_j \rangle^f \langle T \rangle^f \right) = \\ &\frac{\partial}{\partial x_j} \left(\varepsilon k_f \frac{\partial \langle T \rangle^f}{\partial x_j} + \frac{k_f}{V} \int_{A_{\text{int}}} T n_j \mathrm{d}A - \varepsilon \rho_f c_{pf} \left\langle \tilde{u}_j \tilde{T} \right\rangle^f \right) + \frac{1}{V} \int_{A_{\text{int}}} k_f \frac{\partial T}{\partial x_j} n_j \mathrm{d}A \end{aligned} \tag{4.10}$$

where:

$\langle T \rangle^f$ = Volume-average fluid temperature

n_j = Unit vector pointing out from the fluid into the solid

A_{int} = Solid-fluid interface area

$\varepsilon\rho_f c_{pf}\left\langle \tilde{u}_j \tilde{T} \right\rangle^f$ = Volume-average thermal dispersion

The term $\frac{\partial}{\partial x_j}\frac{k_f}{V}\int_{A_{\text{int}}} T n_j \mathrm{d}A$ is called the tortuosity term. It vanishes when the surface temperature is uniform. The third term in the bracket on the right side of the above equation represents thermal dispersion. The thermal dispersion represents the amount of energy a fluid particle loses or gains in a unit cell due to momentum transfer and thermal energy storage. The last term on the right side represents the solid-fluid (interfacial) heat transfer.

Consistent with the volume-averaging concept, the average interfacial heat transfer coefficient may be defined by writing,

$$\frac{1}{V}\int_{A_{\text{int}}} k_f \frac{\partial T}{\partial x_j} n_j \mathrm{d}A = a_f h_f \left(\langle T \rangle^s - \langle T \rangle^f \right) \tag{4.11}$$

where:

a_f = Specific area

h_f = Heat transfer coefficient (also called convection coefficient)

$\langle T \rangle^s$ = Volume-average solid surface temperature

The interfacial heat transfer coefficient (Equation 4.11) can be substituted into the fluid energy conservation equation (Equation 4.10) and the resulting simplified thermal energy conservation equation becomes,

$$\varepsilon\rho_f c_{pf}\left(\frac{\partial\langle T\rangle^f}{\partial t}+\frac{\partial}{\partial x_j}\langle u_j\rangle^f\langle T\rangle^f\right)= \\ \frac{\partial}{\partial x_j}\left(\varepsilon k_f\frac{\partial\langle T\rangle^f}{\partial x_j}-\varepsilon\rho_f c_{pf}\left\langle\tilde{u}_j\tilde{T}\right\rangle^f\right)-a_f h_f\left(\langle T\rangle^f-\langle T\rangle^s\right) \tag{4.12}$$

The volume-average governing equations described in this section consider the fluid to be incompressible and have constant properties.

4.3 Calculated Parameters

Pore-scale calculations are performed by numerically solving Equations 4.8, 4.11, and 4.12 in the domain displayed in Figure 3.2. These detailed solutions are done using Fluent [39].

Using the aforementioned Fluent CFD simulations, the heat transfer coefficient was found using Equation 4.11. The heat transfer coefficient was then used, along with the unit cell length to calculate a cell-based Nusselt number. The Nusselt number is defined here as,

$$Nu_L=\frac{hL}{k_f} \tag{4.13}$$

The thermal dispersion was also derived from this study by using the pore-level detailed numerical simulation results. The thermal dispersion term is defined here as,

$$D_T = \varepsilon \rho_f c_{pf} \left\langle \tilde{u}_j \tilde{T} \right\rangle^f \tag{4.14}$$

The thermal dispersion term was non-dimensionalized by writing,

$$D_T^* = \frac{\varepsilon \rho_f c_{pf} \left\langle \tilde{u}_j \tilde{T} \right\rangle^f}{\rho c_p \varepsilon u_{\max} L \left(\left\langle \frac{dT}{dx} \right\rangle \right)} \tag{4.15}$$

where k_{tor} and k_{disp} represent the contributions of tortuosity and thermal dispersion.

This equation compares the thermal dispersion term to the maximum change in stored thermal energy in the fluid as it moves from one unit cell to another. The temperature gradient was found by applying the central differencing scheme in unit cell 5, using data from unit cell 4 and unit cell 6 in the simulated system.

For steady flow in porous media, model volume-average conservation equations are often represented in terms of an effective fluid thermal conductivity by writing,

$$k_{eff} = k_f + k_{tor} + k_{disp} \tag{4.16}$$

Accordingly, the dispersion thermal conductivity can be defined as,

$$k_{disp} = \frac{\varepsilon \rho_f c_{pf} \left\langle \tilde{u}_j \tilde{T} \right\rangle^f}{\varepsilon \left\langle \frac{dT}{dx} \right\rangle} \tag{4.17}$$

Once the volume-average and cycle-average heat transfer coefficient and the thermal dispersion term are found from detailed pore-level simulations, they must satisfy the macroscopic model equation represented by Equation 4.12. This was tested for selected runs in order to ensure the consistency and correctness of the calculation procedures.

The average heat transfer coefficient, Nusselt number, thermal dispersion, non-dimensional thermal dispersion, and dispersion thermal conductivity were all calculated for frequencies of 0 to 100 Hz, porosities of 64% to 84%, and Reynolds numbers (Re_L) of 0 to 1000. The resulting data is presented and discussed in the next chapter.

4.4 Inlet, Initial, and Boundary Conditions

The inlet velocity profile to the simulated system represents pulsating flow and is represented as,

$$U_{in} = U_m \left[1 + a \sin\left(2\pi f t\right)\right] \tag{4.18}$$

where:

U_m = Mean fluid velocity for pulsating flow

a = Flow pulsation amplitude

f = Pulsation frequency

This velocity function, computationally inputted as a user defined function, is shown in detail in Appendix A. As previously stated, the inlet boundary is located a distance $2L$ upstream from the first unit cell. The mean fluid velocity varied as a function of the Reynolds number. The flow pulsation amplitude was fixed to a value of $a = 0.4$.

A no-slip boundary condition was applied to the walls, which were at a constant temperature of 300 K. The upper and lower boundary conditions for the simulated six unit cells (Figure 3.1) were set to symmetry conditions (normal gradients of all variable parameters are prescribed as zero) since the physical and geometric boundaries are symmetric about the x-direction. Due to this, only one half of the unit cell domain was actually simulated, making the computations significantly faster. The outlet boundary is at a distance of $7L$ downstream from the sixth unit cell, where a default pressure outlet boundary condition is set and a zero-gradient is imposed for all dependent variables.

For the initial conditions, first a steady-state simulation was performed with U_m as the inlet velocity. The converged steady state results were then used for the transient calculations. The unsteady flow simulations continued until steady periodic conditions were achieved.

For convenience, air, modeled as an incompressible fluid, was the working fluid. In all the simulations, the temperature and pressure at the inlet were assumed to be 200K and 1 bar, respectively. All fluid properties over the entire temperature range were assumed to be constant. These properties are shown in Table 4.1.

Table 4.1. Fluid Properties.

Variable	Description	Values
ρ_f	Density	1.225 [kg/m^3]
k_f	Thermal Conductivity	0.0242 [W/m-K]
c_{pf}	Specific Heat	1006.43 [J/kg-K]
μ_f	Viscosity	1.7894x10^{-5} [kg/m-s]

The pressure-based coupled solution algorithm in Fluent [39] was used to solve the local and instantaneous mass, momentum, and energy conservation equations. The simulation results were post processed in Matlab [40].

CHAPTER 5

RESULTS AND DISCUSSION

5.1 General Remarks

The inlet flow condition in the simulations was that of pulsating flow, as mentioned earlier (Equation 4.18). This resulted in the development of transient velocity and temperatures elsewhere in the simulated system, where pulsations were superimposed on an otherwise steady-state profile. The resulting instantaneous average velocity and temperature profiles for the case of 64% porosity, Reynolds number of Re_L=700, and frequency of f=80 Hz are shown in Figures 5.1 and 5.2, respectively. Each simulation, of course, starts from a system initial condition that represents steady flow. As a result, the system goes through a relatively brief transient before steady-periodic flow conditions are established. The velocity and temperature profile trends are similar to Figures 5.1 and 5.2 for all simulated cases.

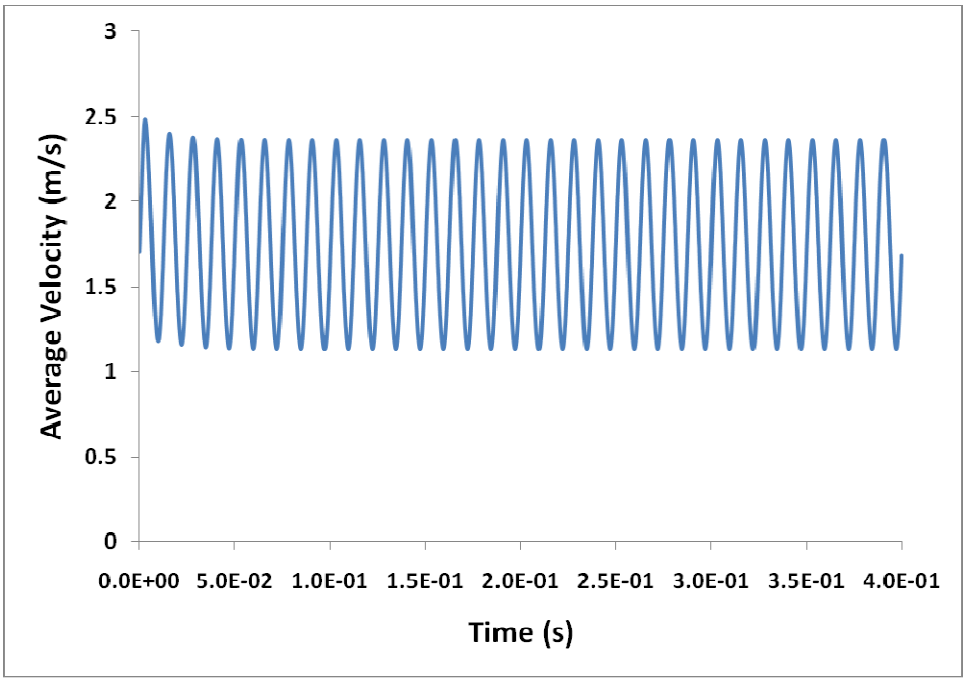

Figure 5.1. Velocity Profile.

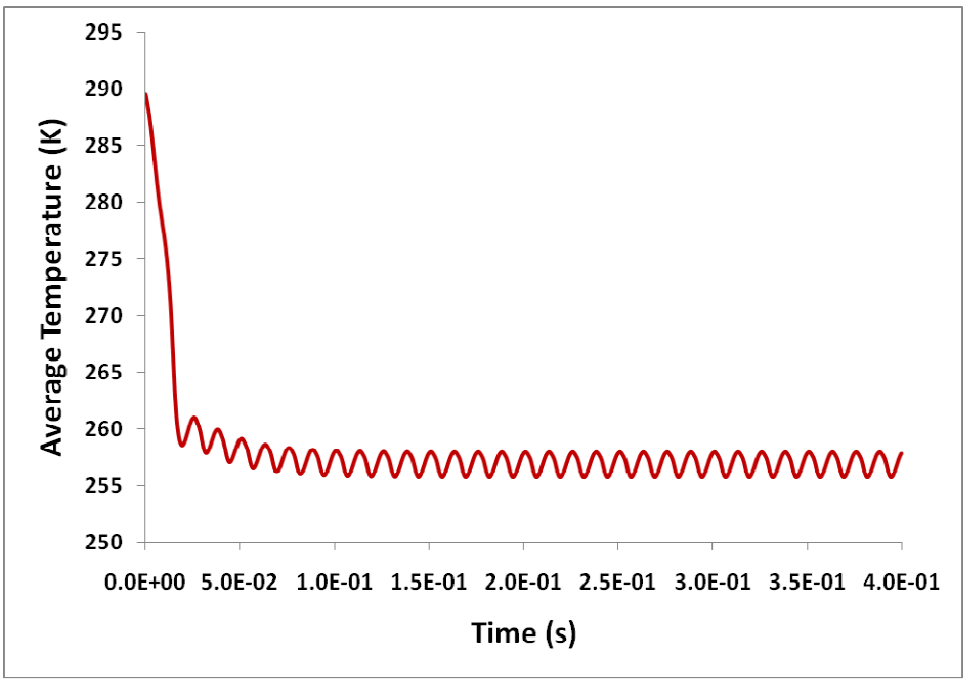

Figure 5.2. Temperature Profile.

.

5.1.1 Convergence

For all numerical simulations, the convergence criterion applied to the residuals for the continuity and momentum equations was a tolerance of 10^{-6}. A convergence criterion of 10^{-8} was used for the energy equation residuals. These tolerance criteria are known to be quite adequate for simulations with Fluent [39].

A grid independence study was also performed. For a 75% porous structure case, for example, two grid systems were studied, one with 20x40 nodes per unit cell, and one with 40x80 nodes per unit cell. The resulting average temperatures were compared. A plot comparing the magnitudes of average temperature for the two grid systems is shown in Figure 5.3. The results were very close to each other. The maximum difference between the two grid systems for the volume-average temperature was within 1.5 K. This grid test agreed well with the grid testing performed earlier by Kim and Ghiaasiaan [12], who investigated the hydrodynamics of essentially the same porous structure in pulsating flow. Therefore, a 20x40 grid system structure was used as it produced similar results to the finer grid system and was computationally more optimal and efficient. The same number of grids was maintained for all of the porous structures and all of the parametric simulations.

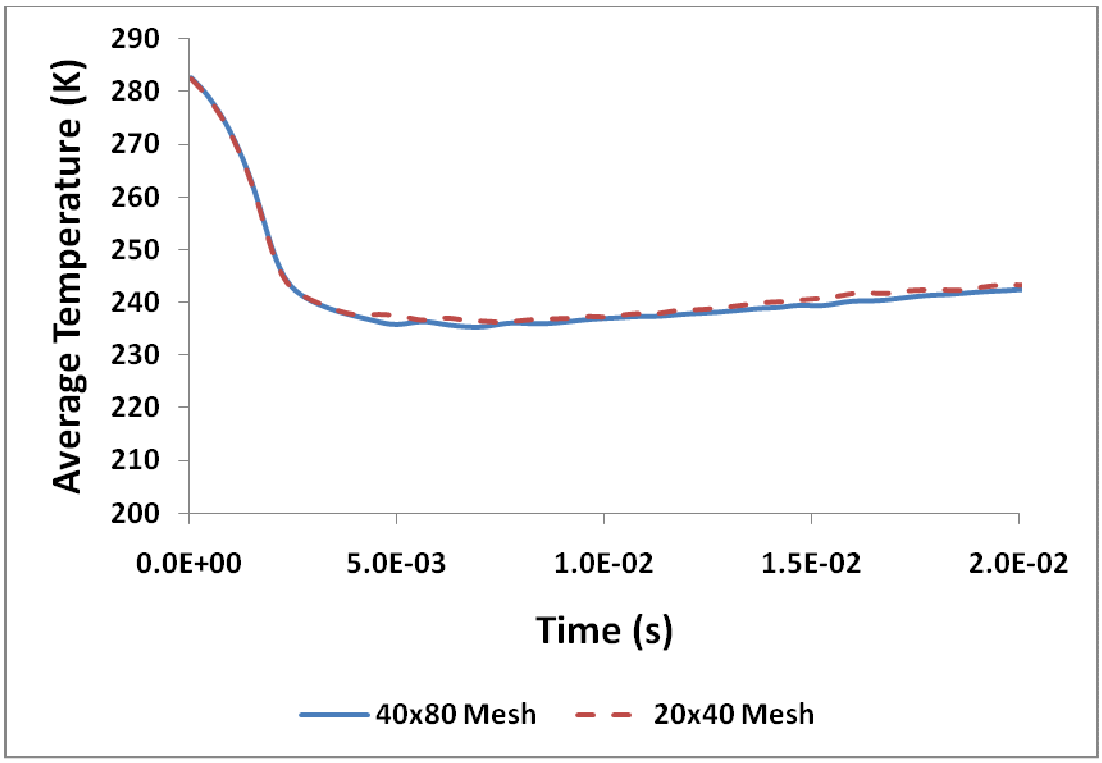

Figure 5.3. Average Temperature Comparison Plot.

5.1.2. Parametric Tests

Parametric simulations were performed where the cycle-average heat transfer coefficient, Nusselt number, thermal dispersion, non-dimensional thermal dispersion, and dispersion thermal conductivity were found for the following parametric ranges:

- porosities in the range of 64% to 84%
- Reynolds numbers (Re_L) in the range of 0 to 1000
- frequencies in the range of 0 to 100 Hz

The details of the varied parameters and calculated variables are shown in Tables 5.1 and 5.2, respectively.

Table 5.1. Varied Parameters.

Run #	**Re_L**	**f (Hz)**	**ε (%)**
1	70	0	64
2	140	0	64
3	280	0	64
4	420	0	64
5	560	0	64
6	700	0	64
7	840	0	64
8	980	0	64
9	70	20	64
10	140	20	64
11	280	20	64
12	420	20	64
13	560	20	64
14	700	20	64
15	840	20	64
16	980	20	64
17	70	40	64
18	140	40	64
19	280	40	64
20	420	40	64
21	560	40	64
22	700	40	64
23	840	40	64
24	980	40	64
25	70	64	64
26	140	64	64
27	280	64	64
28	420	64	64
29	560	64	64
30	700	64	64
31	840	64	64
32	980	64	64
33	70	80	64
34	140	80	64
35	280	80	64
36	420	80	64
37	560	80	64
38	700	80	64
39	840	80	64
40	980	80	64
41	70	100	64
42	140	100	64

Table 5.1 continued

43	280	100	64
44	420	100	64
45	560	100	64
46	700	100	64
47	840	100	64
48	980	100	64
49	70	0	75
50	140	0	75
51	280	0	75
52	420	0	75
53	560	0	75
54	700	0	75
55	840	0	75
56	980	0	75
57	70	20	75
58	140	20	75
59	280	20	75
60	420	20	75
61	560	20	75
62	700	20	75
63	840	20	75
64	980	20	75
65	70	40	75
66	140	40	75
67	280	40	75
68	420	40	75
69	560	40	75
70	700	40	75
71	840	40	75
72	980	40	75
73	70	64	75
74	140	64	75
75	280	64	75
76	420	64	75
77	560	64	75
78	700	64	75
79	840	64	75
80	980	64	75
81	70	80	75
82	140	80	75
83	280	80	75
84	420	80	75
85	560	80	75

Table 5.1 continued

86	700	80	75
87	840	80	75
88	980	80	75
89	70	100	75
90	140	100	75
91	280	100	75
92	420	100	75
93	560	100	75
94	700	100	75
95	840	100	75
96	980	100	75
97	70	0	84
98	140	0	84
99	280	0	84
100	420	0	84
101	560	0	84
102	700	0	84
103	840	0	84
104	980	0	84
105	70	20	84
106	140	20	84
107	280	20	84
108	420	20	84
109	560	20	84
110	700	20	84
111	840	20	84
112	980	20	84
113	70	40	84
114	140	40	84
115	280	40	84
116	420	40	84
117	560	40	84
118	700	40	84
119	840	40	84
120	980	40	84
121	70	64	84
122	140	64	84
123	280	64	84
124	420	64	84
125	560	64	84
126	700	64	84
127	840	64	84
128	980	64	84

Table 5.1 continued

129	70	80	84
130	140	80	84
131	280	80	84
132	420	80	84
133	560	80	84
134	700	80	84
135	840	80	84
136	980	80	84
137	70	100	84
138	140	100	84
139	280	100	84
140	420	100	84
141	560	100	84
142	700	100	84
143	840	100	84
144	980	100	84

Table 5.2. Calculated Variables.

Parameter	Variable
Heat Transfer Coefficient [W/m^2-K]	h
Nusselt Number [-]	Nu_L
Thermal Dispersion [W/m^2]	D_T
Non-Dimensional Thermal Dispersion [-]	D_T^*
Dispersion Thermal Conductivity [W/m-K]	k_{disp}

Unless otherwise stated, all presented variables are calculated as volume-average and cycle-average quantities. The results obtained from this parametric analysis are presented and discussed in the following sections.

5.2 Convection Heat Transfer

5.2.1 Solid-Fluid Heat Transfer Coefficients

Using Equations 4.11 and 4.12, the average heat transfer coefficients were determined for the range of Reynolds numbers, porosities, and frequencies shown in Table 5.1. The heat transfer coefficients at given Reynolds numbers are plotted against frequency for three unit cell porosities. Figures 5.4, 5.5, and 5.6, show these values for unit cell porosities of 64%, 75%, and 84%, respectively.

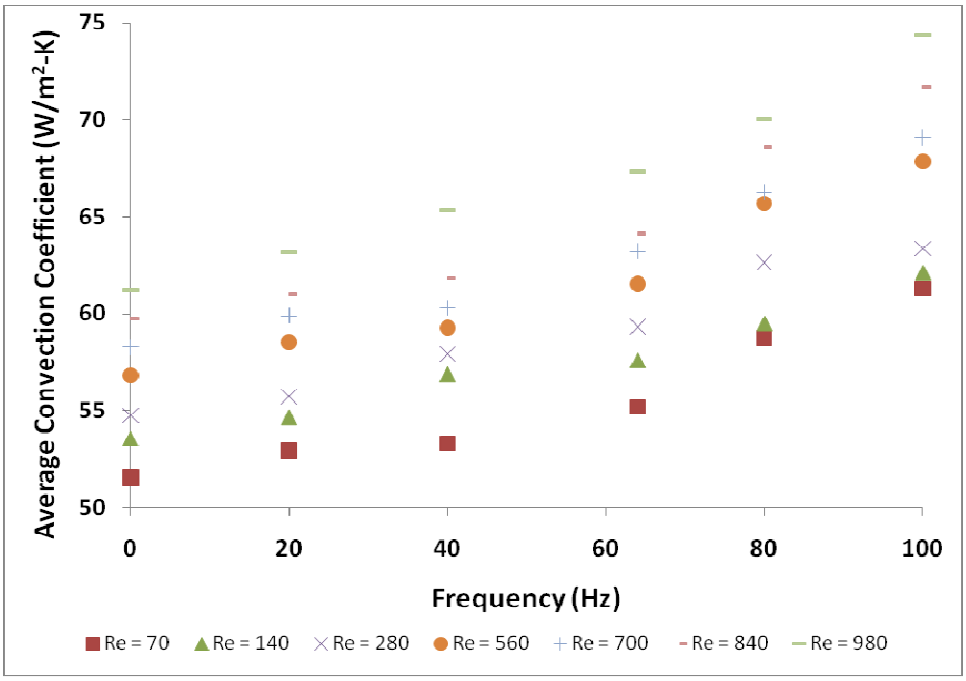

Figure 5.4. 64% Porosity – Heat Transfer Coefficient vs. Frequency.

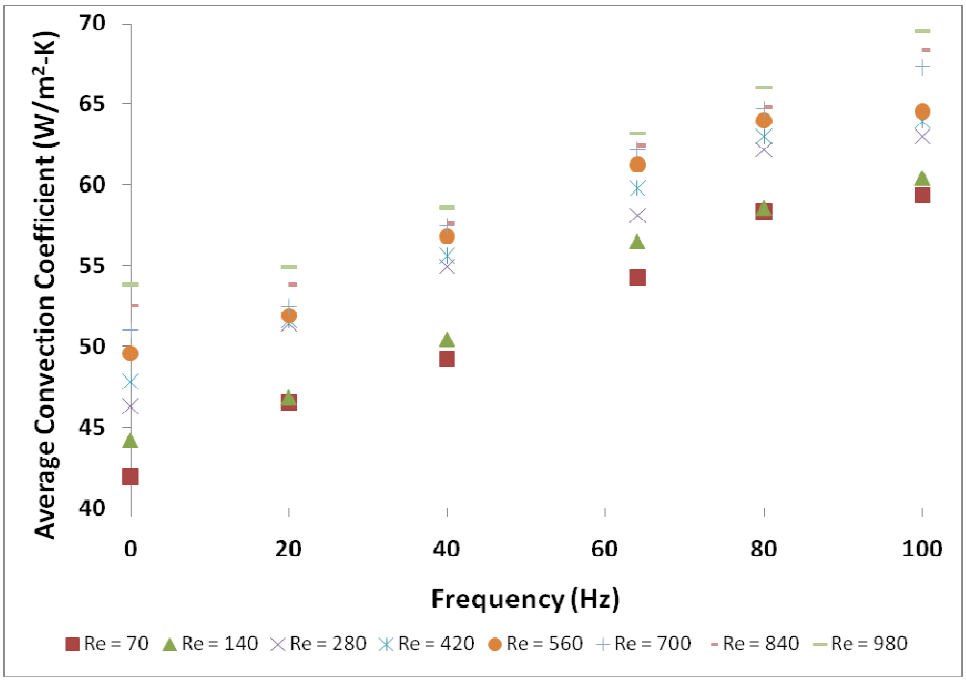

Figure 5.5. 75% Porosity – Heat Transfer Coefficient vs. Frequency.

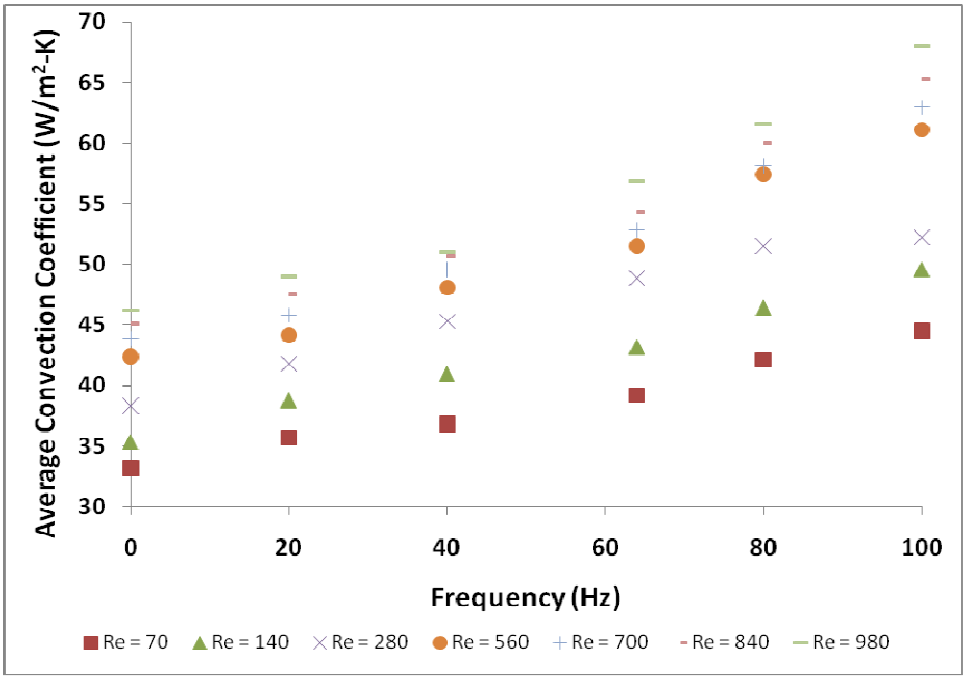

Figure 5.6. 84% Porosity – Heat Transfer Coefficient vs. Frequency.

It is noticed that the average heat transfer coefficient monotomically increases as the frequency increases for all unit cell porocities and Reynolds numbers. The Reynolds numbers used in the above plots and for all forthcoming plots is the unit cell-based Reynolds number. For each porosity, the higher the Reynolds number, the higher the average heat transfer coefficient. Finally, within the tested range of porosities the magnitude of the average convection heat transfer coefficient increases as the porosity decreases.

Figure 5.7 compares the volume-average and cycle-average heat transfer coefficients for unit cells 3, 4, and 5 for a typical run (ε=0.64, Re_L=700). The behavior of the displayed three unit cells is essentially identical, confirming the adequacy of the assumptions that for these unit cells there are negligible system end effects.

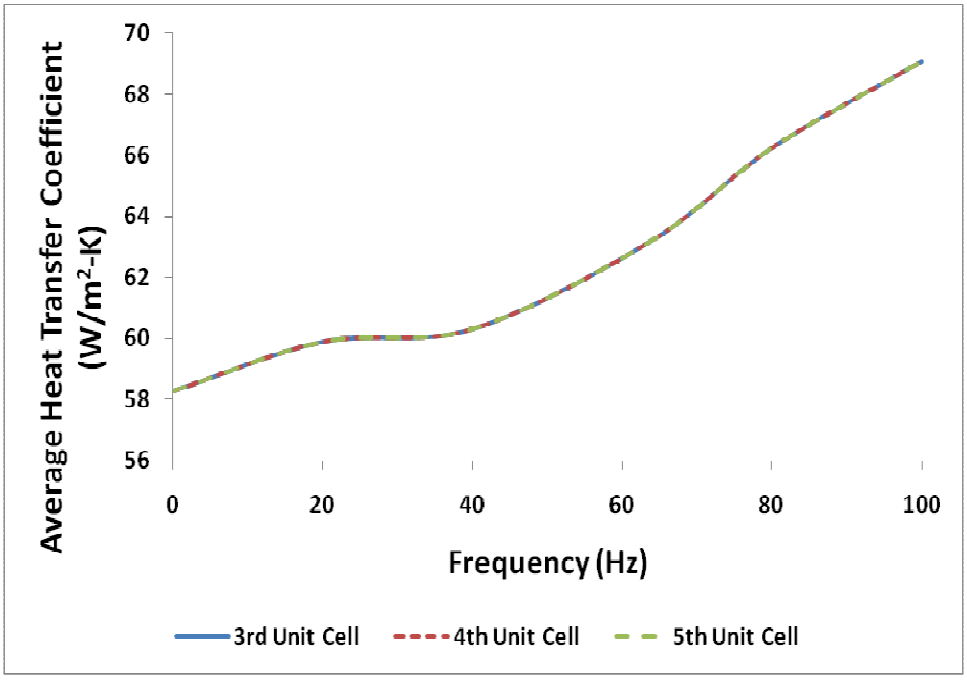

Figure 5.7. Unit Cell Heat Transfer Coefficients.

Figure 5.8 displays the instantaneous, unit cell-average heat transfer coefficient for a typical simulation (ε=0.64, Re_L=700, f=80). As expected, the unit cell-average heat transfer coefficient is varys in response to the flow pulsations. The relative magnitude of pulsations in the average heat transfer cofficient is about 7% for the displayed run, indicating the significance of the effect of flow pulsations on the heat transfer ceofficient.

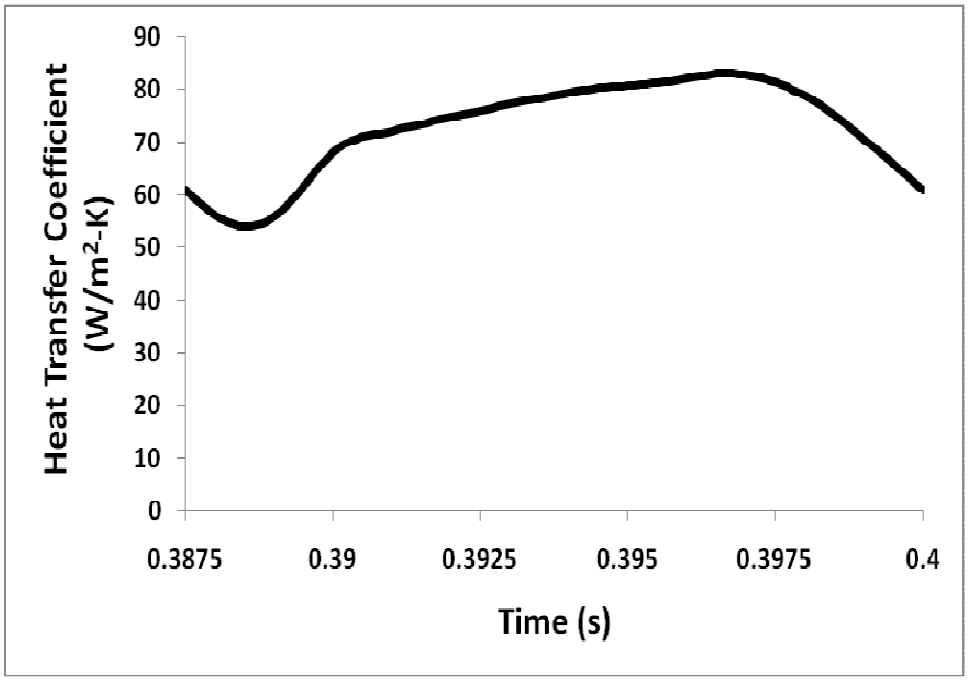

Figure 5.8. Instantaneous, Unit Cell-Average Heat Transfer Coefficient.

5.2.2 Nusselt Numbers

Once the volume and cycle-average heat transfer coefficient was determined, the average Nusselt number was found by using Equation 4.13. The results are shown in Figures 5.9, 5.10, and 5.11. The results are also displayed in several different parametric

forms in Appendix B to better clarify the parametric trends. Consistent trends are noticed for the Nusselt numbers, when they are compared to the heat transfer coefficient.

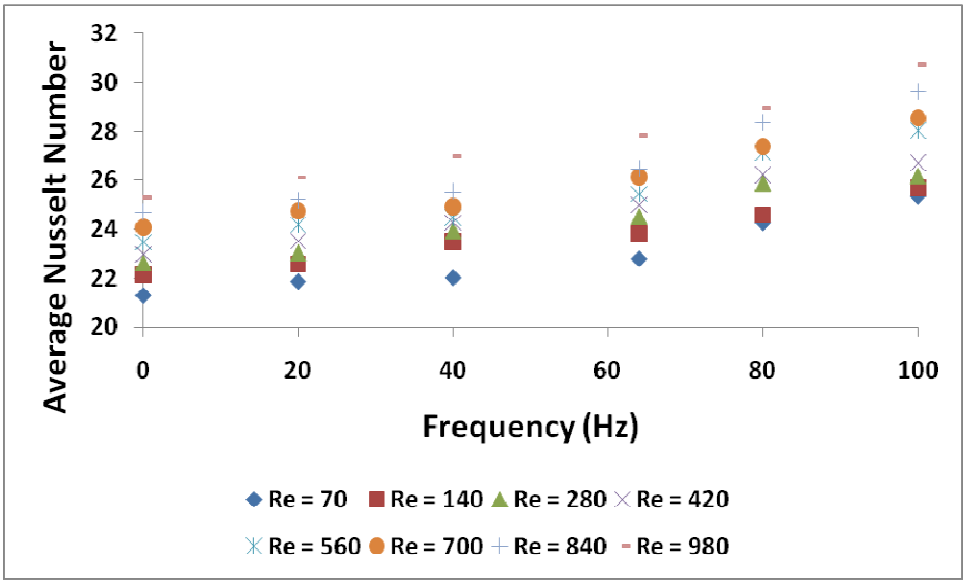

Figure 5.9. 64% Porosity – Nusselt Number vs. Frequency.

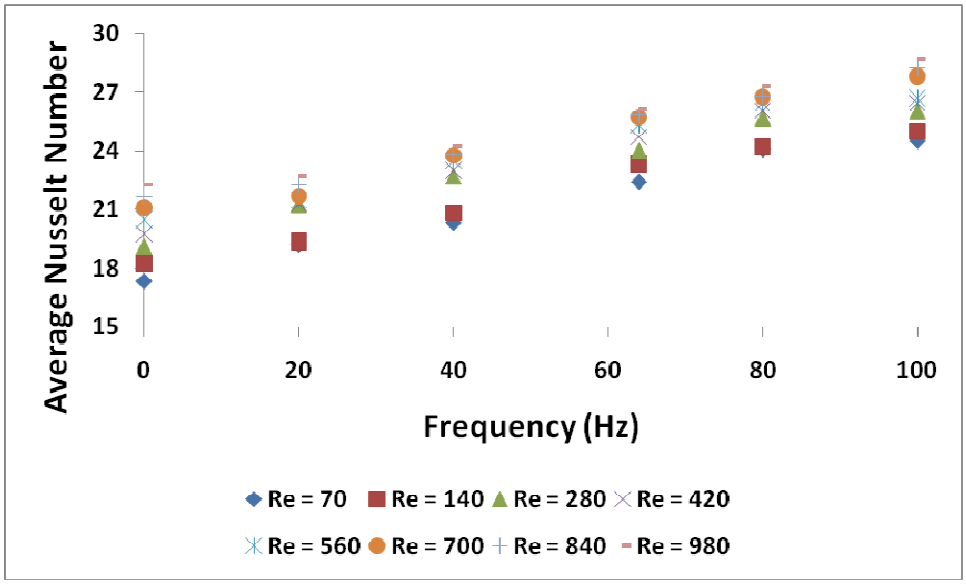

Figure 5.10. 75% Porosity – Nusselt Number vs. Frequency.

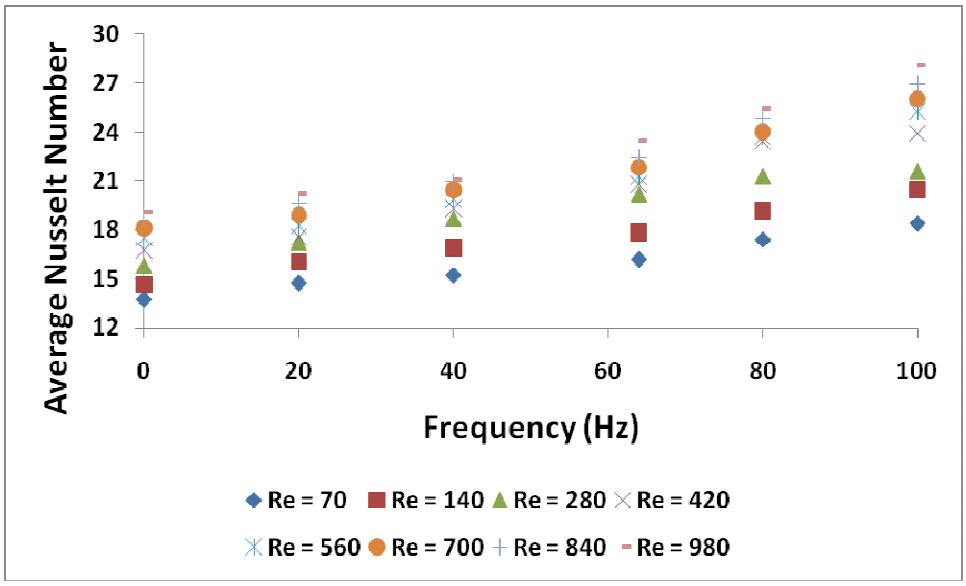

Figure 5.11. 84% Porosity – Nusselt Number vs. Frequency.

Within the tested parameter range, the average Nusselt number: increases as the frequency increases for all unit cell porocities and Reynolds numbers, increases as the Reynolds number increases for all unit cell porosities and frequencies, and decreases as the unit cell porosity increases for all Reynolds numbers and frequencies.

Figures 5.12 through 5.14 are similar to Figures 5.8 to 5.10, when the horizontal coordinate is now a unit cell length-based Valensi number, which is a frequency – dependent dimensionless parameter.

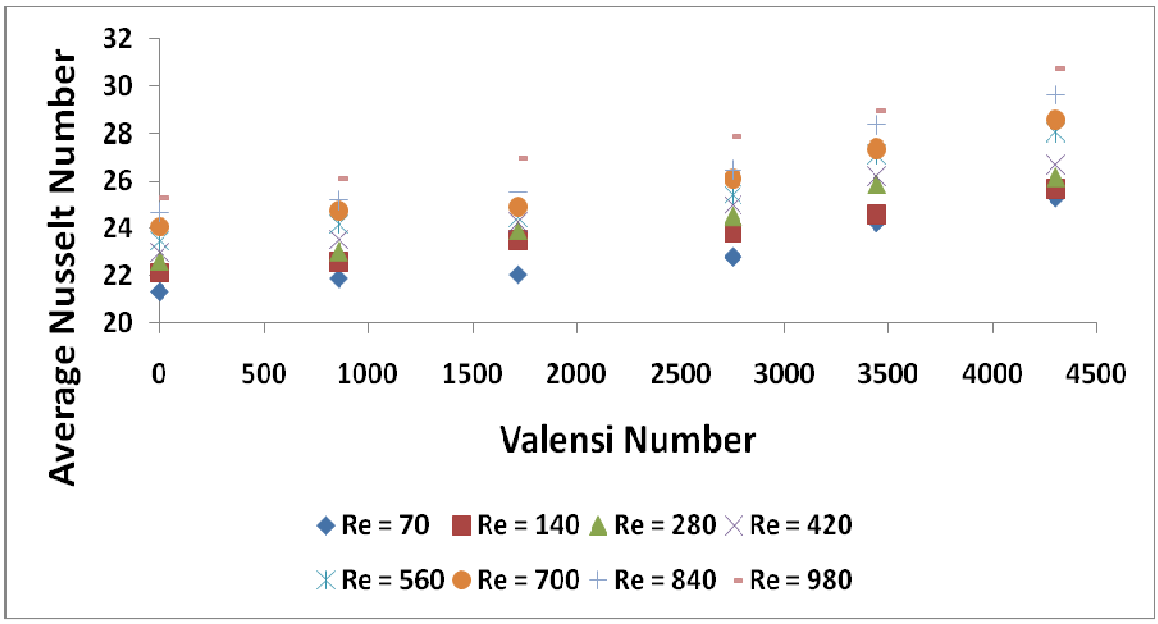

Figure 5.12. 64% Porosity – Nusselt Number vs. Valensi Number.

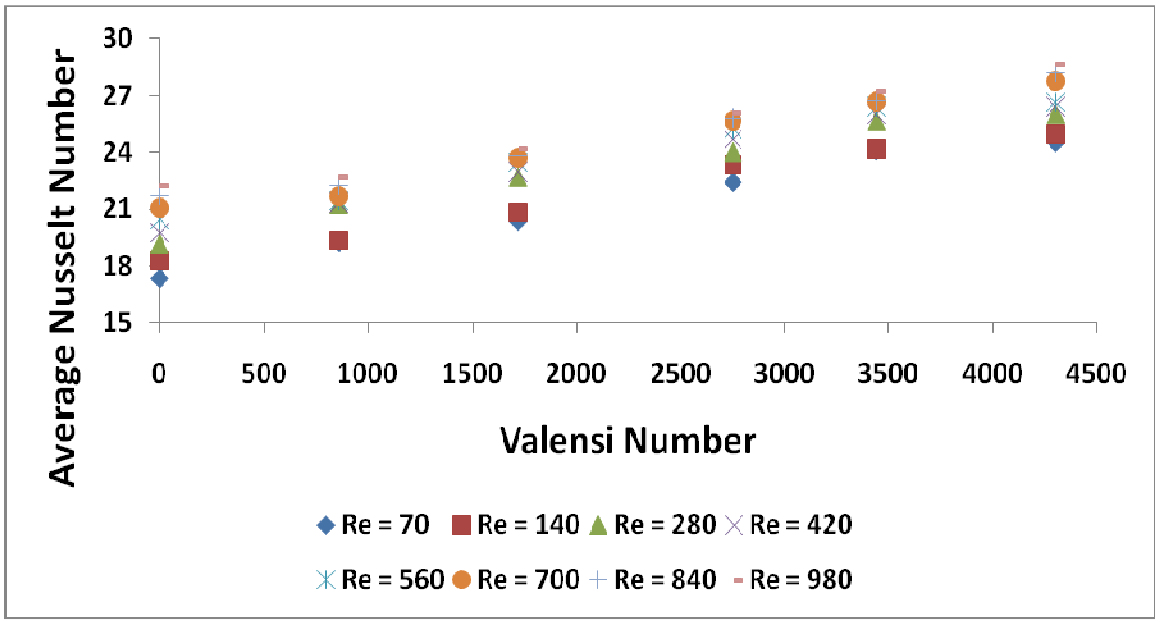

Figure 5.13. 75% Porosity – Nusselt Number vs. Valensi Number.

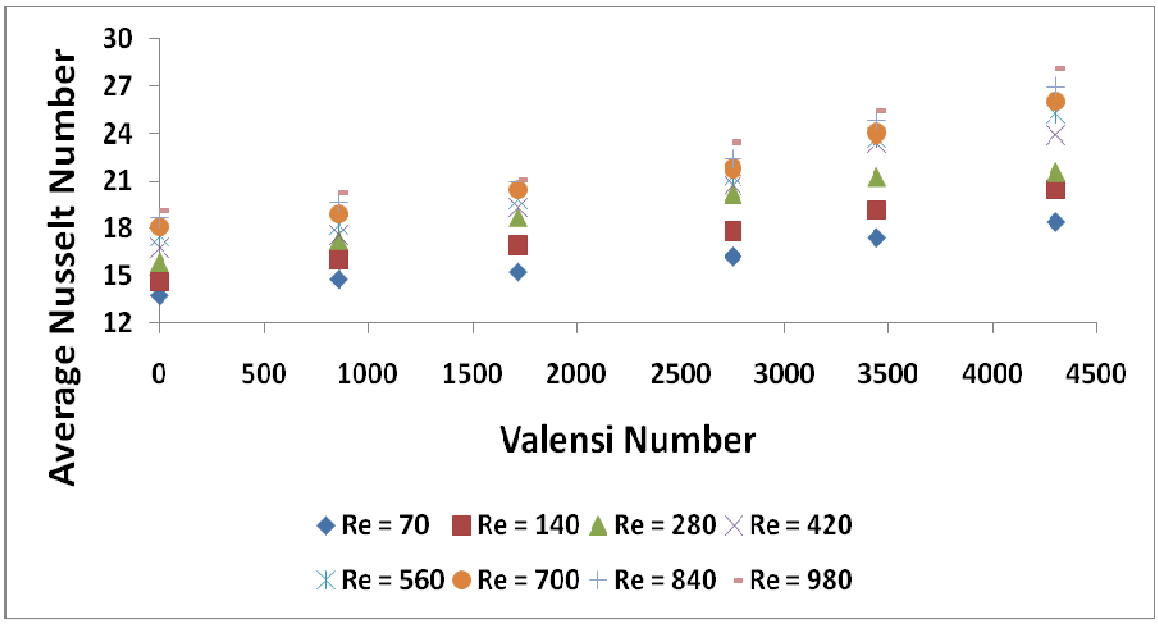

Figure 5.14. 84% Porosity – Nusselt Number vs. Valensi Number.

As noted, the Valensi number is written as,

$$Va_L = \frac{\omega L^2}{\nu} \tag{5.1}$$

where:

ω = angular frequency

The angular frequency is defined by,

$$\omega = 2\pi f \tag{5.2}$$

5.2.3 Nusselt Number Correlation

Using the generated numerical data and analyzing the resulting trends, the following correlation for the unit cell and cycle-average Nusselt number was developed as a function of the Reynolds number, porosity, and the Valensi number,

$$
\begin{aligned}
&Va_L < 2700: Nu_L = 20.85\,\mathrm{Re}_L^{\,0.0873}\left(1-\varepsilon\right)^{0.4014}\left(\exp^{-0.000045Va_L} + 0.0001Va_L\right)\\
&Va_L \geq 2700: Nu_L = 20.999\,\mathrm{Re}_L^{\,0.14}\left(1-\varepsilon\right)^{0.0189}\exp^{-0.00005Va_L} - Q_f\\
&Q_f = 4.07\ln(\mathrm{Re}_L) + (\varepsilon - 2.74)(\varepsilon + 1.47)
\end{aligned}
\tag{5.3}
$$

The associated relative correlation error was determined from,

$$
\%Error = \frac{\left(\left|Nu_{L,computational} - Nu_{L,correlation}\right|\right)}{Nu_{L,computational}} \cdot 100 \tag{5.4}
$$

where:

$Nu_{L,computational}$ = Nusselt number based on computational simulations

$Nu_{L,correlation}$ = Nusselt number based on correlation

Figure 5.15 compares the predictions of the aforementioned correlation with the numerical data. The associated average error was found to be approximately 3%.

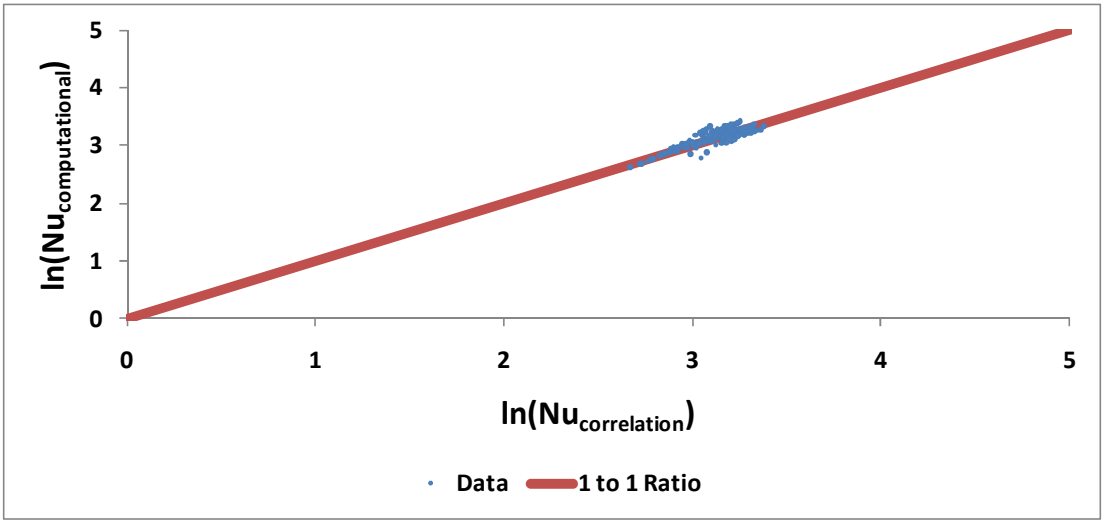

Figure 5.15. Comparison of Nusselt Number Correlation vs. Numerical Predictions.

5.3 Thermal Energy Dispersion

5.3.1 Thermal Dispersion

Using Equations 4.3, 4.7 and 4.12, the instantaneous and cycle-average thermal dispersion term was calculated for the range of Reynolds numbers, porosities, and frequencies shown in Table 5.1. The average thermal dispersion, defined as $\varepsilon\rho_f c_{pf}\left\langle \tilde{u}_j \tilde{T} \right\rangle^f$, at given Reynolds numbers are plotted against frequency for three unit cell porosities. Figures 5.16, 5.17, and 5.18, show these values for unit cell porosities of 64%, 75%, and 84%, respectively.

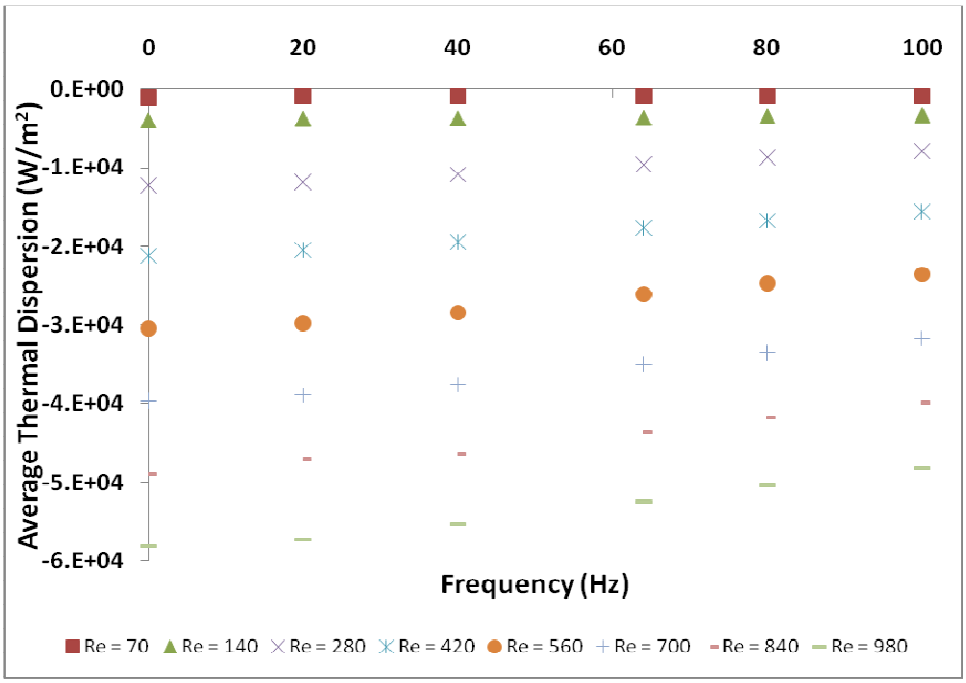

Figure 5.16. 64% Porosity – Thermal Dispersion vs. Frequency.

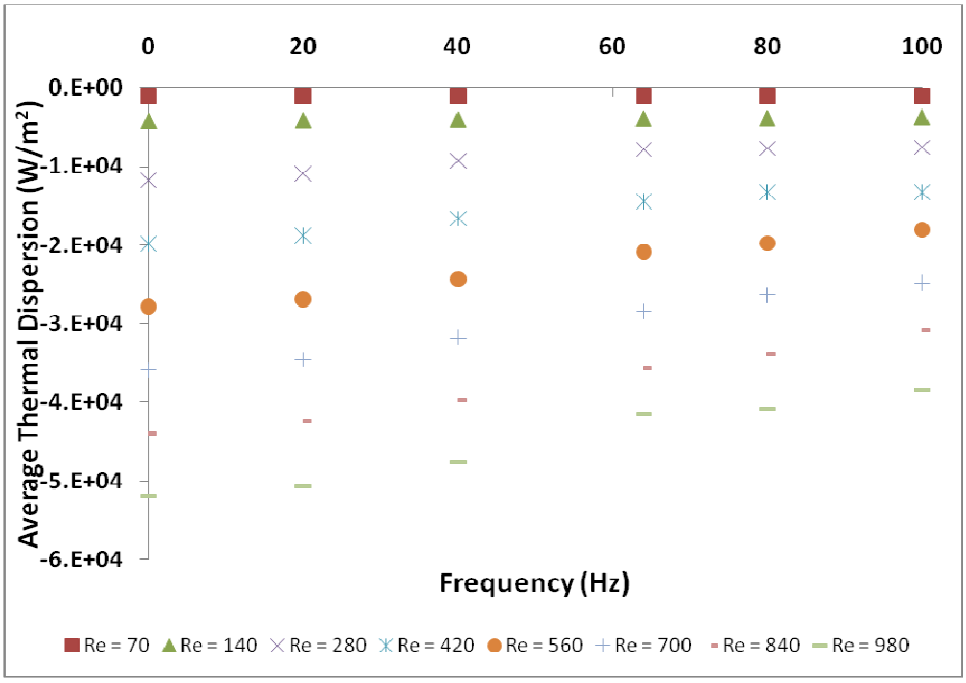

Figure 5.17. 75% Porosity – Thermal Dispersion vs. Frequency.

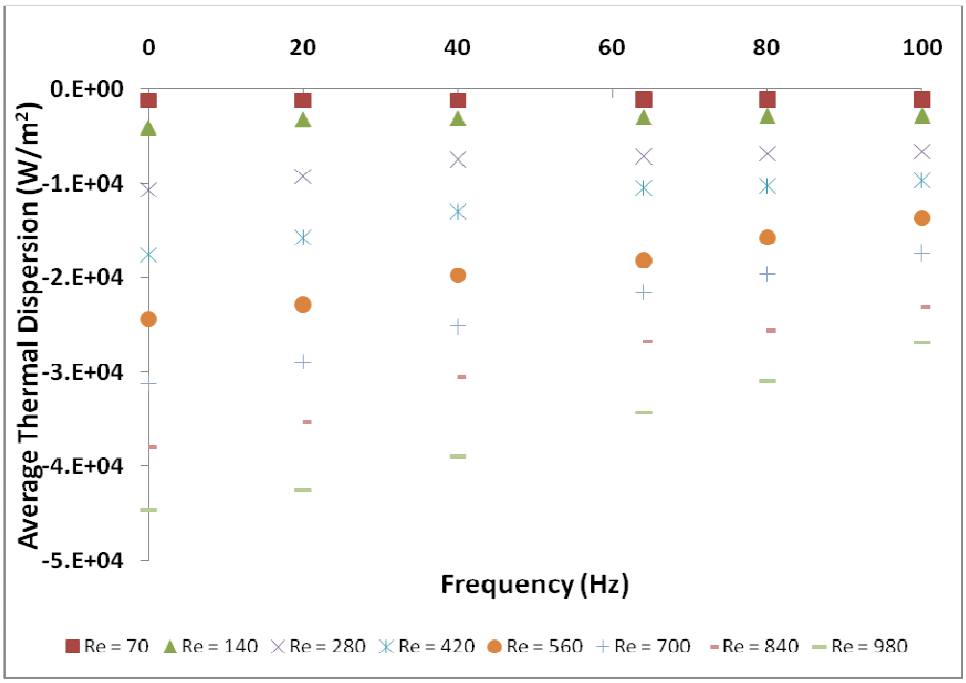

Figure 5.18. 84% Porosity – Thermal Dispersion vs. Frequency.

It is noticed that the magnitude of the average thermal dispersion monotomically decreases as the frequency increases for all unit cell porocities and Reynolds numbers. For each porosity, the higher the Reynolds number, the higher the magnitude of the average thermal dispersion. Finally, within the tested range of porosity, the magnitude of the average thermal dispersion increases as the porosity decreases.

5.3.2 Non-Dimensional Thermal Dispersion

Once the average thermal dispersion was determined, the average non-dimensional thermal dispersion was found by using Equation 4.15. Figures 5.19 through 5.21 summarize the parametric trends. More parametric depictions can be found in Appendix C. Figures 5.19 through 5.21 are similar to Figures 5.22 to 5.24, except that

now the dimensionless Valensi number is used as a coordinate. As noticed consistent trends are noticed for the non-dimensional thermal dispersion compared to the thermal dispersion.

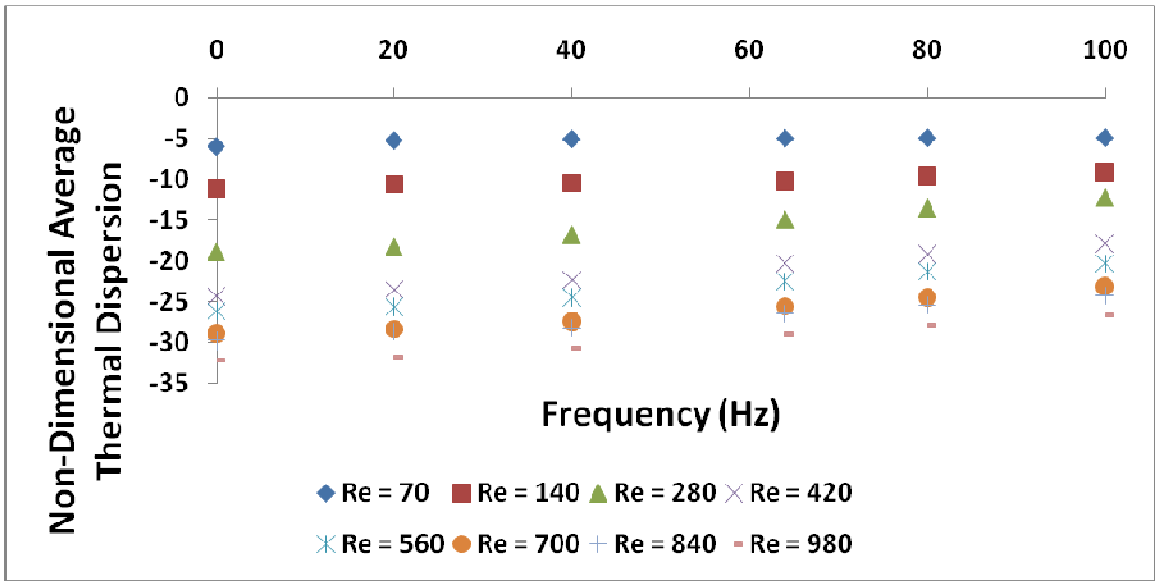

Figure 5.19. 64% Porosity – Non-Dimensional Dispersion vs. Frequency.

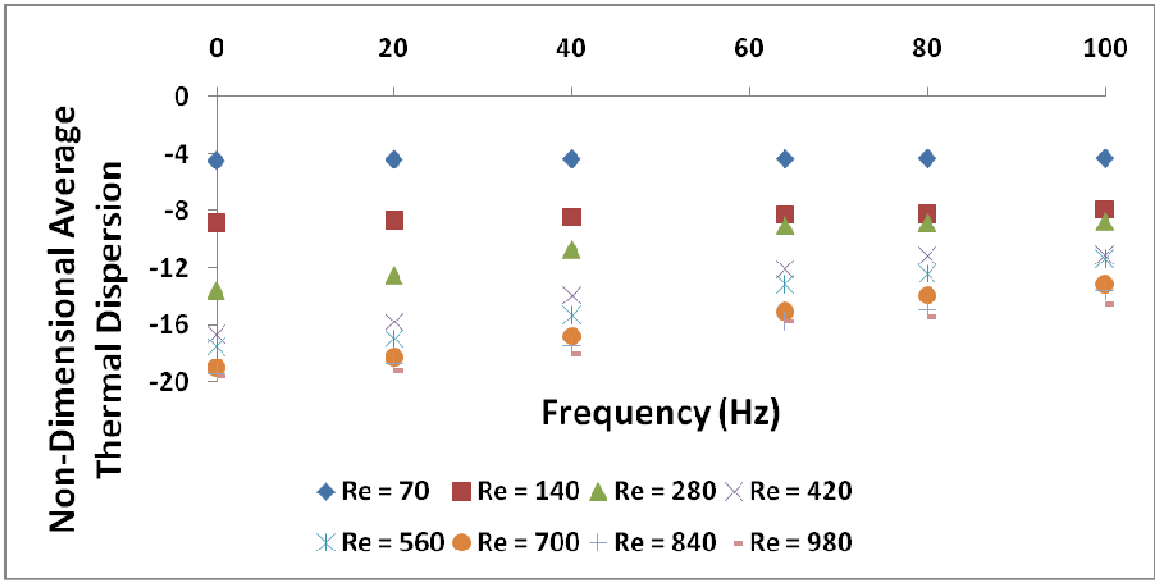

Figure 5.20. 75% Porosity – Non-Dimensional Dispersion vs. Frequency.

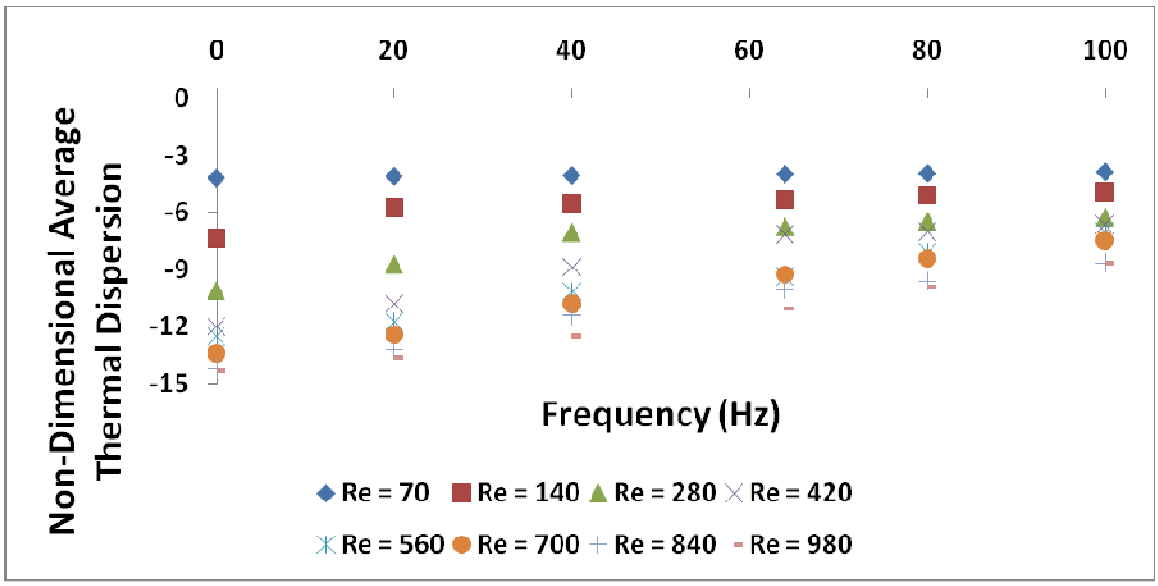

Figure 5.21. 84% Porosity – Non-Dimensional Dispersion vs. Frequency.

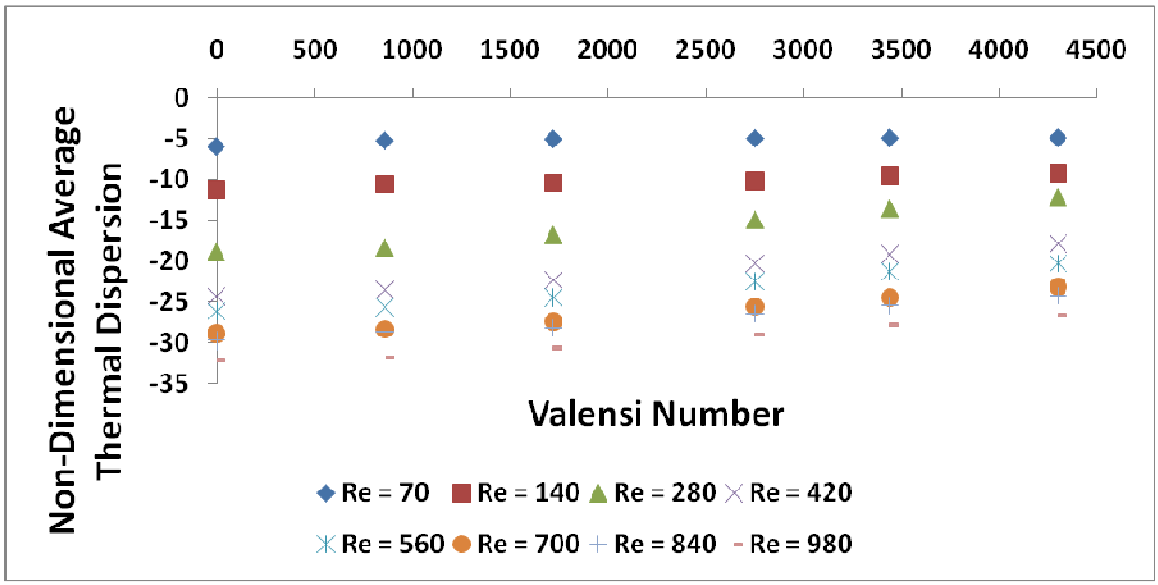

Figure 5.22. 64% Porosity – Non-Dimensional Dispersion vs. Valensi Number.

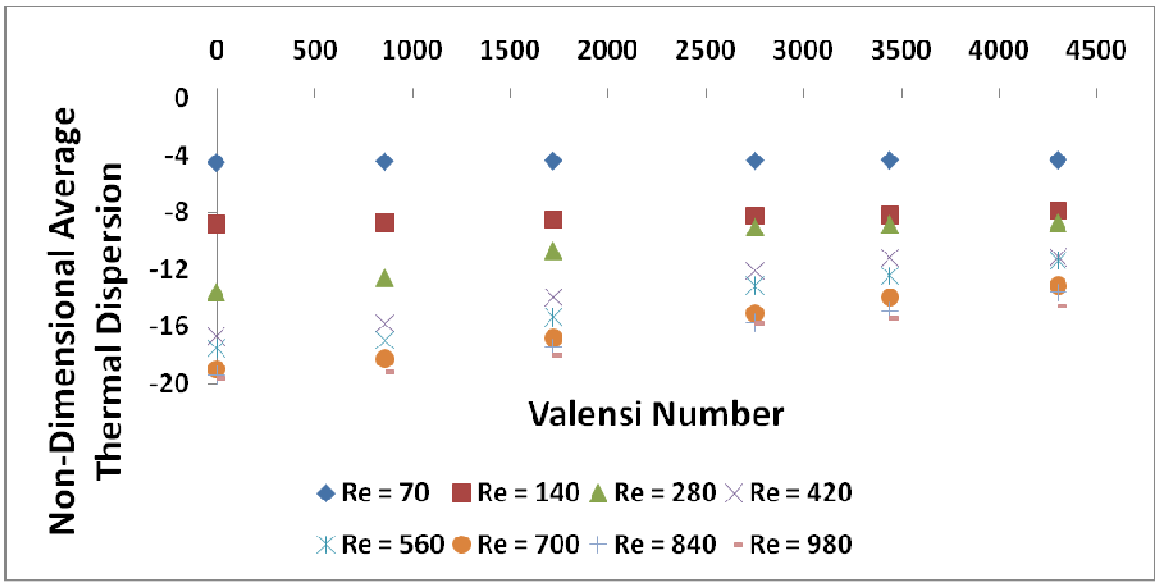

Figure 5.23. 75% Porosity – Non-Dimensional Dispersion vs. Valensi Number.

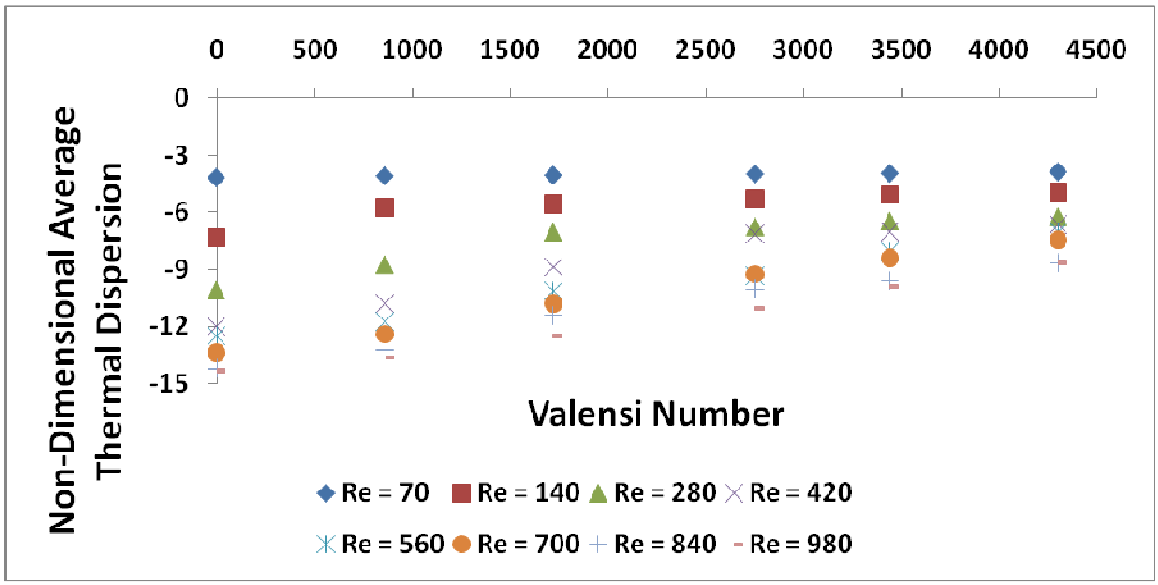

Figure 5.24. 84% Porosity – Non-Dimensional Dispersion vs. Valensi Number.

The magnitude of the non-dimensional average thermal dispersion decreases as the frequency increases for all unit cell porocities and Reynolds numbers. The dimensionless dispersion increases as the Reynolds number increases for all unit cell

porosities and frequencies. Also, the nondimensional thermal dispersoin decreases as the unit cell porosity increases for all Reynolds numbers and frequencies.

5.3.3 Thermal Dispersion Correlation

Using the generated numerical data and analyzing the resulting thermal dispersion trends, the following correlation for the dimensionless average thermal dispersion number was developed as a function of the Reynolds number, porosity, and the Valensi number,

$$D_T^* = (A \cdot \ln(\mathrm{Re}_L) - 37.7)\frac{\left(1 - 0.00000001 Va_L^{\,2} - 0.00008 Va_L\right)}{(1.2558 + 0.0004 \cdot \mathrm{Re}_L)^{((\varepsilon - 0.64)/0.11)}}$$
$$\text{for} \quad Va_L < 2700 : A = 10.35 \tag{5.5}$$
$$\text{for} \quad Va_L \geq 2700 : A = 10.8$$

The associated relative correlation error was determined from,

$$\%Error = \frac{\left(\left|D^*_{T,computational} - D^*_{T,correlation}\right|\right)}{D^*_{T,computational}} \cdot 100 \tag{5.6}$$

where:

$D^*_{T,computational}$ = Dimensionless dispersion number based on computational simulations

$D^*_{T,correlation}$ = Dimensionless dispersion number based on correlation

Figure 5.25 compares the predictions of the aforementioned correlation with the numerical data. The associated average error was found to be approximately 4%.

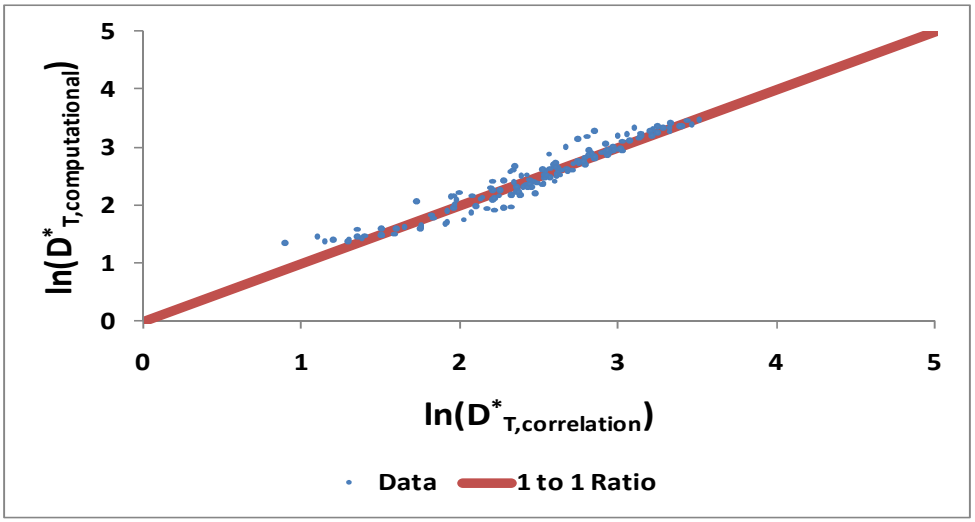

Figure 5.25. Comparison of D_T^* Correlation vs. Numerical Predictions.

5.4 Effective Thermal Conductivity

The instantaneous thermal dispersion thermal conductivity was found by using Equation 4.17. This dispersion conductivity was then non-dimensionalized by dividing by the thermal conductivity of the working fluid. It is important to note that the thermal dispersion term, and consequently the thermal dispersion conductivity, can only be defined based on volume-averaging. It is however possible to calculate the instantaneous values of k_{disp}. The denominator on the right side of the latter equation was calculated for unit cell 5, while the instantaneous temperature gradient was calculated from,

$$\left\langle \frac{dT}{dx} \right\rangle = \frac{\left(\left\langle T_f \right\rangle_6 - \left\langle T_f \right\rangle_4 \right)}{2L} \tag{5.7}$$

The dependence of the instantaneous dimensionless dispersion thermal conductivity, k_{disp}/k_f , during the span of a few periodic steady-state cycles for a typical set of parameters was studied. Examples of the results are displayed in Figures 5.26 to 5.29.

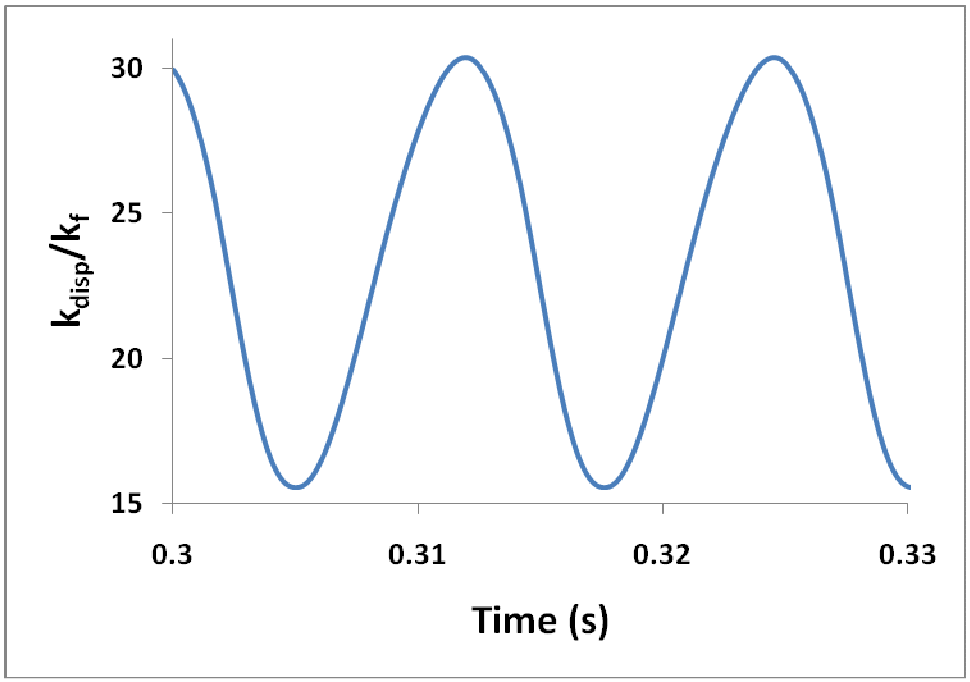

Figure 5.26. Instantaneous Dispersion Conductivity at 75% Porosity and Re_L = 420.

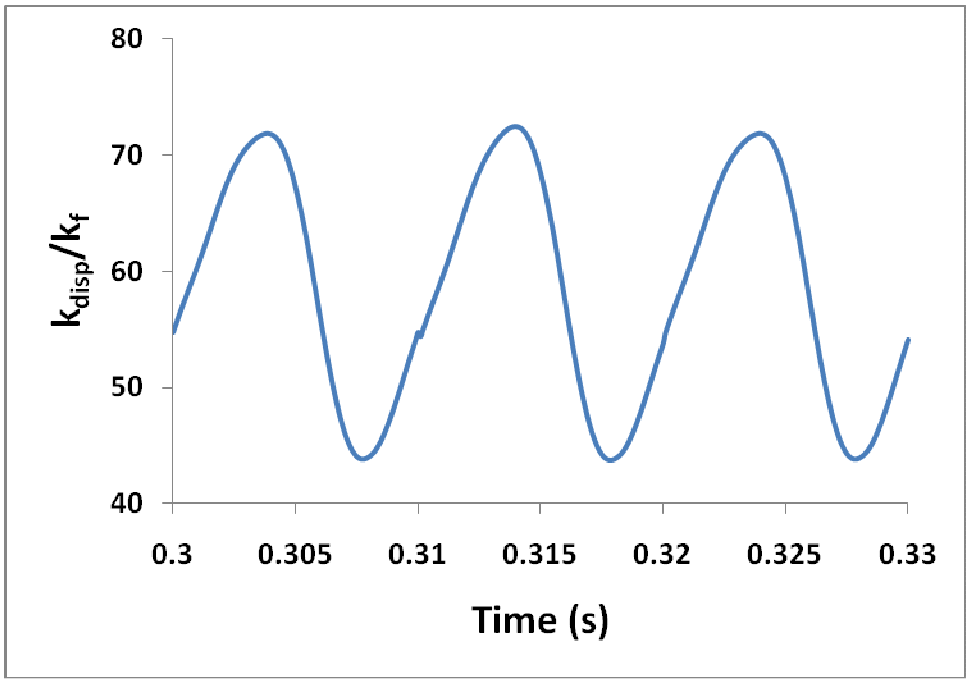

Figure 5.27. Instantaneous Dispersion Conductivity at 64% Porosity and Re_L = 560.

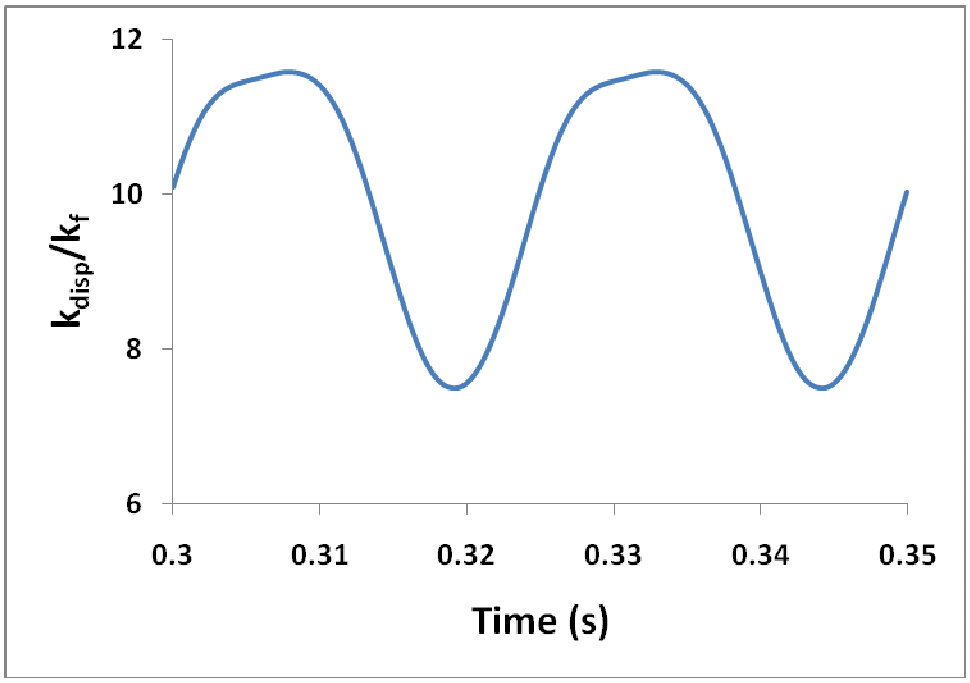

Figure 5.28. Instantaneous Dispersion Conductivity at 84% Porosity and Re_L = 280.

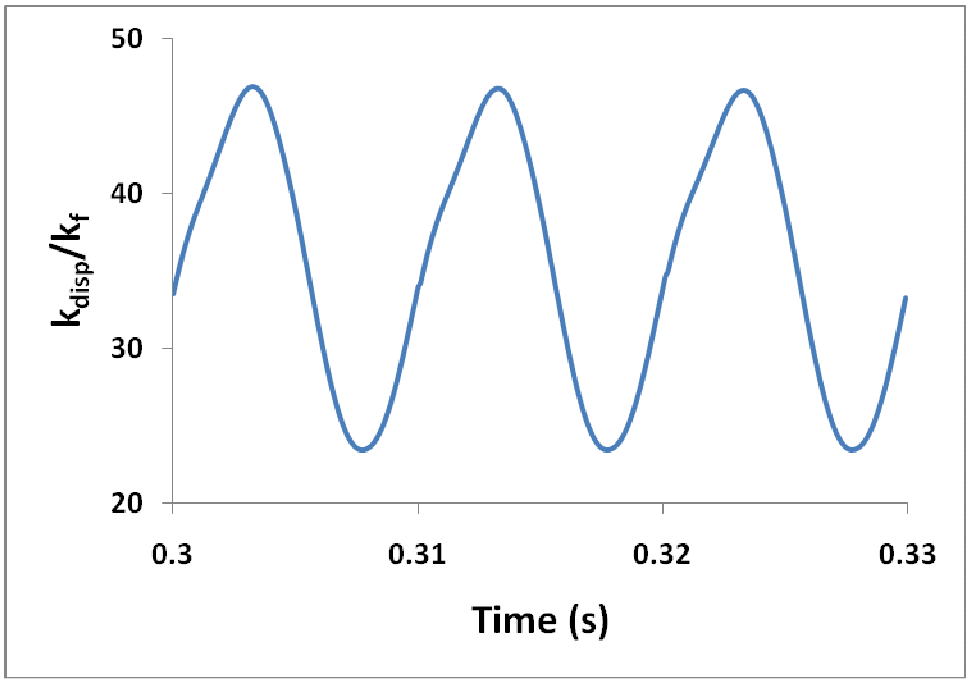

Figure 5.29. Instantaneous Dispersion Conductivity at 84% Porosity and Re_L = 840.

The dispersion conductivity displayed above represents the axial direction of the simulated porous structure. The figures above show that the dispersion thermal conductivity varies periodically during each cycle. Also, it is noticed that during each cycle, over a portion of the cycle, the dispersion thermal conductivity can actually be larger than the molecular thermal conductivity of the working fluid by orders of magnitude.

The dimensionless thermal dispersion conductivity for steady flow at ε=84% and Re_L = 420 is displayed in Figure 5.30.

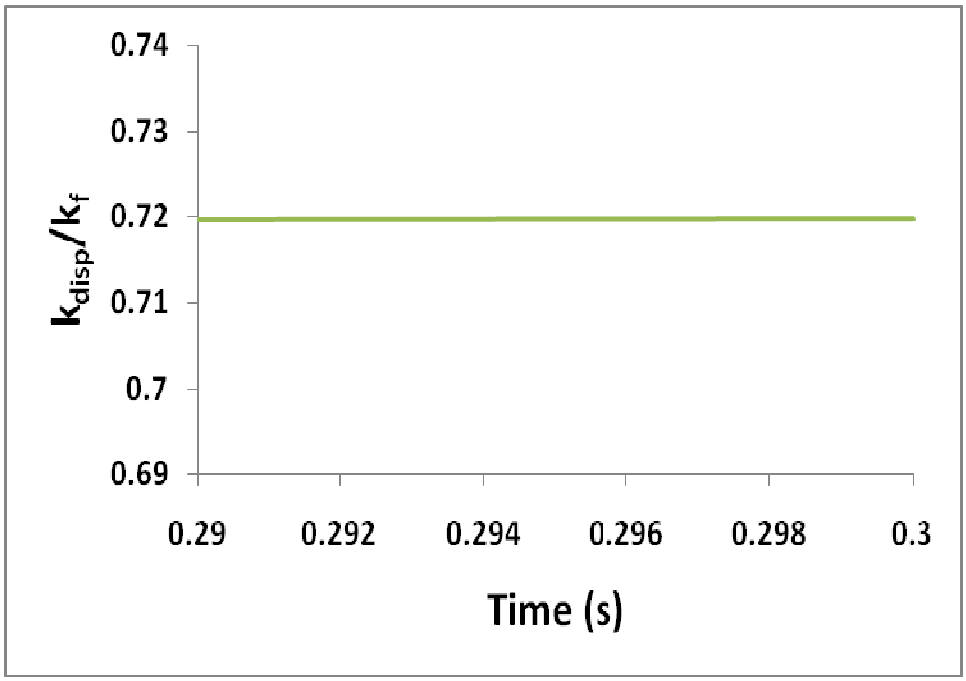

Figure 5.30. Steady Flow Dimensionless Dispersion Thermal Conductivity.

The large magnitude of the thermal dispersion conductivity confirms the significance of thermal dispersion as a strong contributor to heat transfer in laminar flow in porous media. The concept of thermal dispersion conductivity implies that the magnitude of the thermal dispersion is proportional to the gradient of the volume-averaged fluid temperature. Theoretically, however, this proportionality is justifiable for steady-state or slow transients [8]. For transients that are too fast to justify quasi-equilibrium idealization, as a result, the aforementioned proportionality will be inadequate. Thus, the effective thermal dispersion conductivity may not be a useful tool for pulsating and periodic flows of interest for this investigation.

CHAPTER 6

CONCLUSION AND RECOMMENDATIONS

6.1 Concluding Remarks

The adverse effects of solid-fluid thermal non-equilibrium and frictional losses within the regenerator component of a regenerative cryocooler system, which is arguably the most important part of the entire cryocooler system, determines the overall performance of the cryocooler. Common regenerators in pulse tube and Stirling cryocoolers are made of porous structures, often fine mesh screens of rare earth materials, an idealized porous medium. The regenerator in these cryocooler systems is subject to periodic flow of a gaseous cryogen, helium in most cases. Although, steady flow in porous media has been investigated extensively in the past, current understanding of the basic flow and heat transfer phenomena in pulsating and periodic flows in porous media is far from adequate. In this study, the pore-level energy phenomena within an idealized porous medium were investigated. The solid-fluid heat transfer coefficients and thermal dispersion effects were numerically studied for a generic two-dimensional porous medium undergoing pulsating flow conditions. The numerical investigation was carried out using Fluent CFD code. The generic porous media were formed by arrays of parallel square cylinders.

The theoretical investigation revealed that the average Nusselt number increased and the magnitude of the dimensionless average thermal dispersion decreased with increasing frequency for a given unit cell length-based Reynolds number at a particular

porosity. Similar trends were found for the average heat transfer coefficient and the average thermal dispersion term, respectively. The results also showed that the flux of heat transport caused by thermal dispersion were typically orders of magnitude larger than the molecular conduction in the fluid. Also, the instantaneous thermal dispersion conductivity was found to vary periodically during each cycle, confirming that an instantaneous effective thermal conductivity is inappropriate for porous medium subject to pulsating flow. Finally, correlations for the empirical unit cell and cycle-average Nusselt number and the dimensionless cycle-average thermal dispersion were created.

6.2 Recommendations for Future Work

- The future of cryocooling systems are heading toward micro-scale coolers, which require finer meshes in the regenerator and higher frequncies. Therefore, the study of smaller pore size diameters, on the order of 10 micrometers are recommended.
- The current theorectical and computational investigation served as a great first step for the solid-fluid interactions occuring in porous media during pulsating flow, however experimental studies are necessary for further validation. Although, these experiemental studies would be difficult to perform for the pore scale, they are needed.
- More detailed investigations for the energy and dispersion effects at high frequenices, greater than 100 Hz, would be interesting and useful for cryocooling systems with higher compressor power input.

- Changing the porous sturucture geometry from arrays of square cylinders to circular or other geometries representative of emerging mesh screen technologies would allow furthur understanding of the energy interactions occurring within different porous structure geometries.
- Finally, tackling the more difficult problem of periodic flow, specifically, oscillatory flow conditions, in the porous geometries would be a more realistic cryocooler regenration flow situtation. This of course, would also require not only computational and theorectical investigation but experiemental validation as well.

APPENDIX A

FLUENT USER DEFINED FUNCTION

```
// Pulsating velocity profile at inlet boundary
DEFINE_PROFILE(velocity_right, thread, position)
{
  face_t f1;
  real t = CURRENT_TIME;

  real U = 0.818;
  real a = 0.4;
  real w = 2. * 3.141592 * 40.;

  begin_f_loop(f1, thread)
    {
      F_PROFILE(f1,thread,position) = U*(1.+a*sin(w*t));
    }
  end_f_loop(f1, thread)
}
```

Figure A.1. Inlet Velocity Condition.

APPENDIX B

NUSSELT NUMBER PLOTS

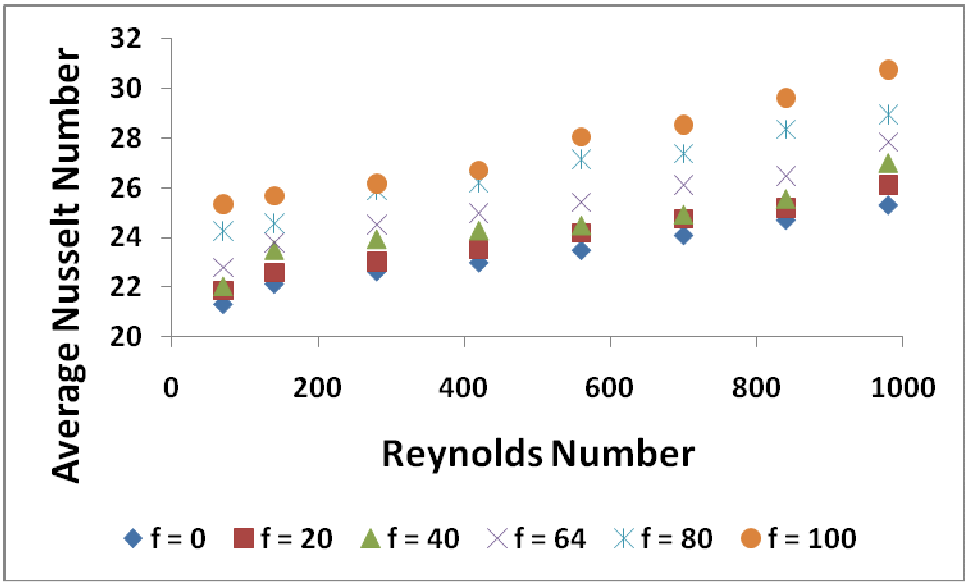

Figure B.1. 64% Porosity – Nusselt Number vs. Reynolds Number.

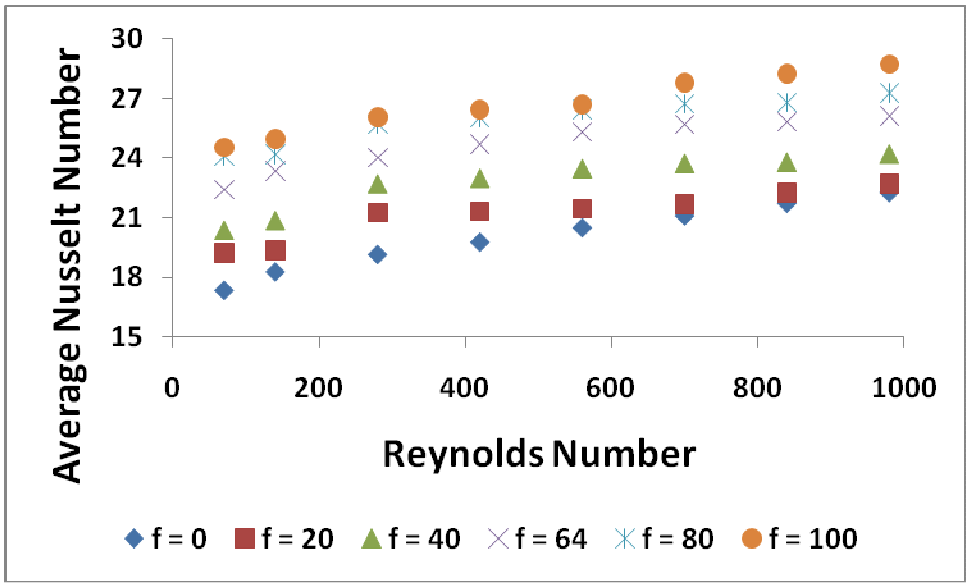

Figure B.2. 75% Porosity – Nusselt Number vs. Reynolds Number.

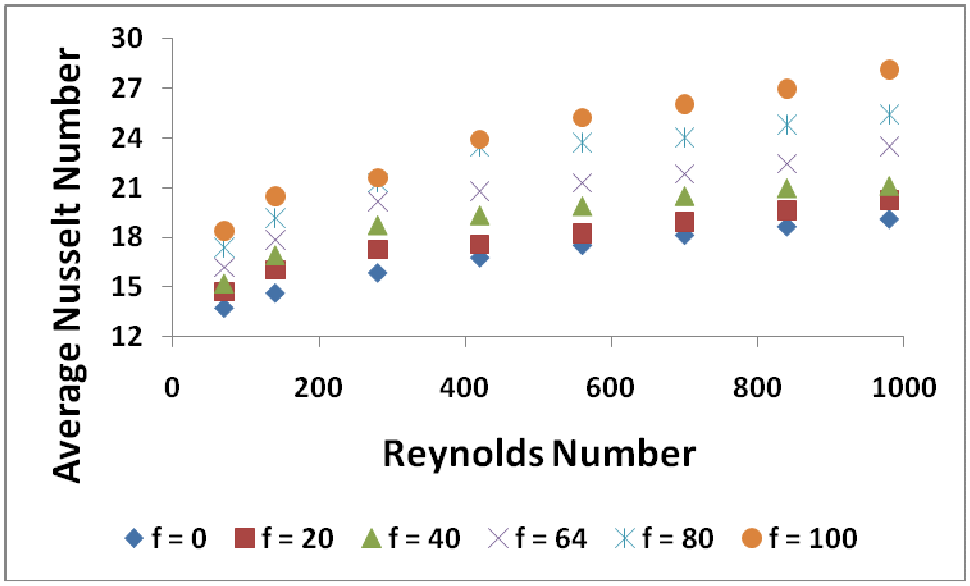

Figure B.3. 84% Porosity – Nusselt Number vs. Reynolds Number.

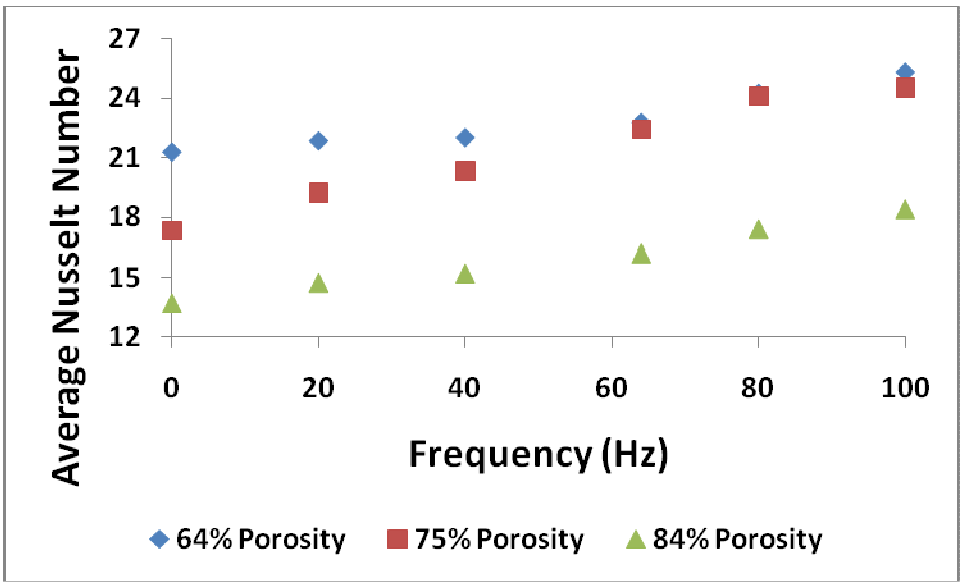

Figure B.4. Reynolds Number = 70 – Nusselt Number vs. Frequncey..

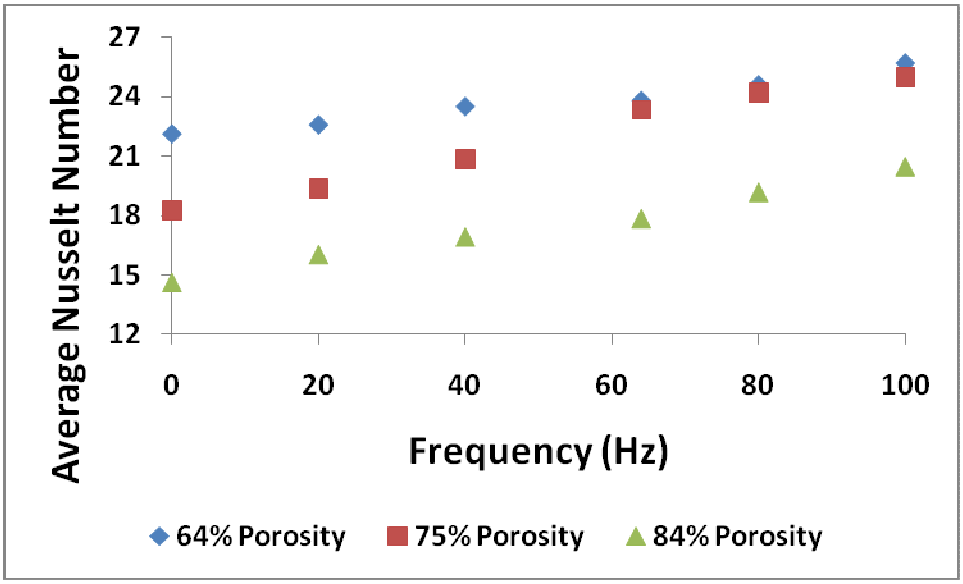

Figure B.5. Reynolds Number = 140 – Nusselt Number vs. Frequency.

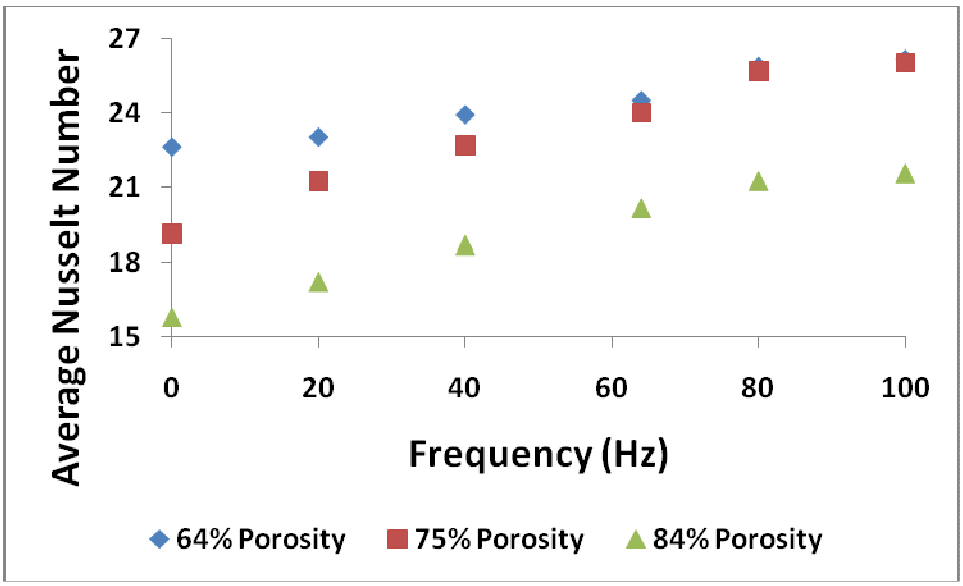

Figure B.6. Reynolds Number = 280 – Nusselt Number vs. Frequency.

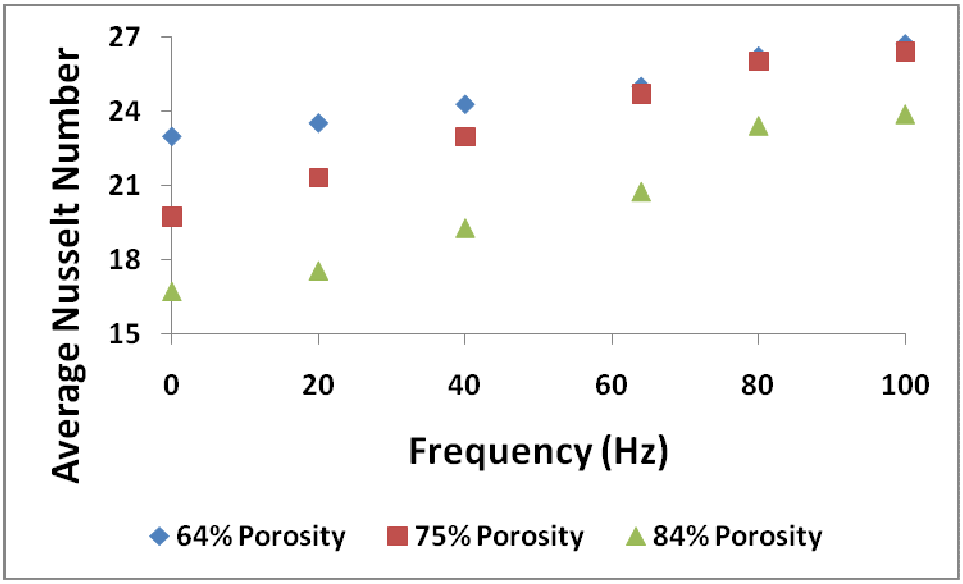

Figure B.7. Reynolds Number = 420 – Nusselt Number vs. Frequency.

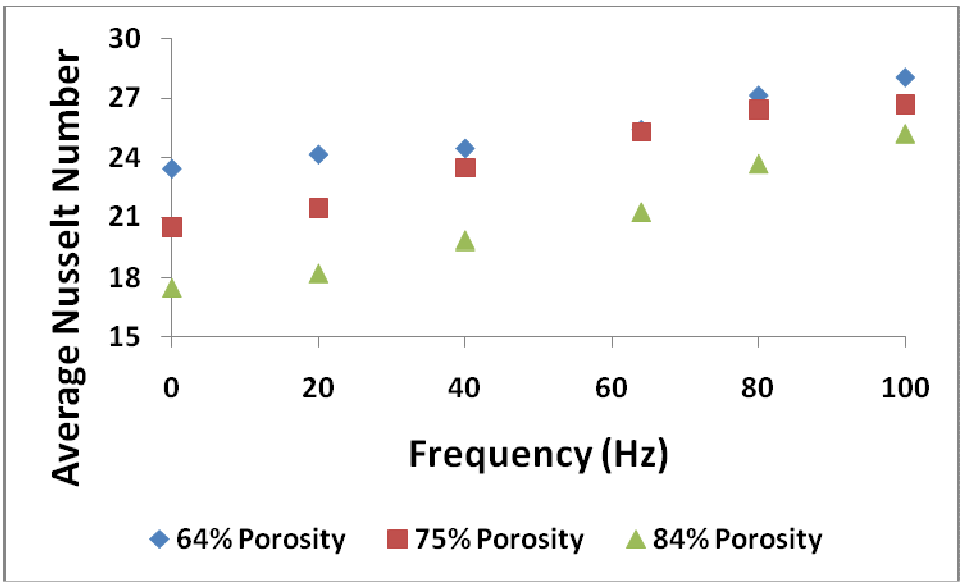

Figure B.8. Reynolds Number = 560 – Nusselt Number vs. Frequency.

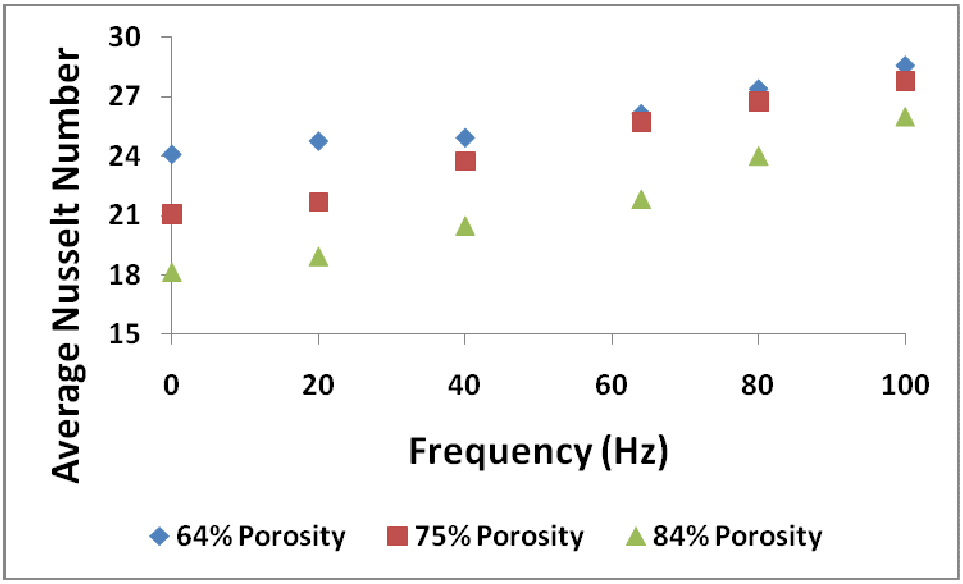

Figure B.9. Reynolds Number = 700 – Nusselt Number vs. Frequency.

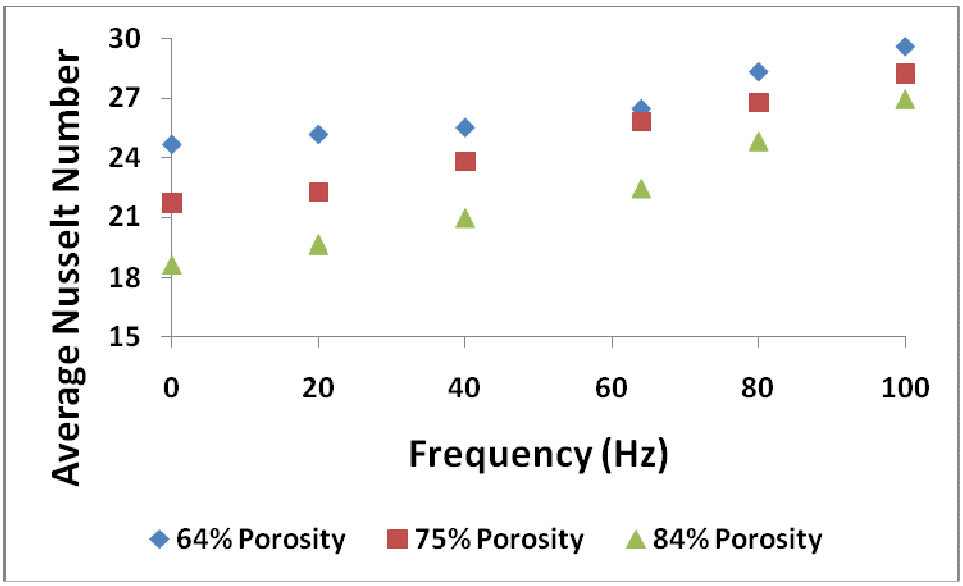

Figure B.10. Reynolds Number = 840 – Nusselt Number vs. Frequency.

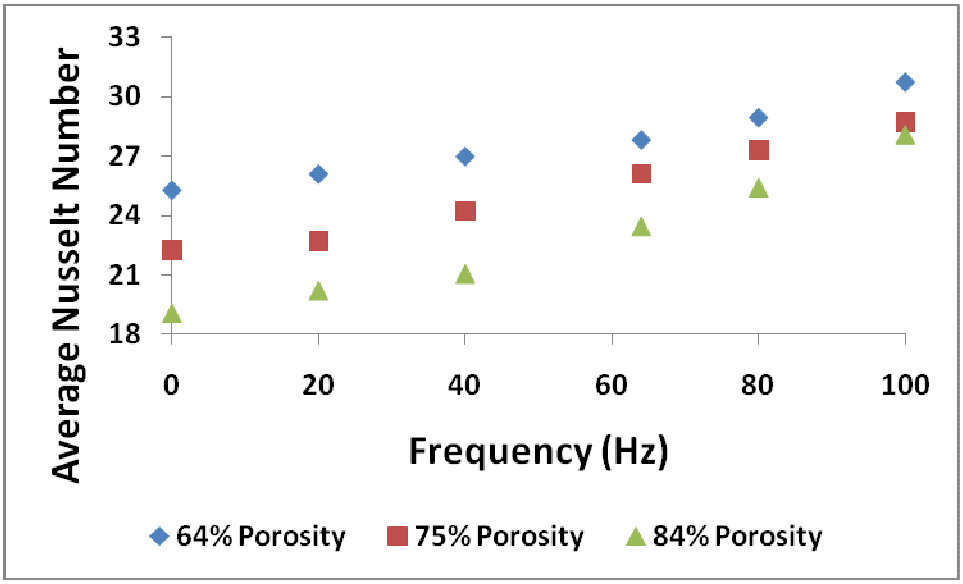

Figure B.11. Reynolds Number = 980 – Nusselt Number vs. Frequency.

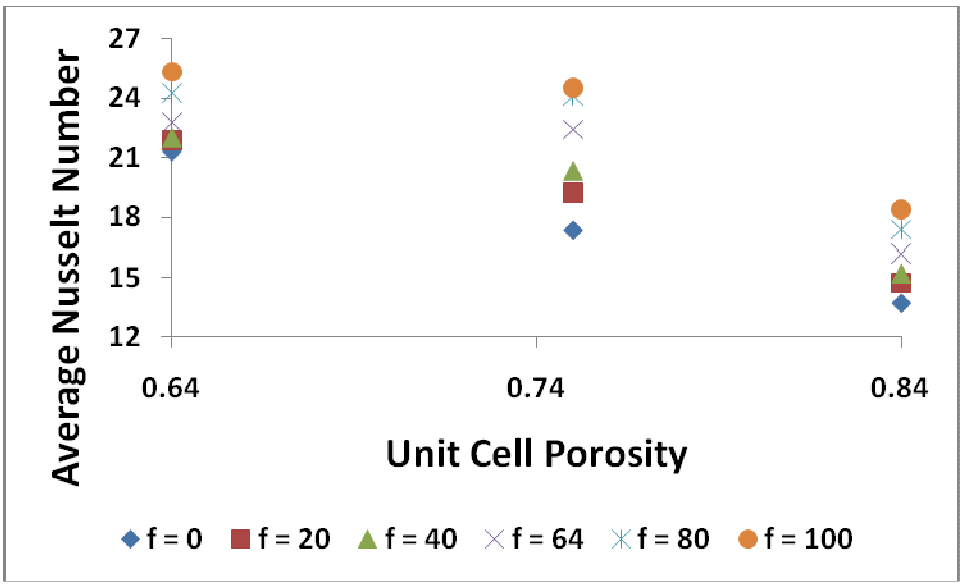

Figure B.12. Reynolds Number = 70 – Nusselt Number vs. Unit Cell Porosity.

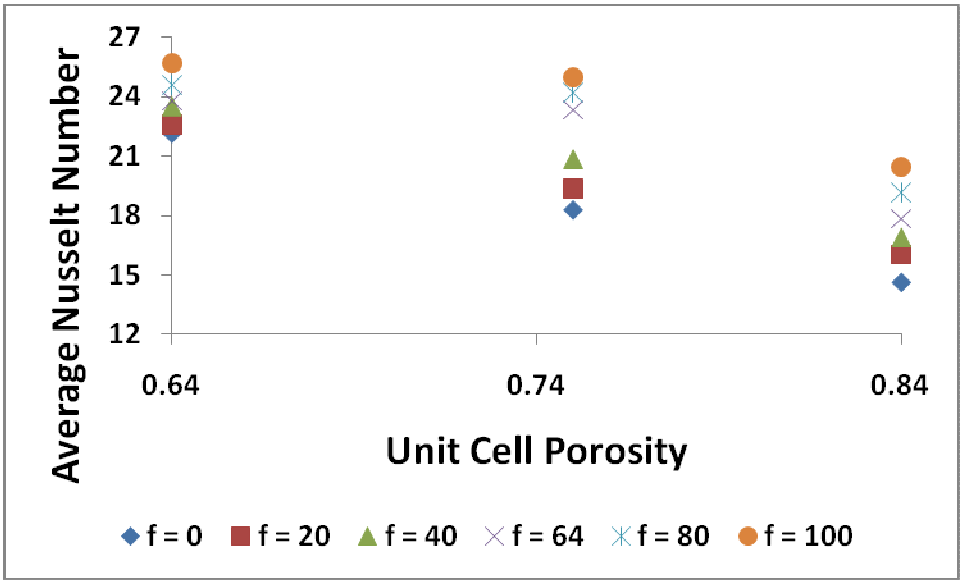

Figure B.13. Reynolds Number = 140 – Nusselt Number vs. Unit Cell Porosity.

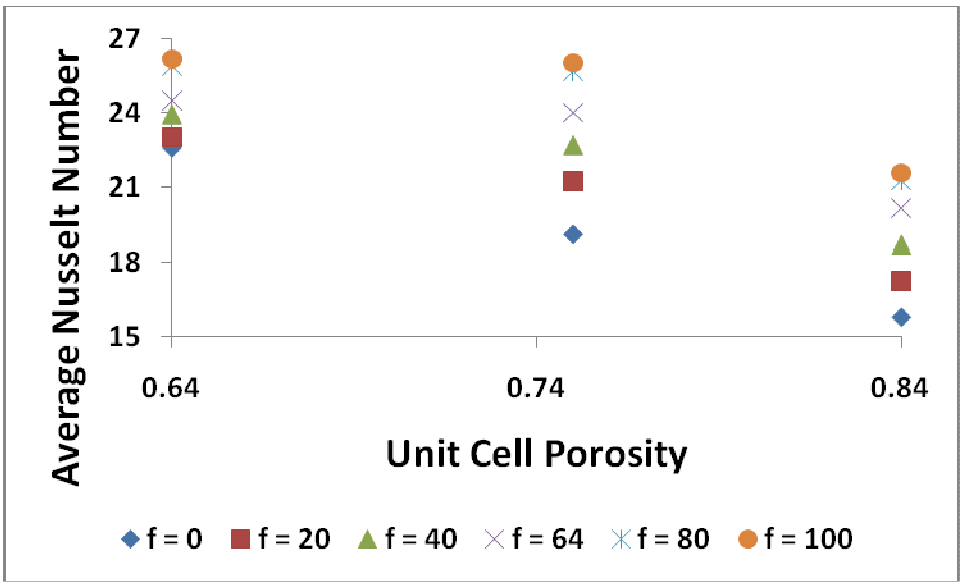

Figure B.14. Reynolds Number = 280 – Nusselt Number vs. Unit Cell Porosity.

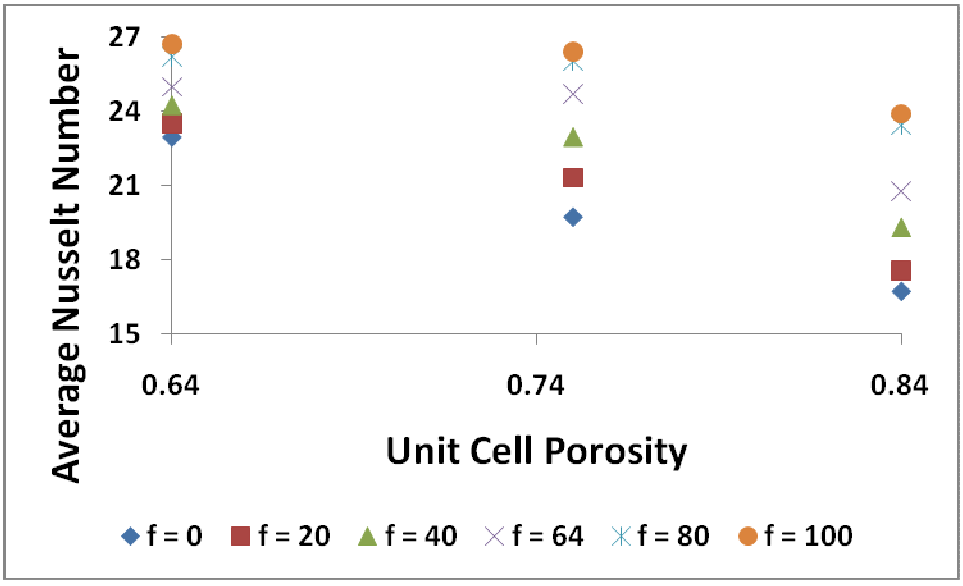

Figure B.15. Reynolds Number = 420 – Nusselt Number vs. Unit Cell Porosity.

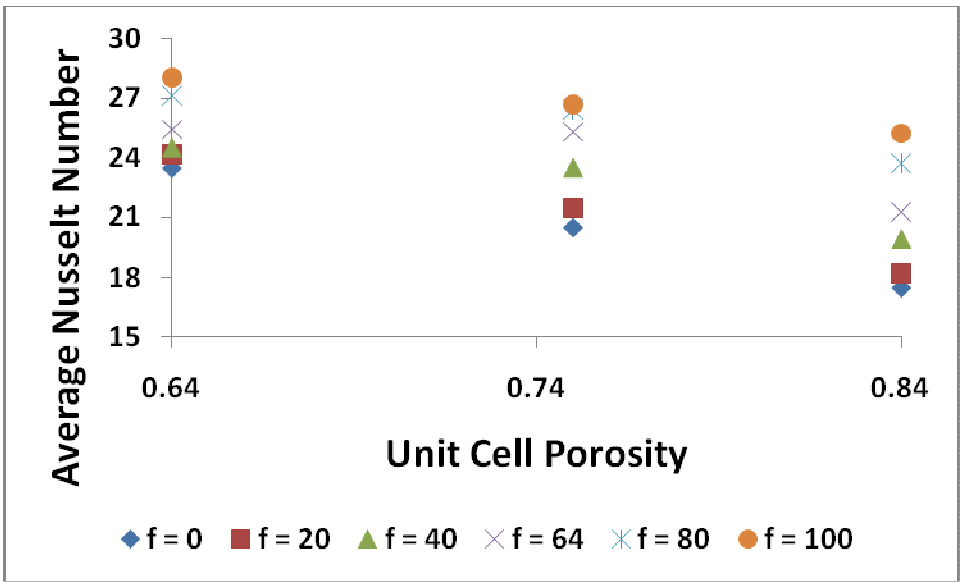

Figure B.16. Reynolds Number = 560 – Nusselt Number vs. Unit Cell Porosity.

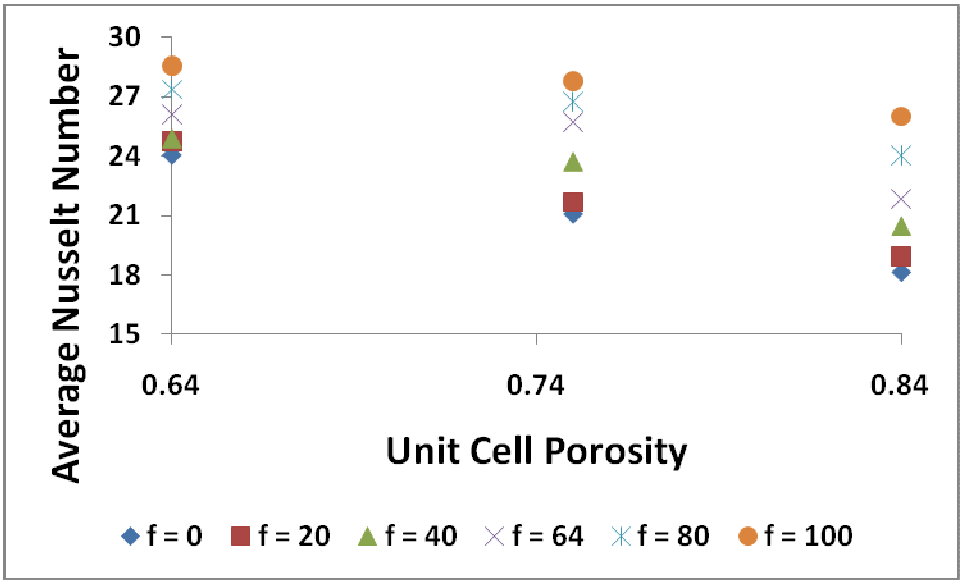

Figure B.17. Reynolds Number = 700 – Nusselt Number vs. Unit Cell Porosity.

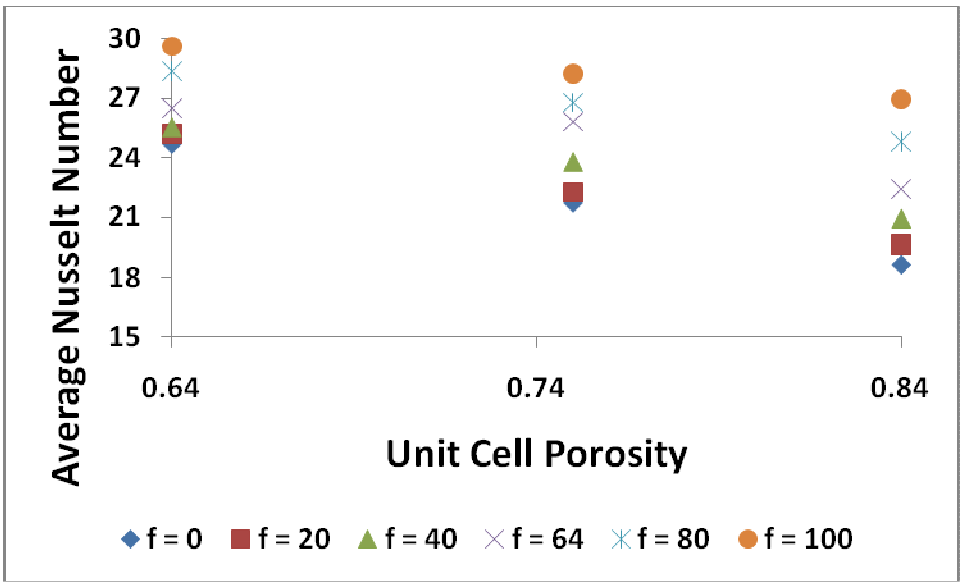

Figure B.18. Reynolds Number = 840 – Nusselt Number vs. Unit Cell Porosity.

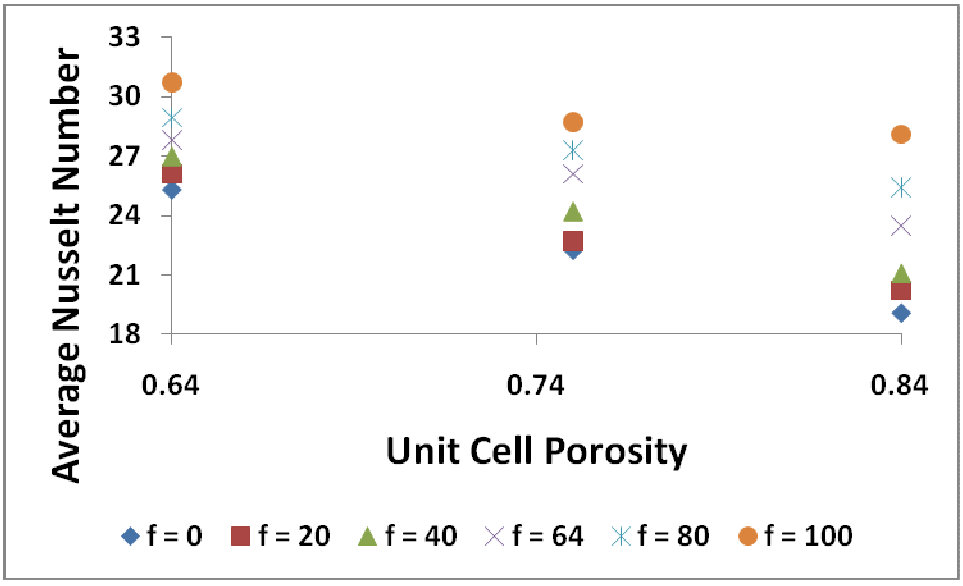

Figure B.19. Reynolds Number = 980 – Nusselt Number vs. Unit Cell Porosity.

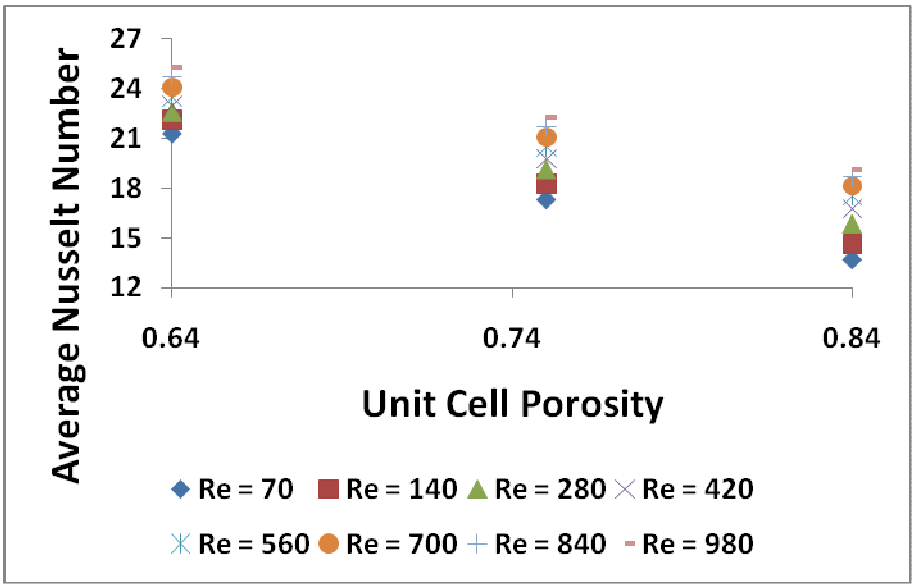

Figure B.20. Frequency = 0 Hz – Nusselt Number vs. Unit Cell Porosity.

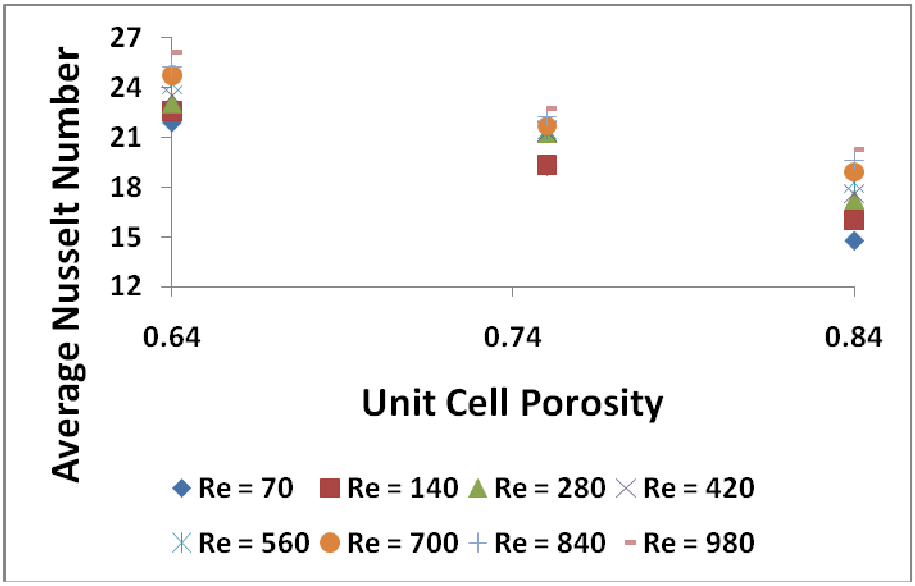

Figure B.21. Frequency = 20 Hz – Nusselt Number vs. Unit Cell Porosity.

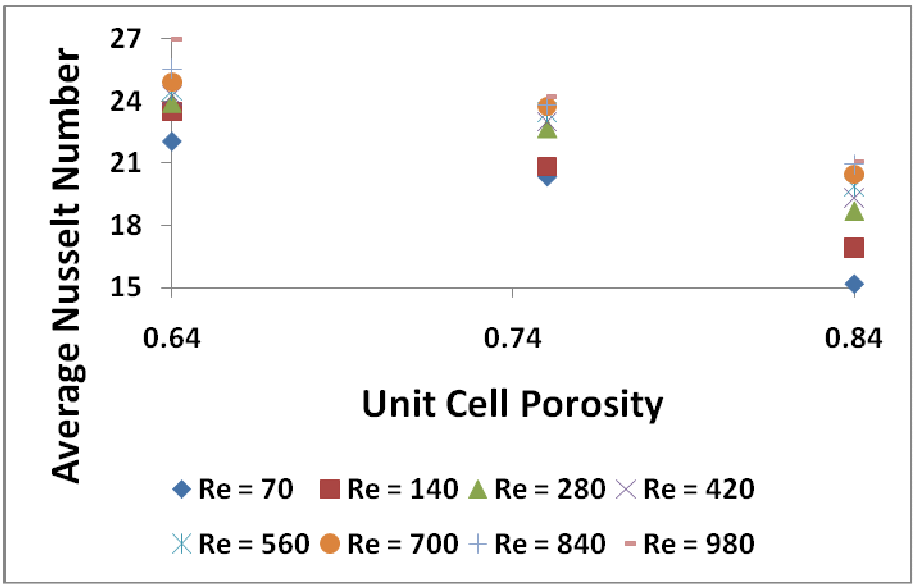

Figure B.22. Frequency = 40 Hz – Nusselt Number vs. Unit Cell Porosity.

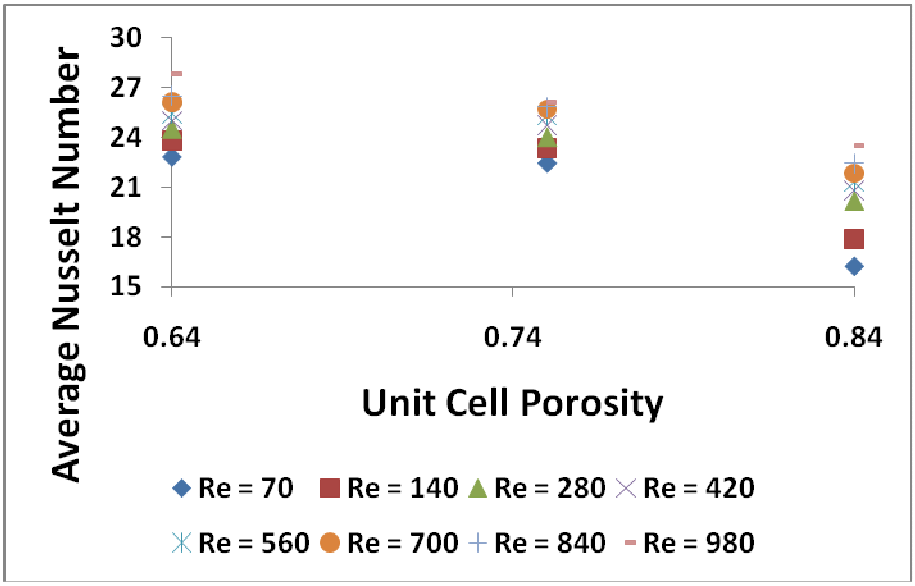

Figure B.23. Frequency = 64 Hz – Nusselt Number vs. Unit Cell Porosity.

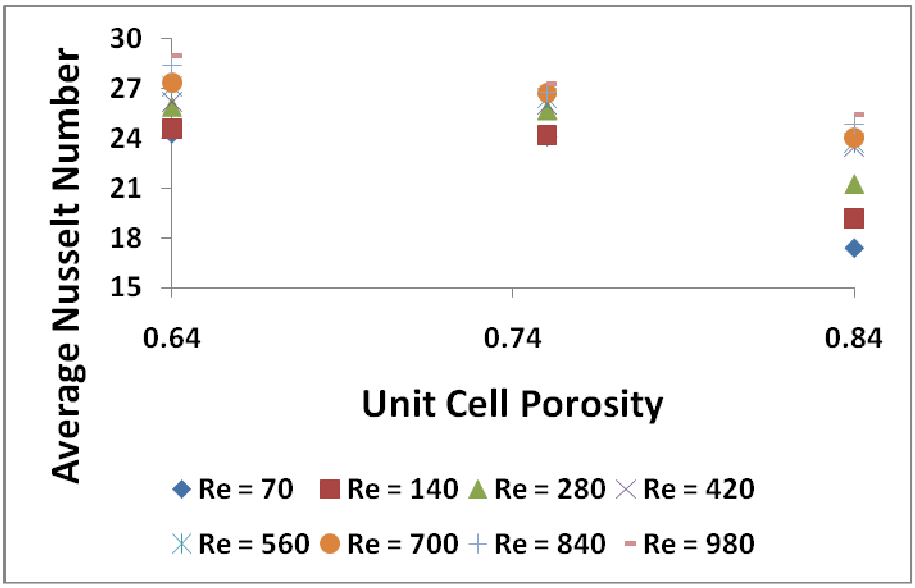

Figure B.24. Frequency = 80 Hz – Nusselt Number vs. Unit Cell Porosity.

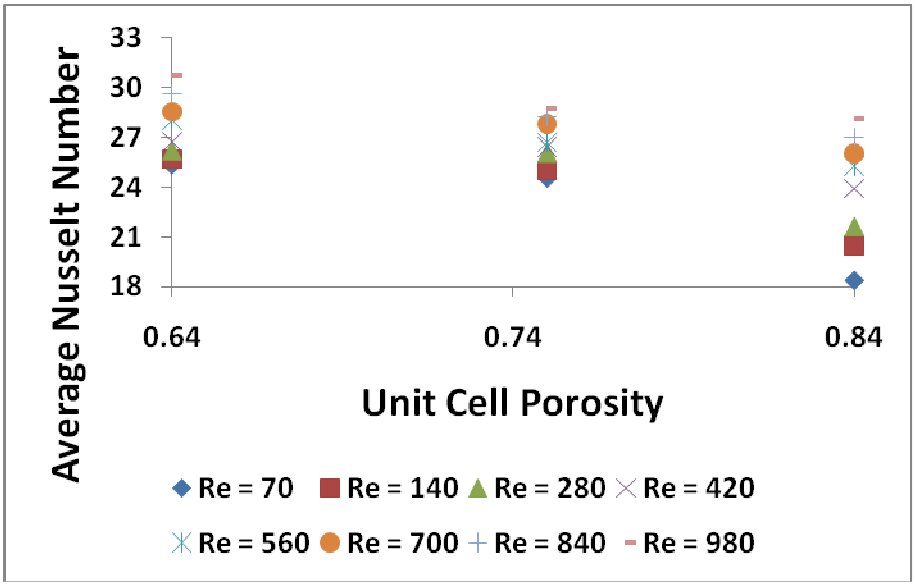

Figure B.25. Frequency = 100 Hz – Nusselt Number vs. Unit Cell Porosity.

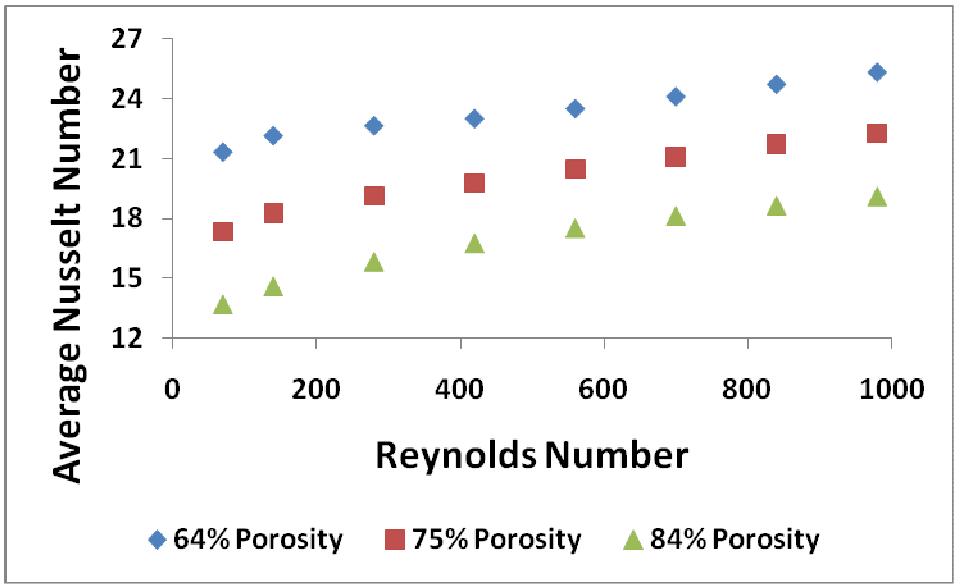

Figure B.26. Frequency = 0 Hz – Nusselt Number vs. Reynolds Number.

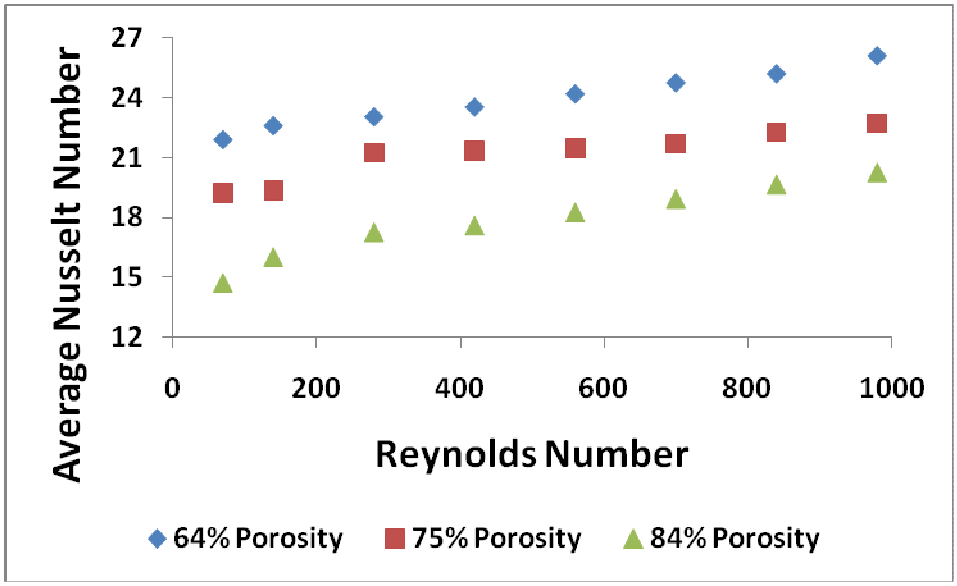

Figure B.27. Frequency = 20 Hz – Nusselt Number vs. Reynolds Number.

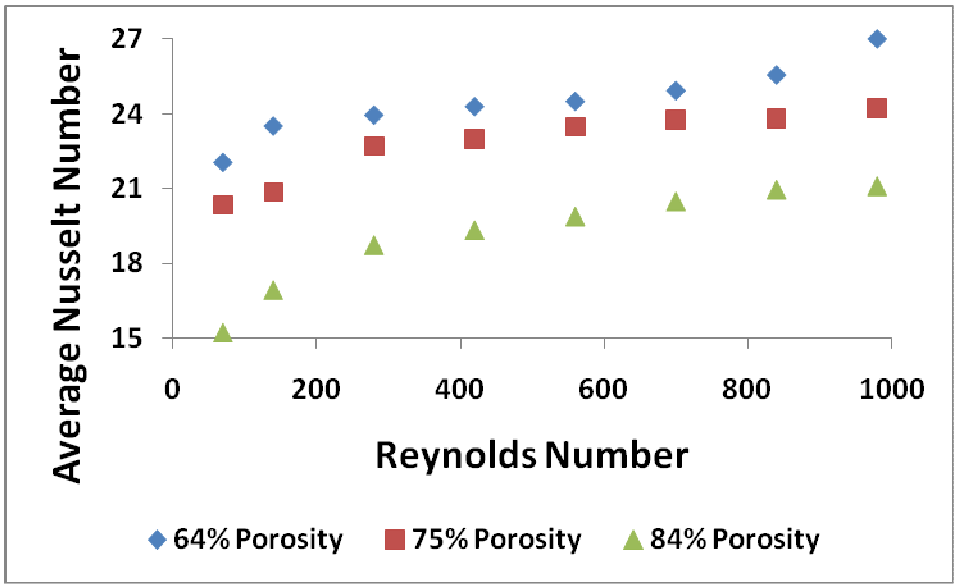

Figure B.28. Frequency = 40 Hz – Nusselt Number vs. Reynolds Number.

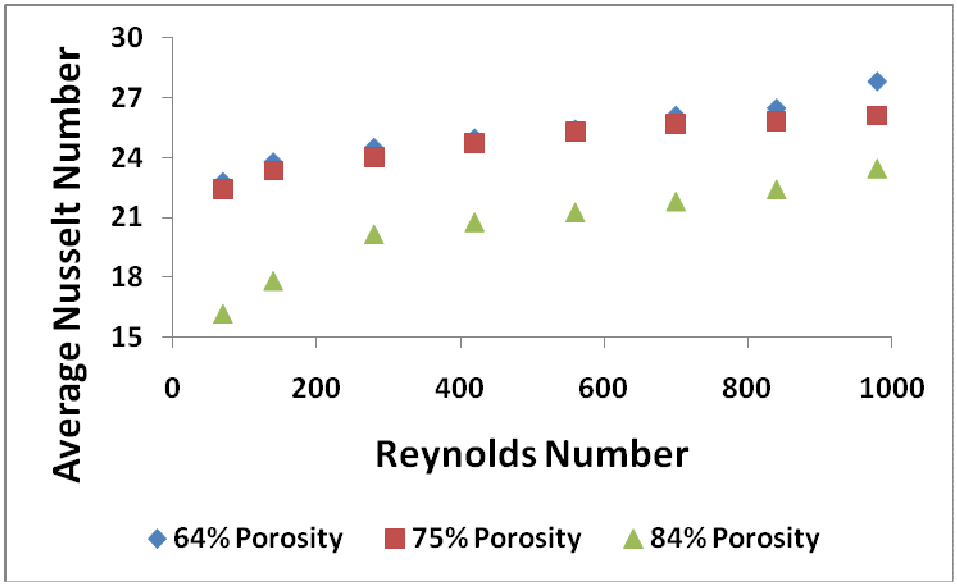

Figure B.29. Frequency = 64 Hz – Nusselt Number vs. Reynolds Number.

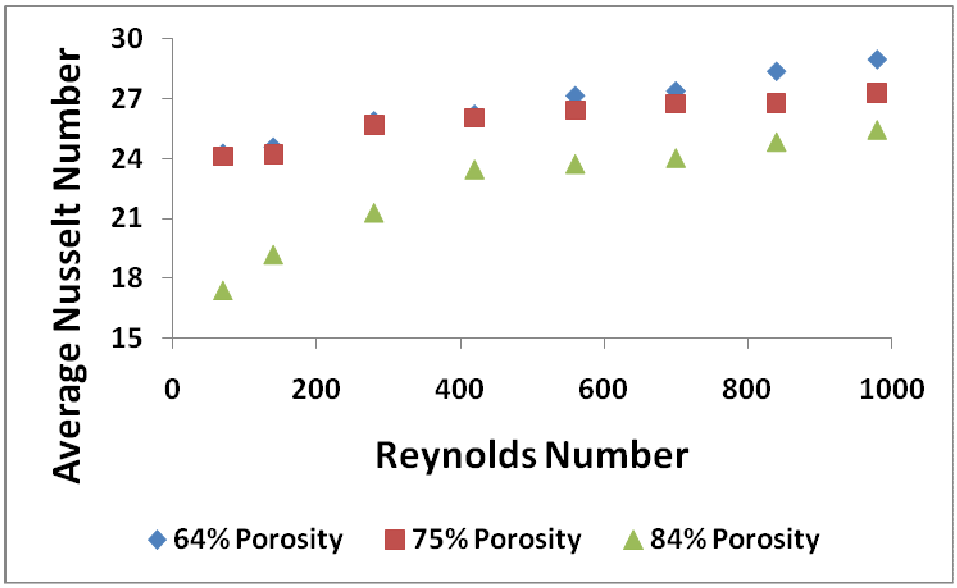

Figure B.30. Frequency = 80 Hz – Nusselt Number vs. Reynolds Number.

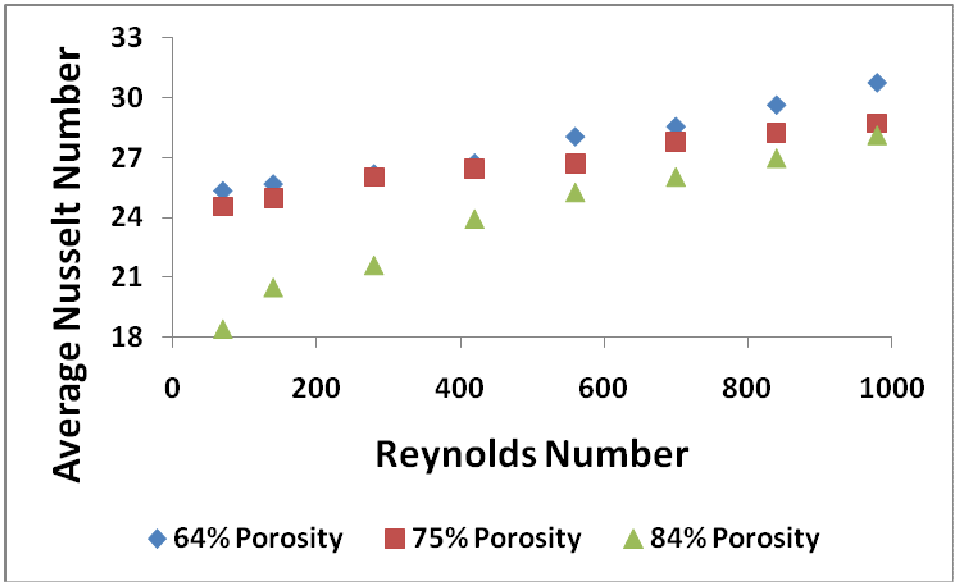

Figure B.31. Frequency = 100 Hz – Nusselt Number vs. Reynolds Number.

APPENDIX C

DIMENSIONLESS THERMAL DISPERSION PLOTS

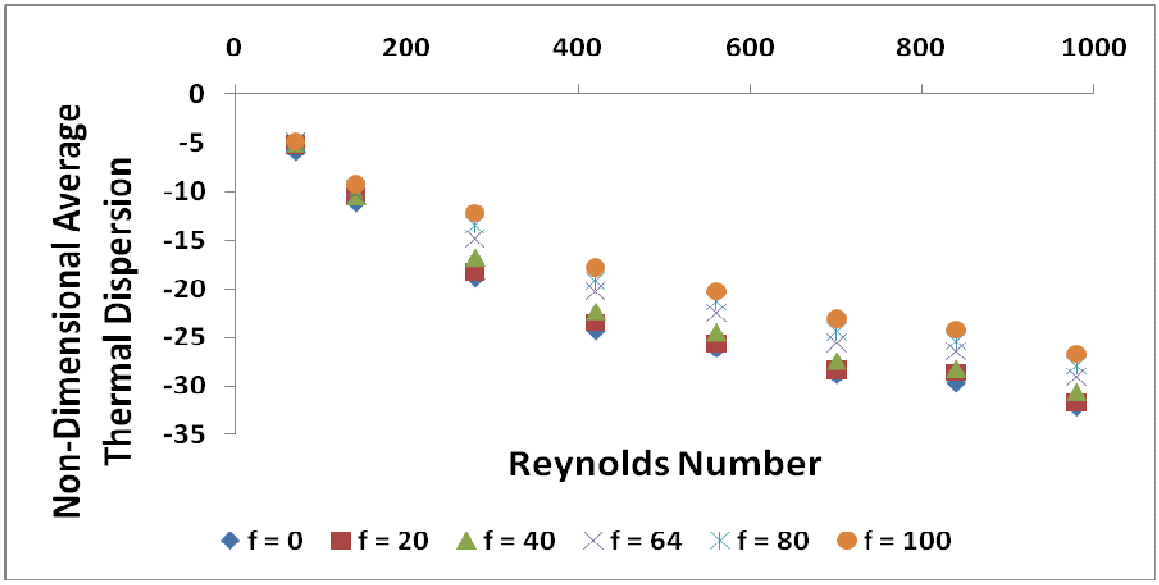

Figure C.1. 64% Porosity – Non-Dimensional Dispersion vs. Reynolds Number.

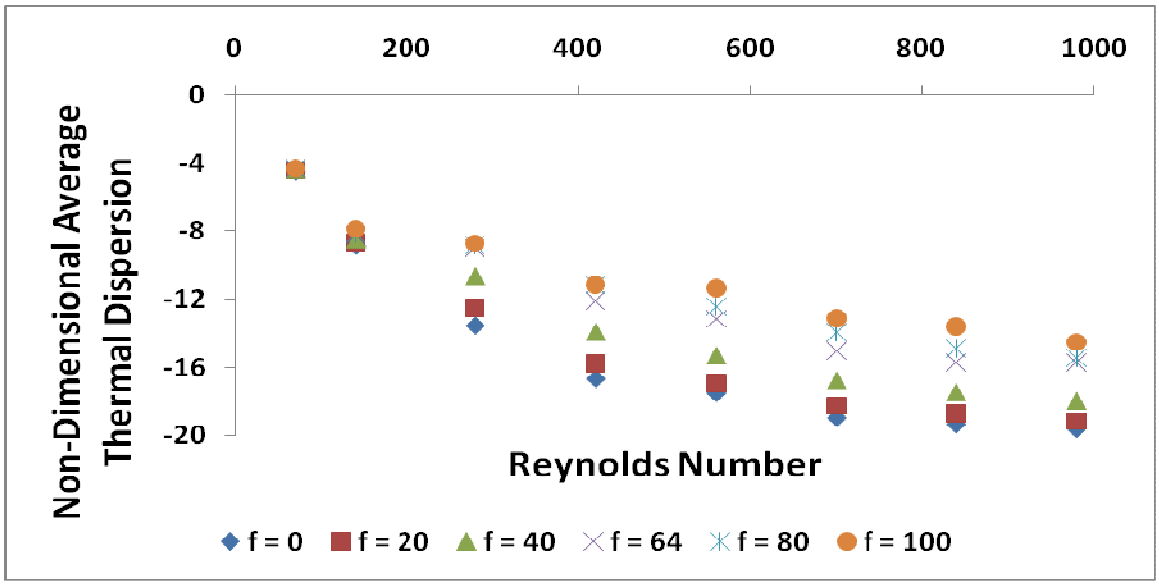

Figure C.2. 75% Porosity – Non-Dimensional Dispersion vs. Reynolds Number.

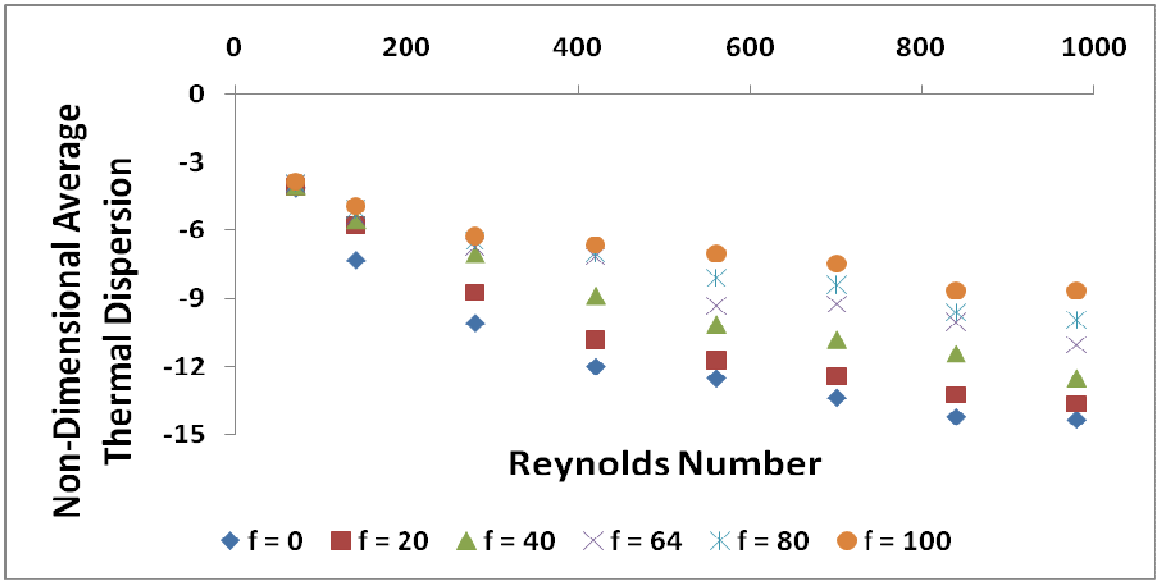

Figure C.3. 84% Porosity – Non-Dimensional Dispersion vs. Reynolds Number.

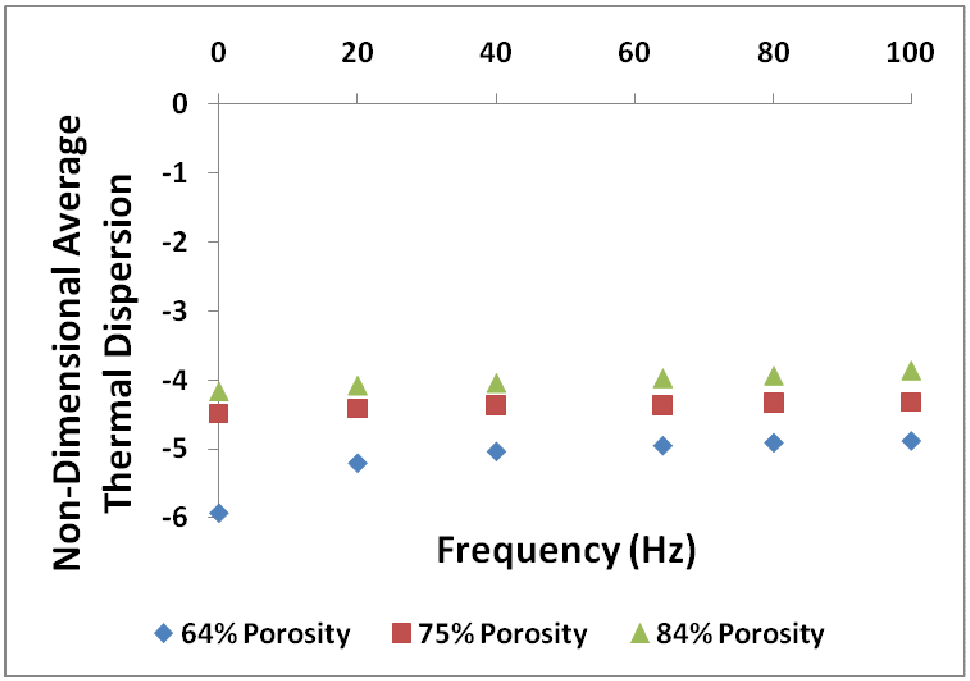

Figure C.4. Reynolds Number = 70 – Non-Dimensional Dispersion vs. Frequncey..

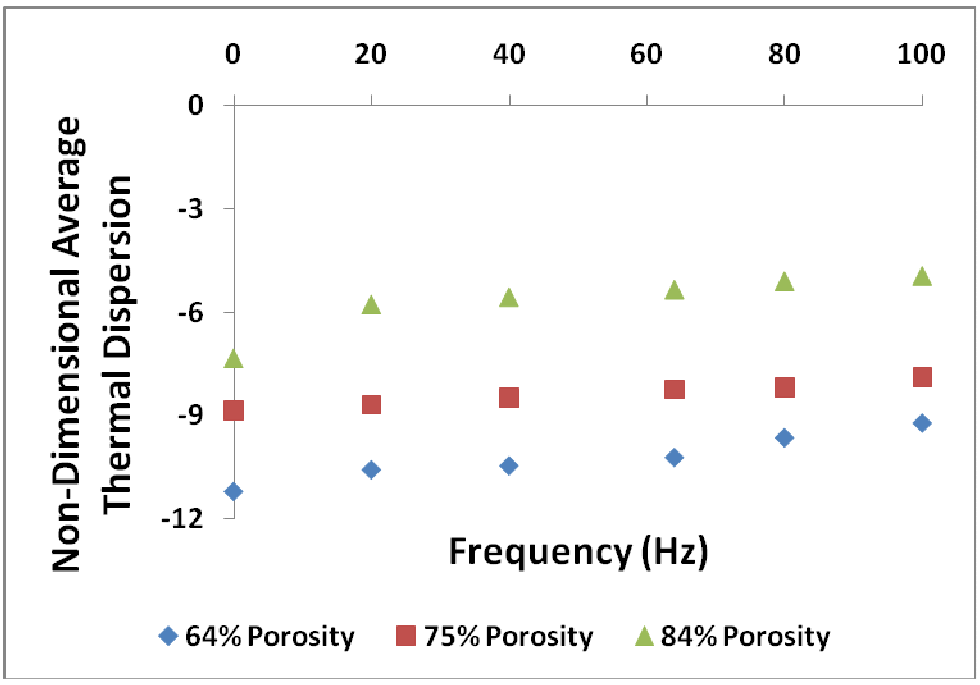

Figure C.5. Reynolds Number = 140 – Non-Dimensional Dispersion vs. Frequency.

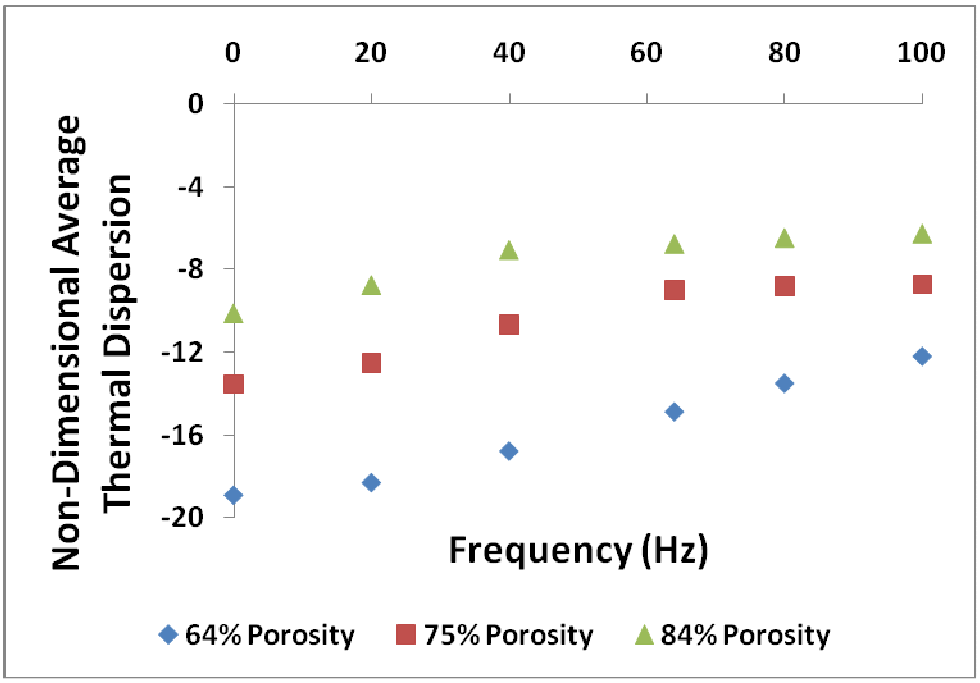

Figure C.6. Reynolds Number = 280 – Non-Dimensional Dispersion vs. Frequency.

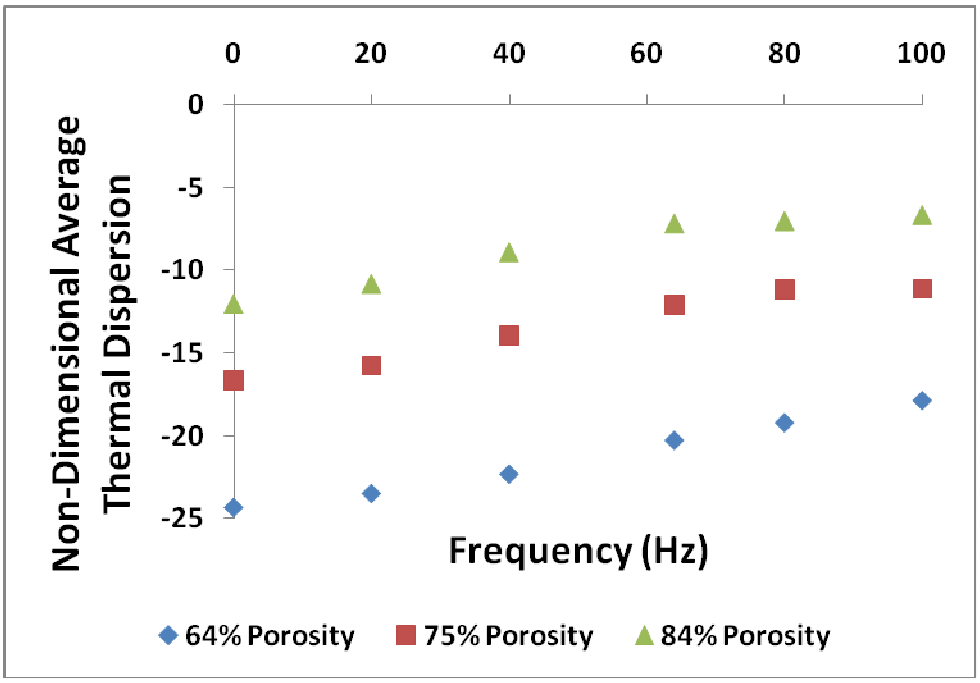

Figure C.7. Reynolds Number = 420 – Non-Dimensional Dispersion vs. Frequency.

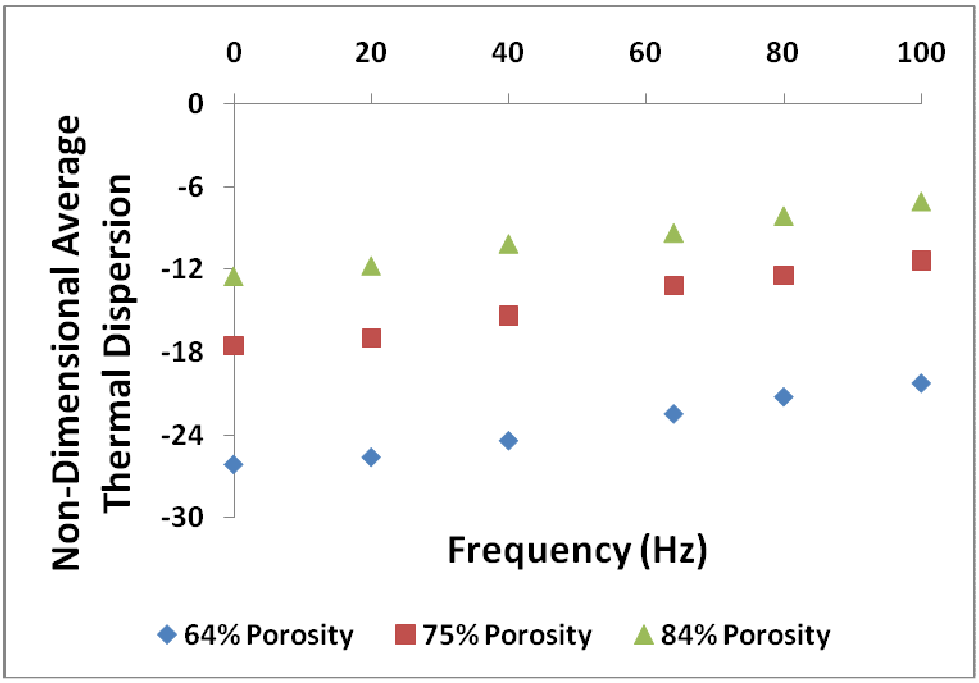

Figure C.8. Reynolds Number = 560 – Non-Dimensional Dispersion vs. Frequency.

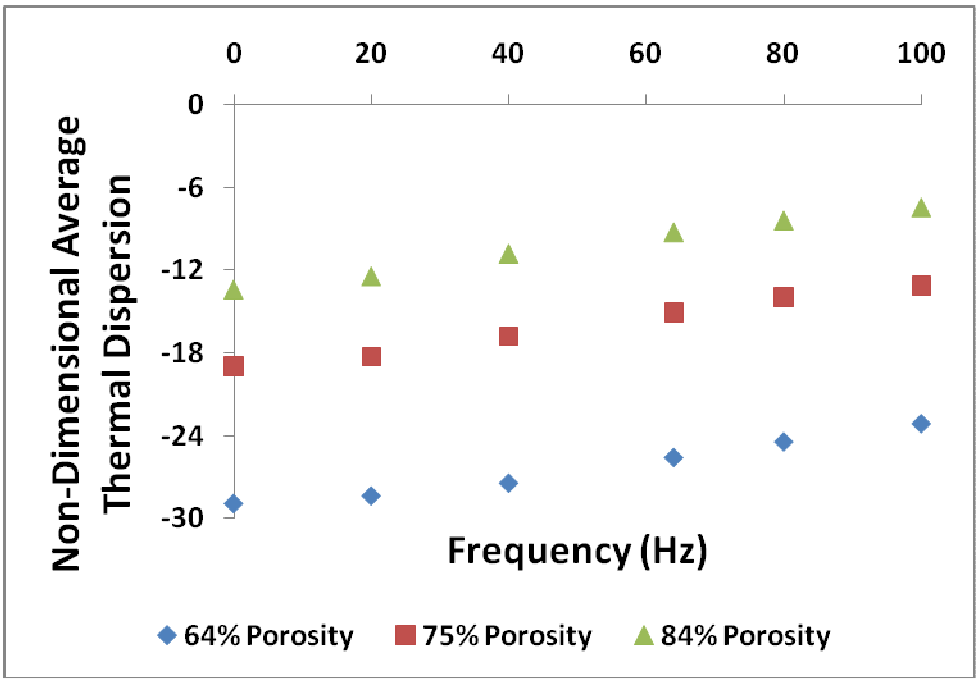

Figure C.9. Reynolds Number = 700 – Non-Dimensional Dispersion vs. Frequency.

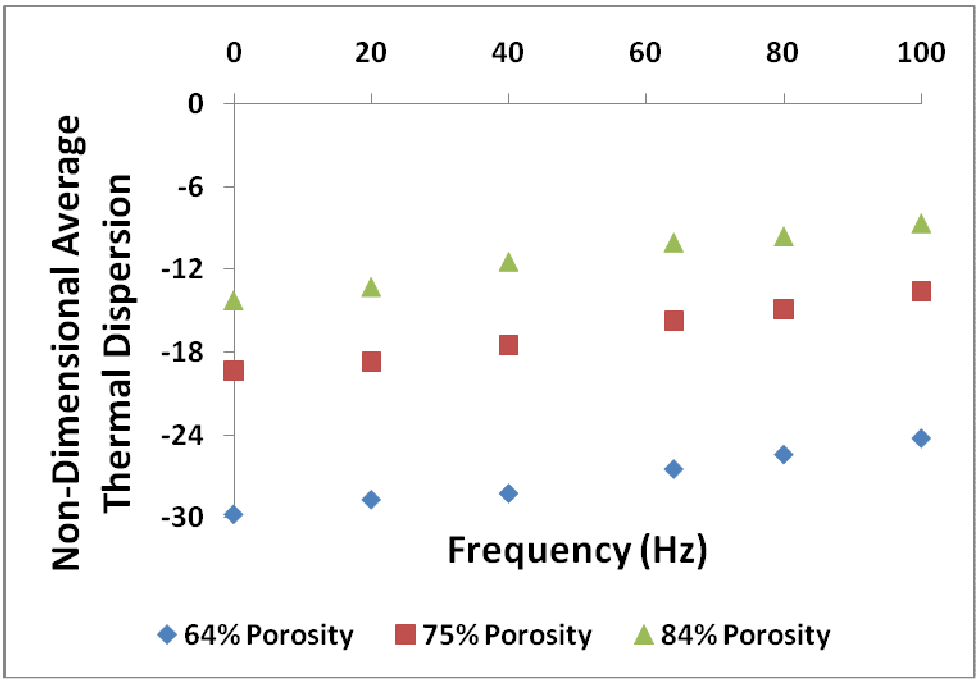

Figure C.10. Reynolds Number = 840 – Non-Dimensional Dispersion vs. Frequency.

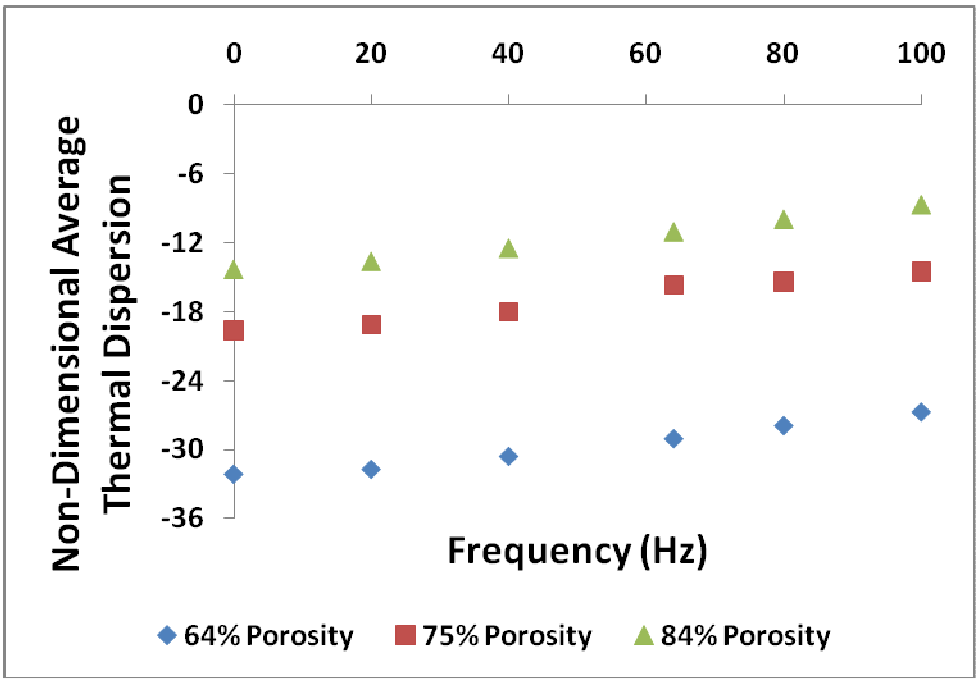

Figure C.11. Reynolds Number = 980 – Non-Dimensional Dispersion vs. Frequency.

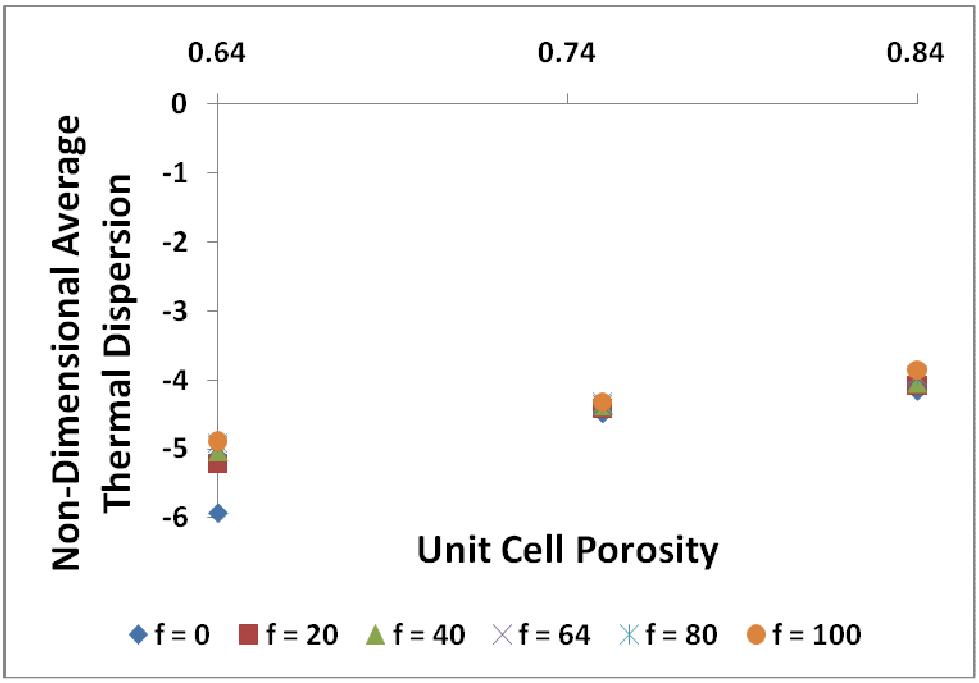

Figure C.12. Reynolds Number = 70 – Non-Dimensional Dispersion vs. Porosity.

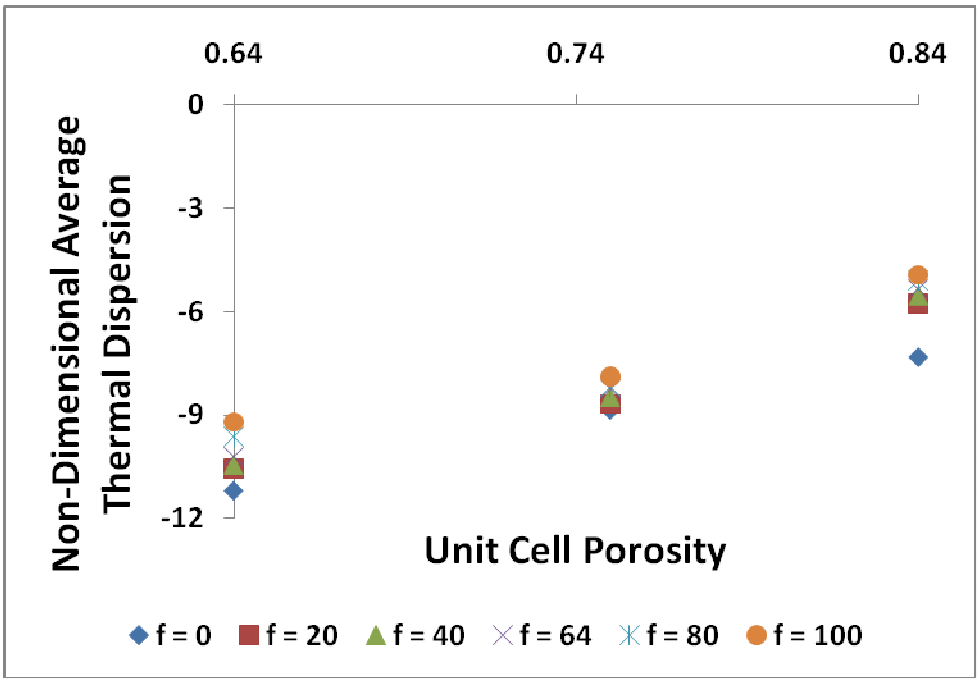

Figure C.13. Reynolds Number = 140 – Non-Dimensional Dispersion vs. Porosity.

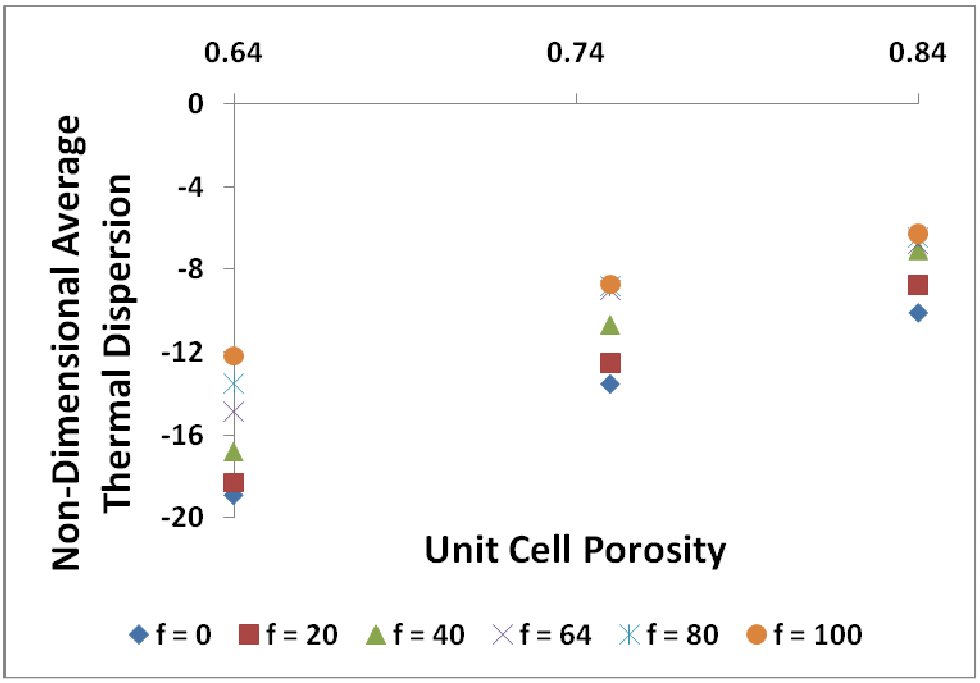

Figure C.14. Reynolds Number = 280 – Non-Dimensional Dispersion vs. Porosity.

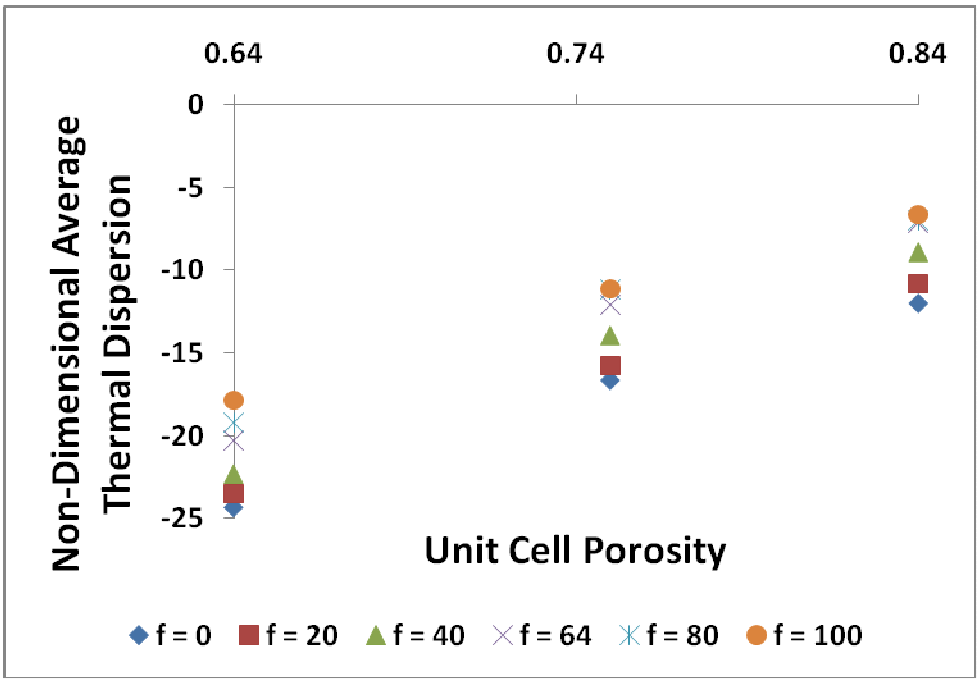

Figure C.15. Reynolds Number = 420 – Non-Dimensional Dispersion vs. Porosity.

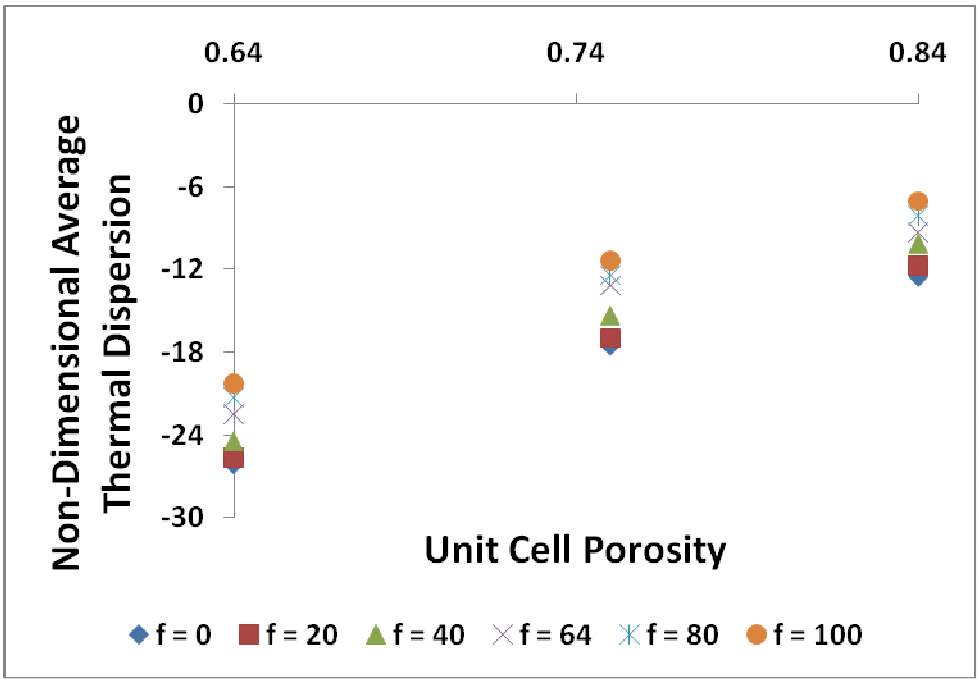

Figure C.16. Reynolds Number = 560 – Non-Dimensional Dispersion vs. Porosity.

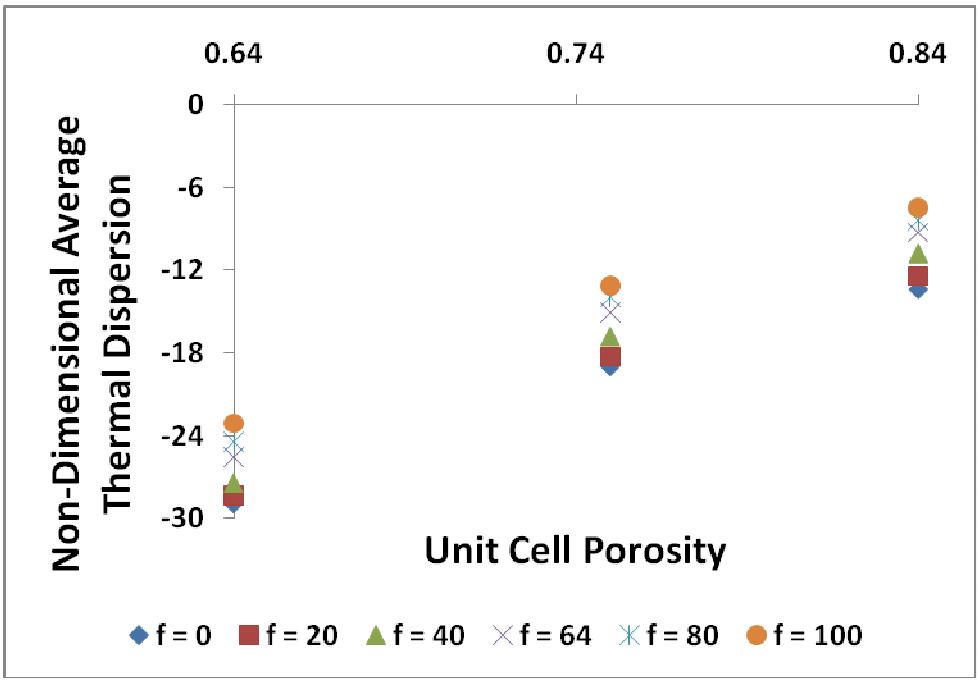

Figure C.17. Reynolds Number = 700 – Non-Dimensional Dispersion vs. Porosity.

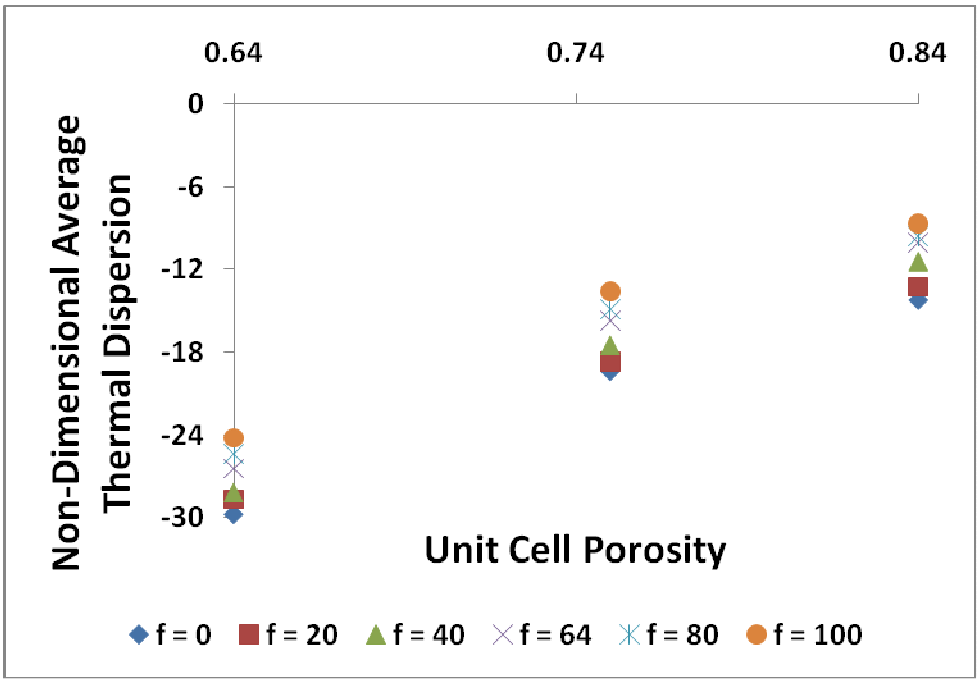

Figure C.18. Reynolds Number = 840 – Non-Dimensional Dispersion vs. Porosity.

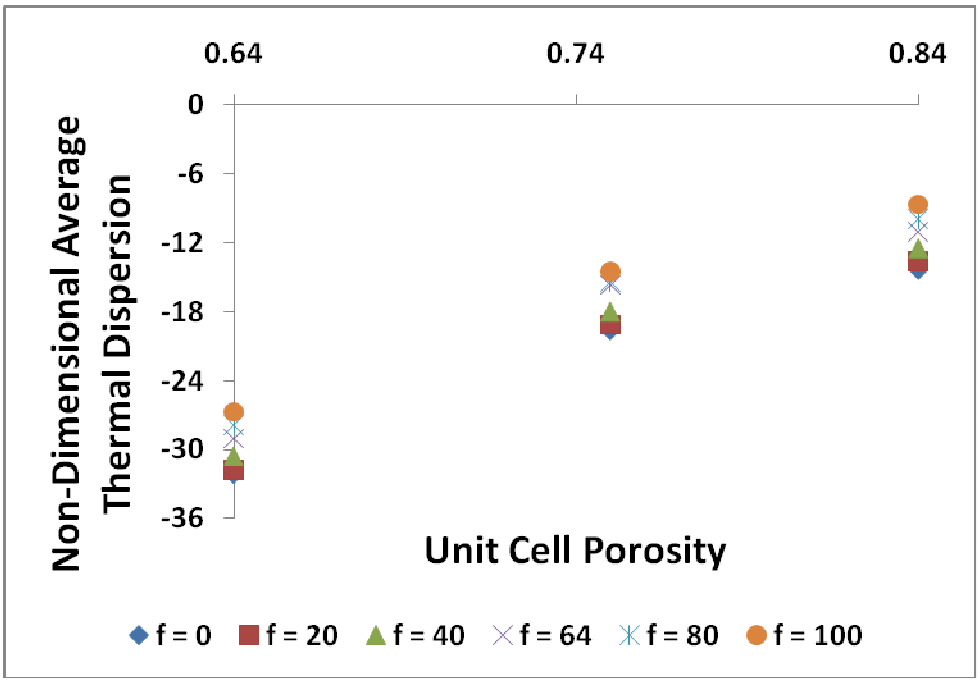

Figure C.19. Reynolds Number = 980 – Non-Dimensional Dispersion vs. Porosity.

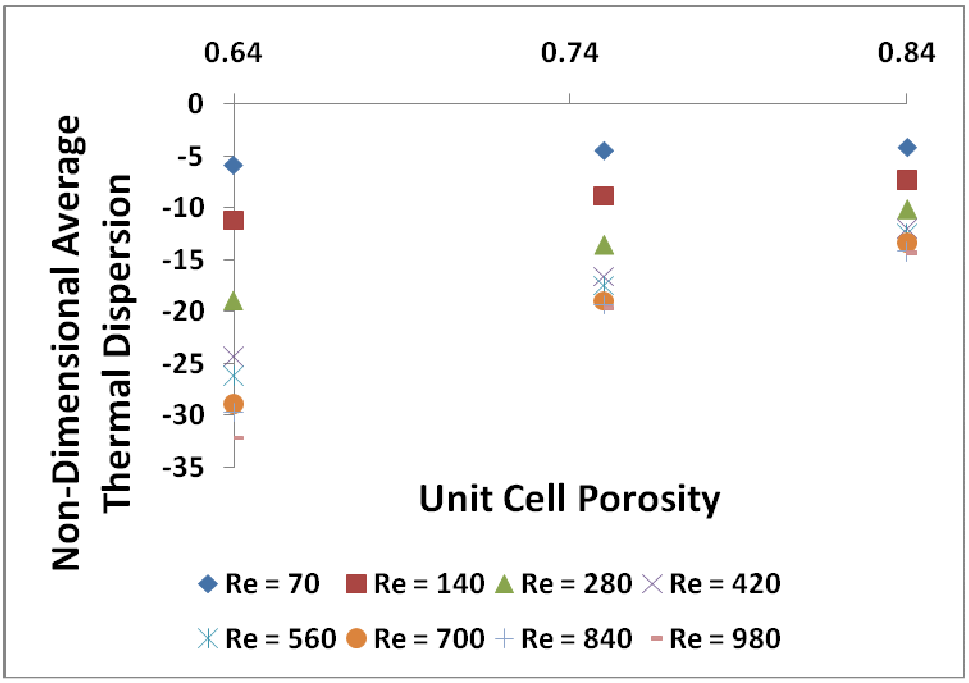

Figure C.20. Frequency = 0 Hz – Non-Dimensional Dispersion vs. Unit Cell Porosity.

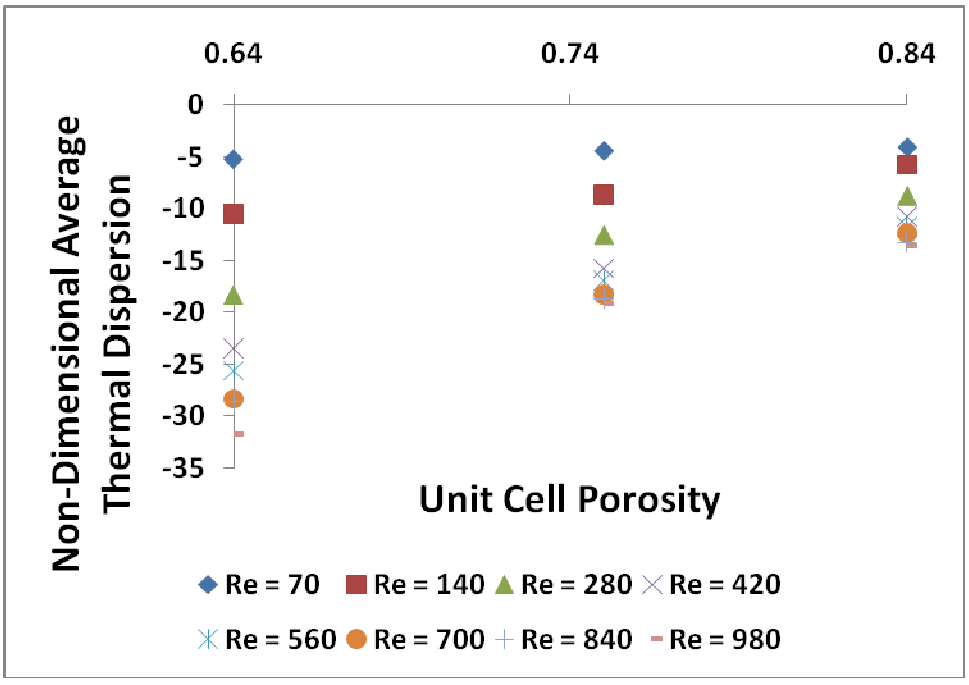

Figure C.21. Frequency = 20 Hz – Non-Dimensional Dispersion vs. Unit Cell Porosity.

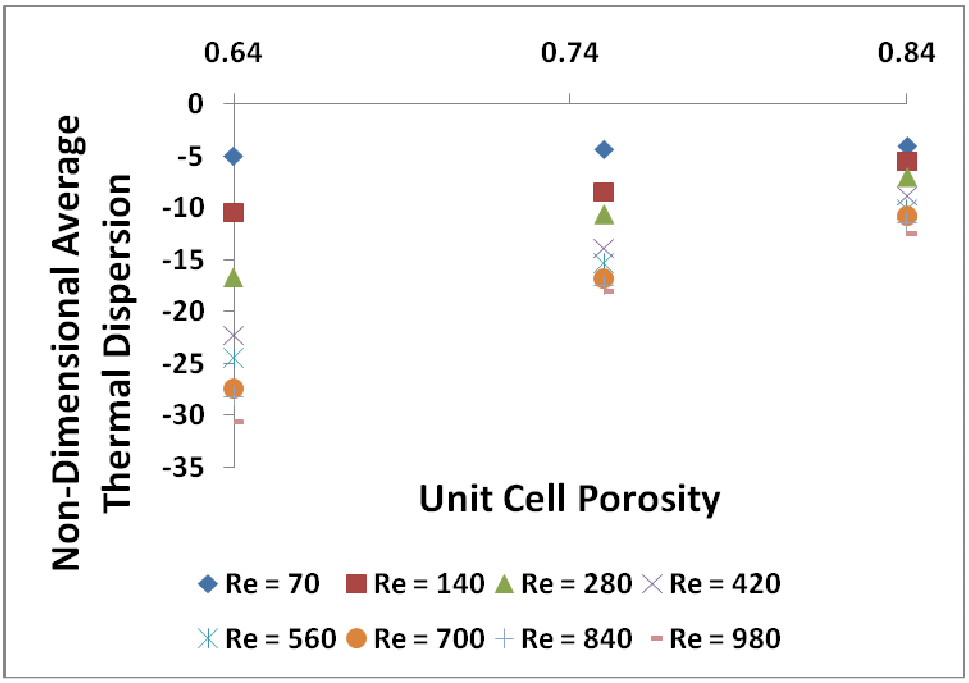

Figure C.22. Frequency = 40 Hz – Non-Dimensional Dispersion vs. Unit Cell Porosity.

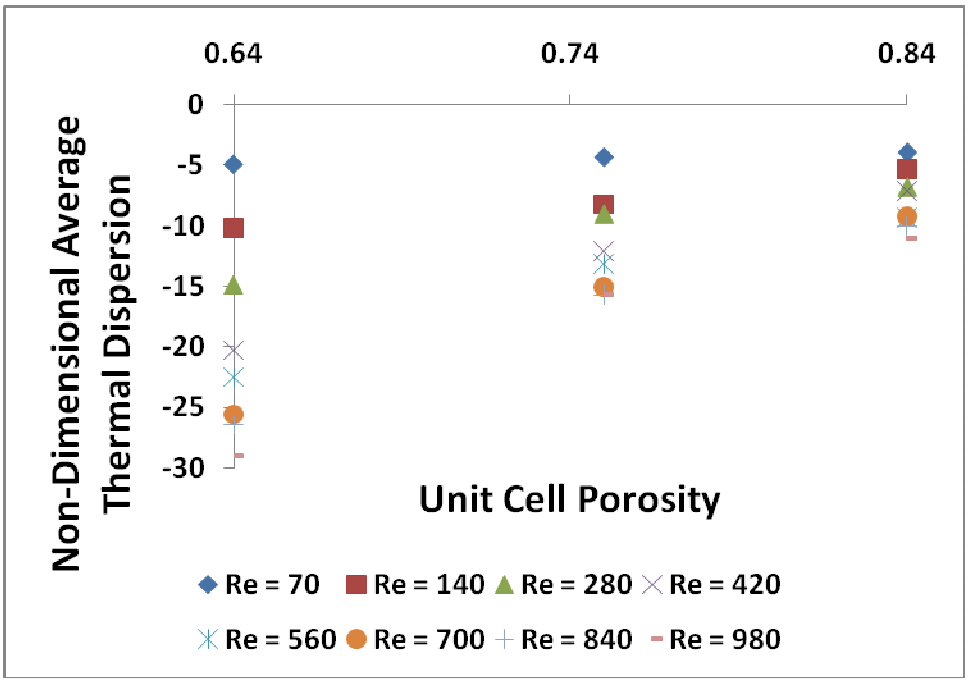

Figure C.23. Frequency = 64 Hz – Non-Dimensional Dispersion vs. Unit Cell Porosity.

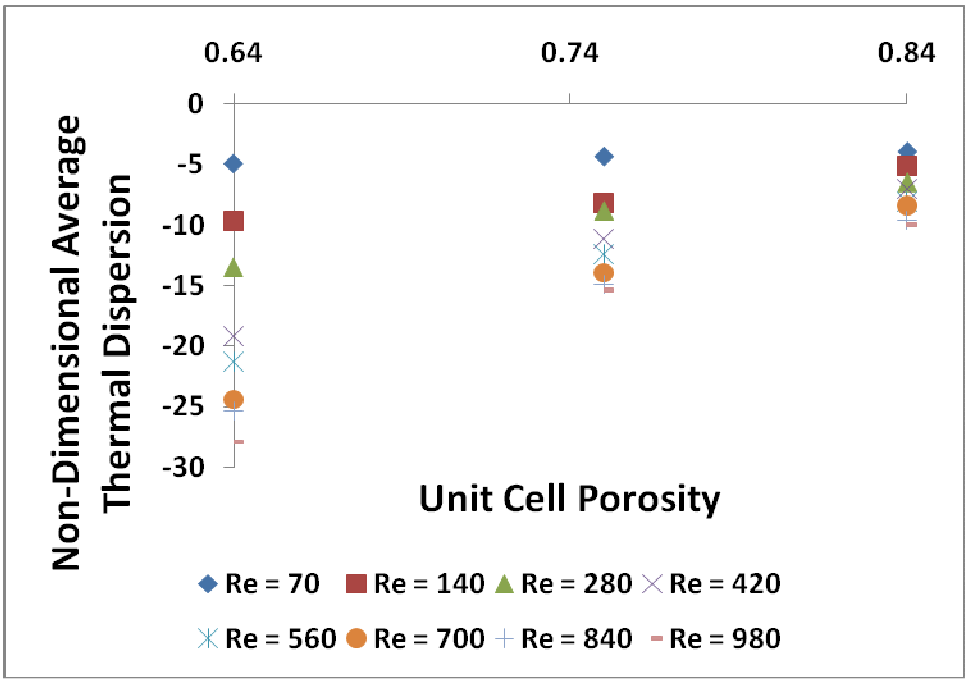

Figure C.24. Frequency = 80 Hz – Non-Dimensional Dispersion vs. Unit Cell Porosity.

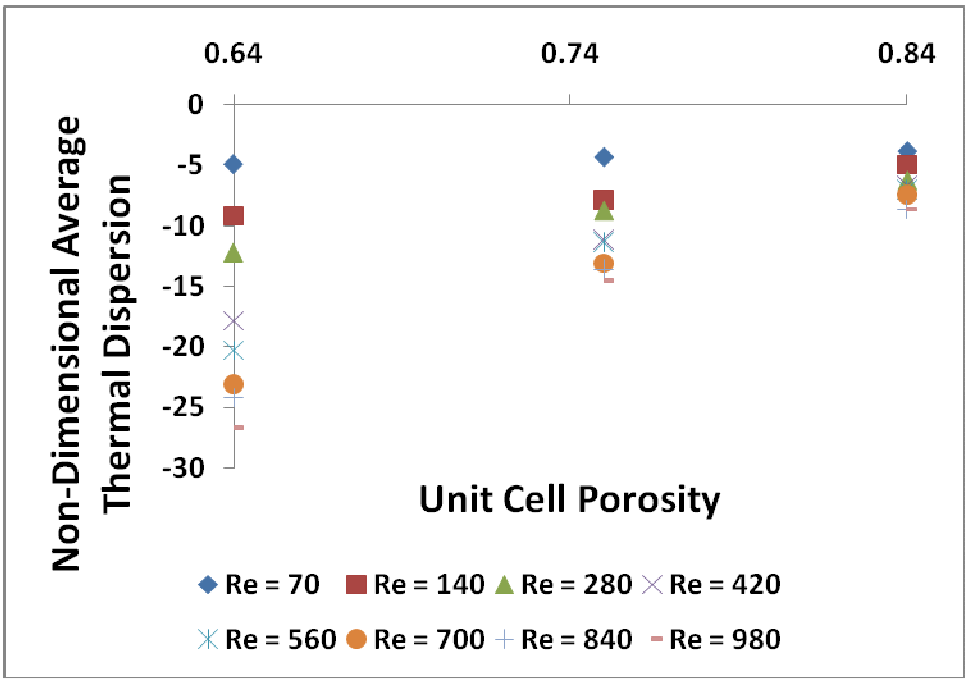

Figure C.25. Frequency = 100 Hz – Non-Dim. Dispersion vs. Unit Cell Porosity.

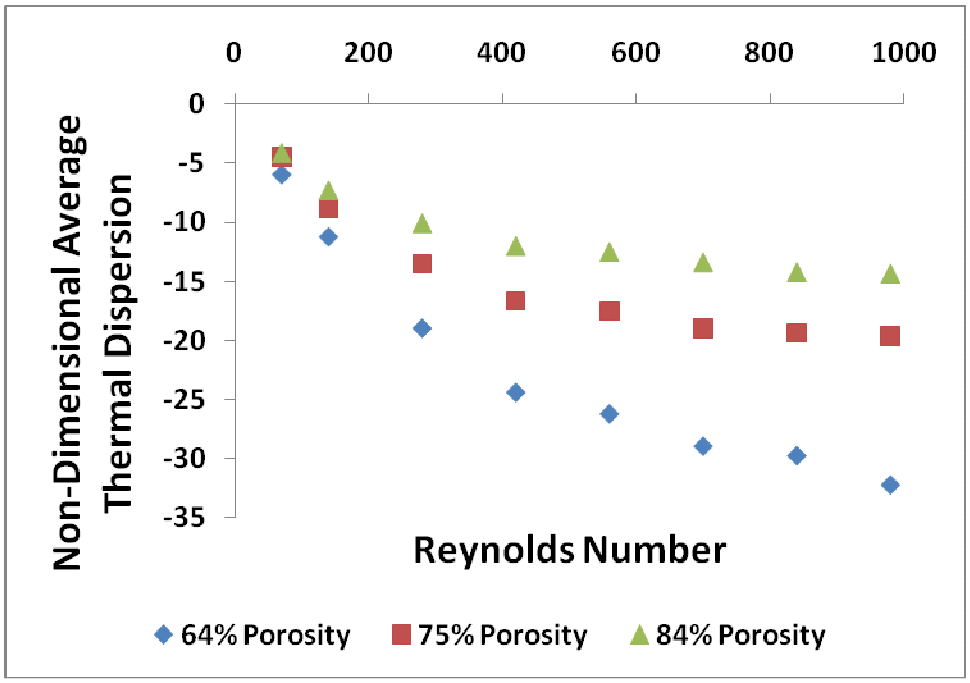

Figure C.26. Frequency = 0 Hz – Non-Dimensional Dispersion vs. Reynolds Number.

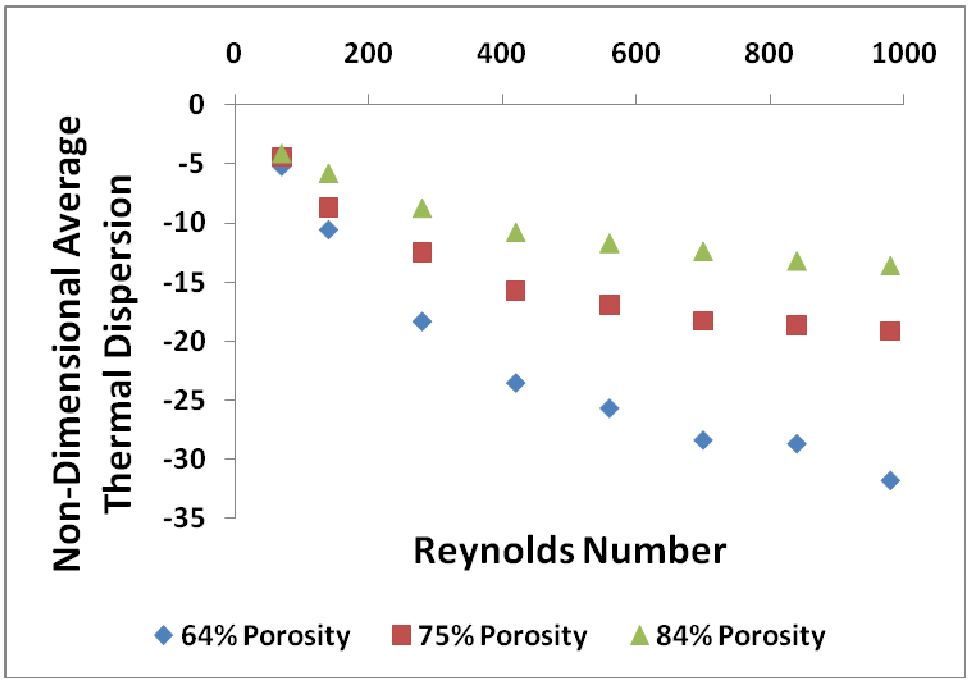

Figure C.27. Frequency = 20 Hz – Non-Dimensional Dispersion vs. Reynolds Number.

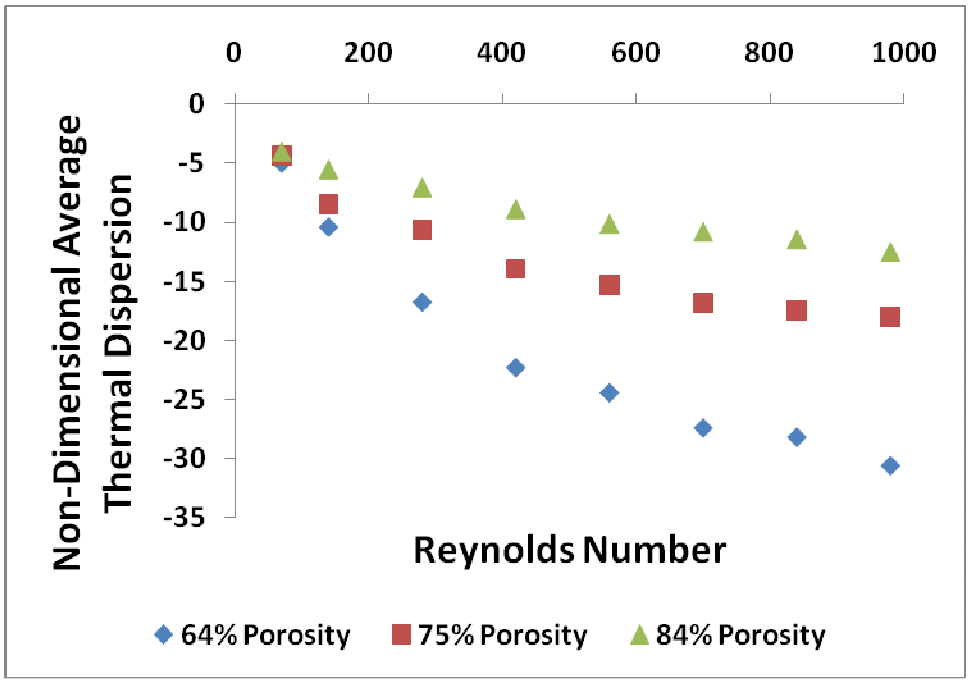

Figure C.28. Frequency = 40 Hz – Non-Dimensional Dispersion vs. Reynolds Number.

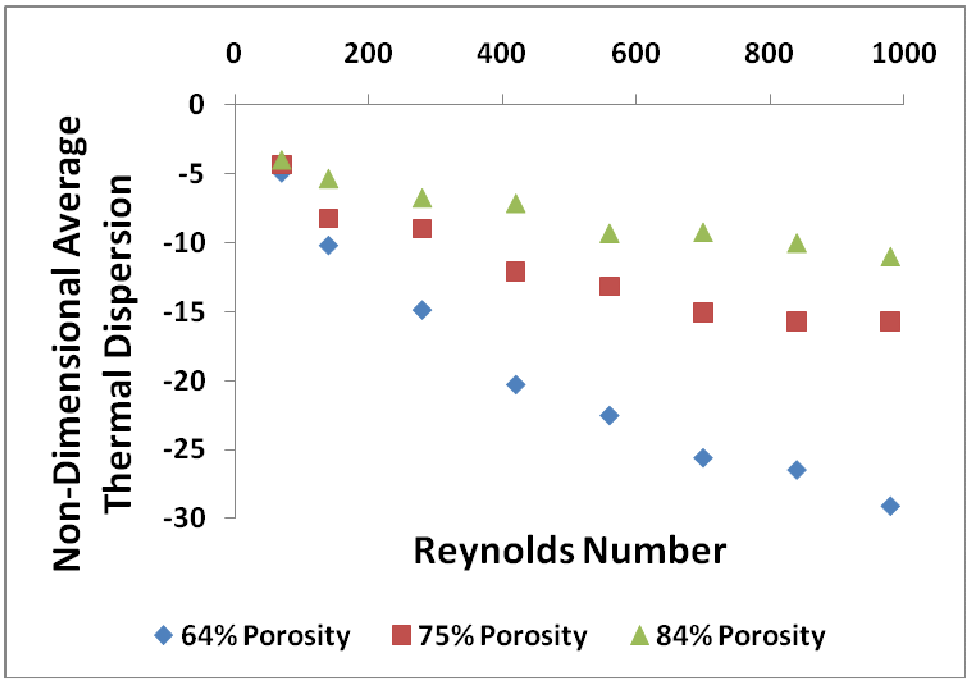

Figure C.29. Frequency = 64 Hz – Non-Dimensional Dispersion vs. Reynolds Number.

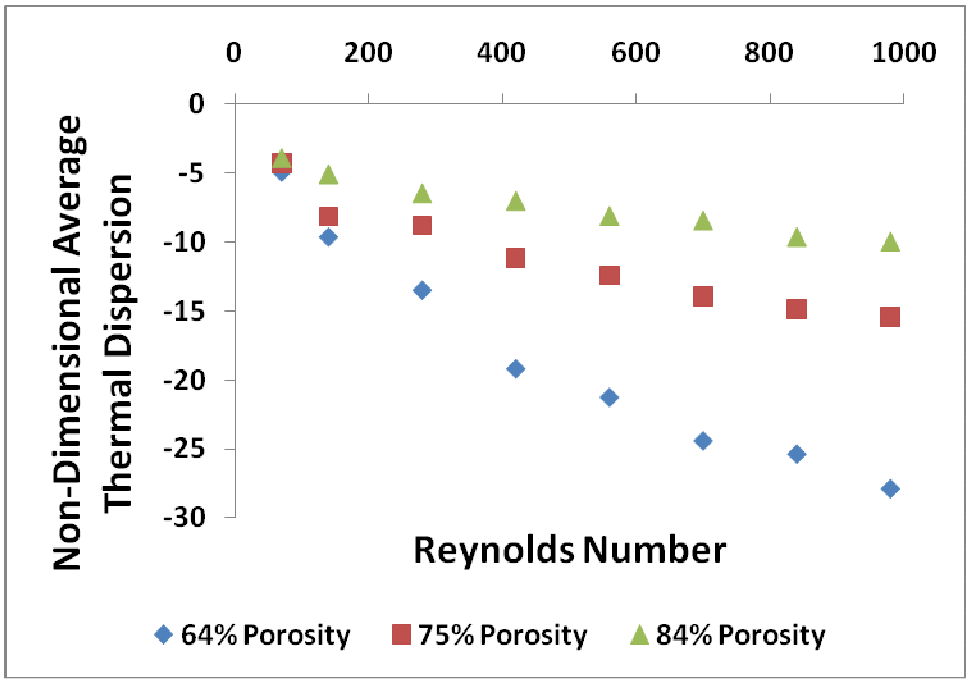

Figure C.30. Frequency = 80 Hz – Non-Dimensional Dispersion vs. Reynolds Number.

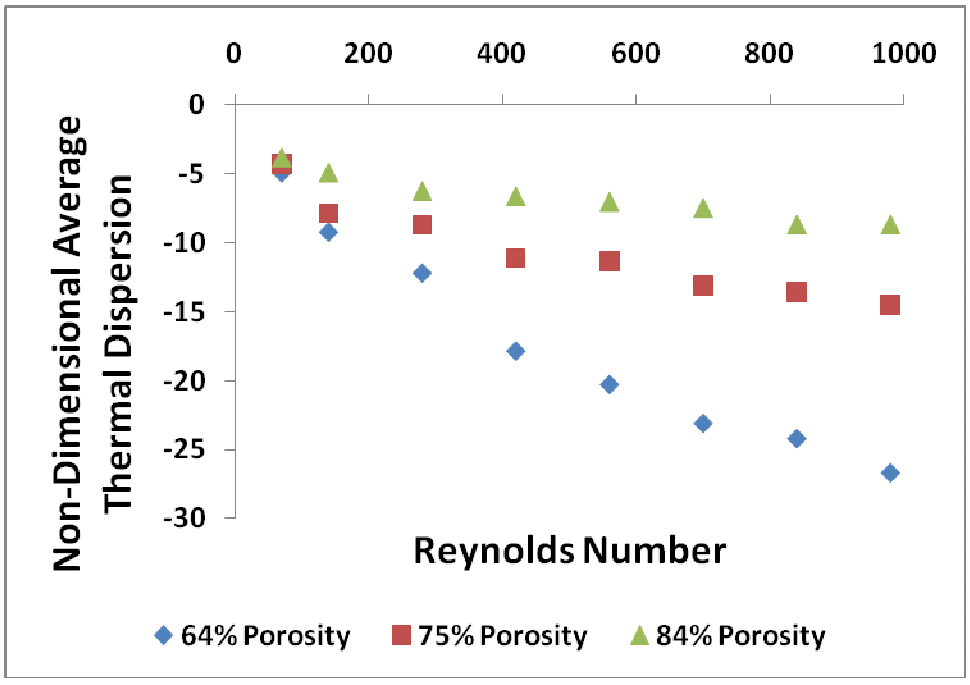

Figure C.31. Frequency = 100 Hz – Non-Dim. Dispersion vs. Reynolds Number.

REFERENCES

[1] R. Radebaugh, "Development of the Pulse Tube Refrigerator as an Efficient and Reliable Cryocooler," *Proc. Institute of Refrigeration (London),* 1999 1999.

[2] R. A. Ackermann, *Cryogenic regenerative heat exchangers*. New York: Plenum Press, 1997.

[3] W. E. Gifford and R. C. Longsworth, "Pulse Tube Refrigeration," *ASME,* vol. 63, 1963.

[4] F. P. Incropera. (2007, *Fundamentals of heat and mass transfer / : Frank P. Incropera ... [et al.] (6th ed.)*.

[5] E. C. Landrum, "Anisotropic parameters of mesh fillers relevant to miniature cryocoolers," Master's Thesis, Mechanical Engineering, Georgia Institute of Technology, Atlanta, 2009.

[6] J. S. Cha, "Simulation of Multi-Dimensional Effects in Inertance Tube Pulse Tube Cryocoolers," Master's Thesis, Mechanical Engineering, Georgia Institute of Technology, Atlanta 2004.

[7] J. P. Harvey, "Parametric study of cryocooler regenerator performance," Master's Thesis, Mechanical Engineering, Georgia Institute of Technology, Atlanta, 1999.

[8] M. Kaviany, *Principals of heat transfer in porous media*, 2nd ed., Springer-Veriag, 2006.

[9] M. Pedras and M. de Lemos, "Simulation of turbulent flow in porous media using a spatially periodic array and a low Re two-equation closure," *Numerical Heat Transfer, Part A: Applications,* vol. 39, pp. 35-59, 2001.

[10] K. Vafai and C. Tien, "Boundary and inertia effects on flow and heat transfer in porous media," *International Journal of Heat and Mass Transfer,* vol. 24, pp. 195-203, 1981.

[11] A. Nakayama, F. Kuwahara, and Y. Kodama "An equation for thermal dispersion flux transport and its mathematical modelling for heat and fluid flow in a porous medium," *Journal of Fluid Mechanics,* vol. 563, pp. 81-96, 2006.

[12] S.M. Kim and S. M. Ghiaasiaan, "Numerical Modeling of Laminar Pulsating Flow in Porous Media," *Journal of Fluids Engineering,* vol. 131, p. 041203, 2009.

[13] A. Nakayama, F. Kuwahara, and M. Sugiyama, G. Xu, "A two-energy equation model for conduction and convection in porous media," *International Journal of Heat and Mass Transfer,* vol. 44, pp. 4375-4379, 2001.

[14] P. Jiang and Z. Ren, "Numerical investigation of forced convection heat transfer in porous media using a thermal non-equilibrium model," *International Journal of Heat and Fluid Flow,* vol. 22, pp. 102-110, 2001.

[15] Z. Guo, S. Kim, and H. Sung, "Pulsating flow and heat transfer in a pipe partially filled with a porous medium," *International Journal of Heat and Mass Transfer,* vol. 40, pp. 4209-4218, 1997.

[16] A. Nakayama, F. Kuwahara, and T. Hayashi, "Numerical modelling for three-dimensional heat and fluid flow through a bank of cylinders in yaw," *Journal of Fluid Mechanics,* vol. 498, pp. 139-159, 2004.

[17] N. Benarji, C. Balaji, and S. Venkateshan, "Unsteady fluid flow and heat transfer over a bank of flat tubes," *Heat and mass transfer,* vol. 44, pp. 445-461, 2008.

[18] I. Garaway, Z. Gan, P. Bradely, A. Veprik, and R. Radebaugh, "Development of a Miniature 150 Hz Pulse Tube Cryocooler."

[19] J.S. Cha, S.M. Ghiaasiaan, P.V. Desai, J.P. Harvey, and C.S. Kirkconnell, "CFD simulation of multi-dimensional effects in an Inertance tube pulse tube refrigerator," *Cryocoolers 13,* pp. 285-292.

[20] J.S. Cha, S.M. Ghiaasiaan, and C.S. Kirkconnell, "Oscillatory flow in microporous media applied in pulse-tube and Stirling-cycle cryocooler regenerators," *Experimental Thermal and Fluid Science,* vol. 32, pp. 1264-1278, 2008.

[21] W.M. Clearman, J.S. Cha, S.M. Ghiaasiaan, and C.S. Kirkconnell, "Anisotropic steady-flow hydrodynamic parameters of microporous media applied to pulse tube and Stirling cryocooler regenerators," *Cryogenics,* vol. 48, pp. 112-121, 2008.

[22] K. Nam and S. Jeong, "Novel flow analysis of regenerator under oscillating flow with pulsating pressure," *Cryogenics,* vol. 45, pp. 368-379, 2005.

[23] W. Clearman, "Measurement and Correlation of Directional Permeability and Forchheimer's Inertial Coefficient of Micro Porous Structures Used in Pulse Tube Cryocoolers," 2007.

[24] J.S. Cha, S.M. Ghiaasiaan, and C.S. Kirkconnell, "Measurement of Anisotropic Hydrodynamic Parameters of Pulse Tube or Stirling Cryocooler Regenerators," 2006, p. 1911.

[25] R. Sahoo and S. Das, "Exergy maximization in cryogenic regenerators," *Cryogenics,* vol. 34, pp. 475-482, 1994.

[26] F.Z. Guo, Y.M. Chou, S.Z. Lee, Z.S. Wang, and W. Mao, "Flow characteristics of a cyclic flow regenerator," *Cryogenics,* vol. 27, pp. 152-155, 1987.

[27] H. Erk and M. Dudukovic, "Phase-Change Heat Regenerators-Modeling and Experimental Studies (Vol 42, Pg 791, 1996)," *AIChE Journal,* vol. 43, pp. 1189-1189, 1997.

[28] K.V. Dobrego, N.N. Gnesdilov, I.M. Kozlov, V.I. Bubnovich, and H.A. Gonzalez, "Numerical investigation of the new regenerator-recuperator scheme of VOC oxidizer," *International Journal of Heat and Mass Transfer,* vol. 48, pp. 4695-4703, 2005.

[29] M. Ogawa, R. Li, and T. Hashimoto, "Thermal conductivities of magnetic intermetallic compounds for cryogenic regenerator," *Cryogenics,* vol. 30, pp. 521-526, 1990.

[30] A. Willmott, "Digital computer simulation of a thermal regenerator," *International Journal of Heat and Mass Transfer,* vol. 7, pp. 1291-1302, 1964.

[31] X. Hua and G. Zhong, "Analytical network model on the flow and thermal characteristics of cyclic flow cryogenic regenerators," *Cryogenics,* vol. 28, pp. 762-769, 1988.

[32] R. Radebaugh, A. O'Gallagher, and J. Gary, "Regenerator behavior at 4 K: Effect of volume and porosity," 2002, p. 961.

[33] A. De Waele and J. Zeegers, "Counterflow pulse-tube refrigerators," 2002, p. 617.

[34] H. Yuan and L. Jing-Tao, "The effect of the regenerator and tube volume on the performance of a high frequency miniature pulse tube refrigerator," *Journal of Engineering Thermophysics,* 2002.

[35] G. Popescu, V. Radcenco, E. Gargalian, P.R. Bala, "A critical review of pulse tube cryogenerator research," *International Journal of Refrigeration,* vol. 24, pp. 230-237, 2001.

[36] S. Kim, "Numerical investigation on laminar pulsating flow through porous media," 2008.

[37] "Gambit 2 User Manual," ed: Fluent Inc. , 2006.

[38] S. Whitaker, "The Method of volume averaging," Kluwer Academic, 1999.

[39] "Fluent 6 User Manual," ed: Fluent Inc., 2006.

[40] "Matlab," ed: Mathworks Inc. , 2008.